

NORTHWESTERN UNIVERSITY

Mapping Magnetic Fields in the Cold Dust at the Galactic Center

A DISSERTATION

SUBMITTED TO THE GRADUATE SCHOOL
IN PARTIAL FULFILLMENT OF THE REQUIREMENTS

for the degree

DOCTOR OF PHILOSOPHY

Field of Physics and Astronomy

By

David Thomas Chuss

EVANSTON, ILLINOIS

December 2002

© Copyright by David Thomas Chuss 2002

All Rights Reserved

Abstract

Mapping Magnetic Fields in the Cold Dust at the Galactic Center

David Thomas Chuss

We present polarimetry results of the Galactic center with two complementary instruments: SPARO (Submillimeter Polarimeter for Antarctic Remote Observing), a $450\ \mu\text{m}$ polarimeter with $6'$ resolution, and Hertz, a $350\ \mu\text{m}$ polarimeter with $20''$ resolution operating on the Caltech Submillimeter Observatory. The design of SPARO is reviewed. A description of the data acquisition and analysis for SPARO is included. Finally, results are presented for the two instruments that are consistent with a model for the Galactic center magnetosphere in which an initially poloidal field has been sheared into a toroidal configuration in regions in which the energy density of gravity dominates that of magnetic fields. The SPARO data show that at low latitudes over much of the central 200 pc of the Galactic center, the field is toroidal. The Hertz data focus on the central 30 pc and find a

clumpy matter distribution in which the dense regions are dominated by a toroidal field, while in the less dense regions, the field is preferentially poloidal. We use this model to estimate a characteristic field strength in this region of ~ 3 mG.

Acknowledgements

There are many people for whose support I am extremely grateful. To begin with, I would like to thank the undergraduates who have passed through our lab and have helped to make our efforts over the past few years fruitful. These people include Chris Greer, Jill Hanna, Prashant Malhotra, Jen Marshall, Tim O'Brien, Sharon Loverde, and Sarah Williams.

For their work on the design and construction of SPARO, I would like to thank Bob Pernic, Jesse Wirth, Bob Hirsch, Bob Spotz, Jeff Sundwall, Jim Jaegar, and Dave Pernic. I would also like to thank Bob Loewenstein for his valuable contributions to SPARO's data acquisition system.

Because it is so difficult to keep a telescope at the South Pole operating, I would like to acknowledge the Viper team: John Ruhl, Bill Holtzapfel, Jeff Peterson, Matt Newcomb, Mark Thoma, Chao-Lin Kuo, Mike Daub, Jon Goldstein, Marcus Runyan, and John Davis. These people have always been great company on my numerous excursions to the South Pole. I would especially like to thank Dave

Pernic once again for keeping SPARO running during Austral Winter 2000 and Greg Griffin for being so dedicated to SPARO science during that winter.

I would like to thank Roger Hildebrand for his guidance over the last few years. I would also like to thank Darren Dowell, John Vaillancourt, Tom Renbarger, and Jackie Davidson for their support as collaborators.

I would like to thank Harvey Moseley, my adviser for the NASA Graduate Student Researchers' Program (NGT 5-88) from which I received a good deal of my funding as a graduate student.

I would like to thank Farhad Yusef-Zadeh for his helpful discussions concerning magnetic fields in the Galactic center and for providing me access to some of his data for comparison with my own. Also, I would like to thank Namir Kassim and Douglas Pierce-Price for providing their data in electronic form.

I would also like to thank Dave Joffe for all of the discussions over lunch of the last few years.

When I first arrived at Northwestern, Jessie Dotson spent a great deal of her time and energy teaching me how to be an instrumentalist. Since then, she has continued to provide valuable career guidance. For this and for her friendship, I am grateful.

It is hard for me to comprehend the concept of being solely responsible for someone's professional training, especially in a field like Astrophysics. Luckily for

me, my adviser, Giles Novak, took this responsibility to heart. I would like to thank Giles for this and for teaching me to really appreciate science. I have really enjoyed the five years I have spent working for Giles, and I will always appreciate our friendship as well as our professional working relationship.

My parents, Tom and Nancy Chuss, have supported me in everything I have done and have taken pride in my accomplishments. For their love and support, I am extremely grateful.

Finally, without the support of my wife, Anne Marie, I would be lost. She is my best friend, and I love her with all of my heart. I truly appreciate all of the sacrifices she has made that allow me to be an Astrophysicist, and I look forward to sharing the future with her.

Contents

Abstract	iii
Acknowledgements	v
List of Tables	xi
List of Figures	xiii
Chapter 1. Introduction	1
Chapter 2. The Galactic Center: An Overview	6
2.1. The Environment	6
2.2. The Galactic Center Magnetosphere	9
Chapter 3. Magnetic Fields and Polarimetry	13
3.1. Grain Alignment and Astrophysical Magnetic Fields	13
3.2. Polarimetry	20
Chapter 4. SPARO Instrument Overview	31
4.1. Cryostat	31

4.2. Detectors	33
4.3. Optics	34
4.4. Observing Procedure	34
Chapter 5. SPARO Photometric Calibration	37
5.1. Pointing	37
5.2. NEFD	41
Chapter 6. SPARO Data Analysis	51
6.1. Determination of χ Angle and Polarization Efficiency	51
6.2. Instrumental Polarization	56
6.3. Snow on the Tertiary	69
6.4. Time Dependence	73
6.5. Edge Effect	74
6.6. Final Data	75
Chapter 7. Hertz	80
7.1. Instrument Overview	80
7.2. Observing Scheme	80
7.3. Analysis	81
7.4. Results	83

Chapter 8. Discussion	91
8.1. The Large Scale Field	93
8.2. Morphology of the Inner 30 Parsecs	96
8.3. Polarized Flux	109
8.4. Reference Beam Contamination	112
8.5. Poloidal Versus Toroidal Fields	115
Chapter 9. Conclusions	124
9.1. The Galactic Center Magnetosphere	124
9.2. Future Work	130
References	132

List of Tables

3.1	Matrix representations of optical elements.	27
5.1	Results of Pointing Model Fit	39
5.2	SPARO Characteristics from Renbarger (2002)	44
5.3	Results for Noise Floor Estimates	48
5.4	Derived Values for 450 μm Fluxes as a Function of n	50
6.1	Grid Test Results	52
6.2	Polarization Efficiencies	55
6.3	Parameter List for Observing Model	59
6.4	Observing Model	61
6.5	IP Fit Results for Sgr B2 Observations	63
6.6	IP Fit Result for Moon Observations	64
6.7	Final IP Matrix	67
6.8	Overlap Candidates	77

6.9	SPARO Polarimetry Results	78
7.1	Polarization Results for M-0.13-0.08	84
7.2	Polarization Results for 50 km s ⁻¹ Cloud, Position 1	85
7.3	Polarization Results for 50 km s ⁻¹ Cloud, Position 2	86
7.4	Polarization Results for 50 km s ⁻¹ Cloud, Position 3	87
7.5	Polarization Results for 50 km s ⁻¹ Cloud, Position 4	88
7.6	Polarization Results for 50 km s ⁻¹ Cloud, Position 5	89
7.7	Polarization Results for 50 km s ⁻¹ Cloud, Position 6	90

List of Figures

2.1	Anatomy of the Central 30 Parsecs at 20 cm	9
3.1	Paramagnetic Relaxation	15
3.2	Stokes' Coordinate System	30
5.1	Pointing of SPARO	40
5.2	Final SPARO Pointing	42
5.3	Plots of Polarization Uncertainty Versus τ	47
6.1	Stokes' Coordinate System	53
6.2	Source and Array Maps	54
6.3	Source Polarizations for Sgr B2	65
6.4	Source Polarizations for the Moon	66
6.5	The Final Instrumental Polarization Matrix	68
6.6	The Difference Between the Sgr B2 and Moon Fits for Instrumental Polarization	69

6.7	Quantification of Snow Coverage	71
6.8	Results of Snow on the Tertiary Mirror	72
6.9	Snow Effect II	73
6.10	Time Variability Study	74
6.11	Edge Effect	76
6.12	SPARO Polarimetry Results of the Galactic Center	79
8.1	Field Geometries in a Cylindrical Basis	92
8.2	SPARO Galactic Center Polarimetry Results	94
8.3	Galactic Center Polarimetry and 850 μm Photometry	97
8.4	Galactic Center Polarization and 20 cm Continuum	101
8.5	Galactic Center Polarization and CS Velocity Maps	102
8.6	X Polarization Feature	103
8.7	Galactic Center Polarization and 90 cm Continuum	105
8.8	Galactic Center Polarization and MSX 8 μm Photometry	106
8.9	Analysis of Radius of Curvature for GC Polarimetry Arc	107
8.10	Hertz P versus SHARC F/F_{SgrB2}	109
8.11	SPARO P versus F/F_{SgrB2}	111

8.12	Polarization Angle Versus Δl	116
8.13	Polarization Angle Versus Flux	118
8.14	Polarization Angle Versus Binned Flux	119
9.1	Model for Molecular Cloud Production of NTFs	126
9.2	Comparison of Models for Magnetic Reconnection in the Sickle	129

CHAPTER 1

Introduction

Located in the constellation Sagittarius, the Galactic center is an extremely complex and interesting astrophysical system. The vast array of different types of matter and energy that interact in this arena make it difficult to decode the physical processes at work. In addition, the limitations imposed by intervening dust that obscures our view of the Galactic center necessitate resorting to wavelengths longward of near-infrared and shortward of ultraviolet for its study.

The Galactic center is interesting for two important reasons. First of all, the very geometry of a spiral galaxy implies the importance of the central bulge. It is from this structure that the beautiful arms of star formation spiral outward and diffuse into intergalactic space. In vicinity of the Galactic center, matter is found in forms that we readily recognize: ionized gas, atomic gas, molecular gas, dust, stars, and even a central black hole believed to have a mass 2.6 million times that of our sun. However, conditions in the Galactic center are very different from those in the disk of the Galaxy. Here, matter and energy densities are much higher than

those of the solar neighborhood, which are believed to be representative of the disk of the Milky Way.

The second reason why the Galactic center has attracted the attention of astronomers is that it is the closest example we have of an Active Galactic Nucleus (AGN). For decades, astronomers have looked at extragalactic objects such as Quasars, Blazars, Seyferts, and Liners. These objects have extremely high and often time-variable luminosities. This combination has inspired the theory that these objects are gravitational engines powered by matter accreting onto supermassive black holes (Mezger, Duschl and Zylka 1996). Our detailed understanding of the process, however, has been limited by our inability to spatially resolve the centers of these objects.

The Milky Way's central engine is powered by a central object of modest mass and low luminosity and hence lies on the unspectacular end of the AGN family. Even so, it shares some interesting characteristics with its larger cousins. Time variability has been observed in the X-ray emission from Sagittarius A* (Sgr A*), the compact radio source coincident with the dynamical center of the Galaxy (Baganoff et al. 2001). We see increasingly conclusive evidence that this central object is indeed a black hole (see chapter 2). Our own Galactic center is so close to us (8.5 kpc compared to thousands of Mpc for quasars) that it offers incomparable insight into the workings of the central engines of galaxies.

One source of energy believed to be important in the Galactic center is that associated with magnetic fields. Despite this fact, little is known about the interaction of magnetic fields with matter and energy both on large scales (Galactic rotation) and on small scales (kinematics of gravitationally bound entities).

Polarimetry of far-infrared and submillimeter thermal emission from magnetically aligned dust grains is known to be a tracer of magnetic field direction projected onto the plane of the sky; however, due to the uncertainties regarding the line-of-sight field and alignment efficiency, this method has been of limited value for estimates of the strength of the field. Because the Galactic center contains large amounts of dust, this technique has the advantage of providing information about the magnetic field at most locations in this region. In contrast, techniques such as Faraday rotation measurements and Zeeman splitting are limited. Faraday rotation measures can only be done for strong radio sources that are polarized, while Zeeman splitting suffers from confusion produced by Doppler-broadened lines.

The thesis is composed of two parts. The first details the calibration of the South Pole 450 μm polarimeter, SPARO (The Submillimeter Polarimeter for Antarctic Remote Observing) (Dotson et al. 1998). SPARO's 6' beam size provides for little sensitivity to the fine details, but provides good coverage over a large portion of the Galactic center. The second part of this thesis presents results of submillimeter polarimetry of the Galactic center using SPARO and also

Hertz, a 350 μm polarimeter operated at the Caltech Submillimeter Observatory on Mauna Kea, Hawai'i (Dowell et al. 1998). Hertz's 0.3 spatial resolution allows for probing structure on smaller scales than SPARO can at the expense of spatial coverage. Together, these two data sets lend credence to Galactic center magnetosphere models that involve the gravitational shearing of an initially poloidal field into one that is toroidal.

Radio observations dating back to the 1980's have provided evidence for large-scale poloidal fields at the Galactic center (see chapter 2). Meanwhile, the data taken with SPARO in Austral Winter 2000 provide convincing evidence that the large scale structure of the field is oriented parallel to the plane of the Galaxy, consistent with a toroidal field. The Hertz data shows that on finer scales, both kinds of fields are visible and the magnetic field direction is correlated with the density of the material. In less dense regions, we find that the field is poloidal while in the denser regions, the field is more toroidal, most likely as a result of gravitational shearing. Comparing these regions allows us to obtain the first estimate of the field strength in the Galactic center to be derived from submillimeter polarimetry.

Chapter 2 gives an overview of the Galactic center, providing details concerning the current state of understanding of this environment, but focusing primarily on

the magnetosphere. Methods for measuring magnetic fields are reviewed. Chapter 3 delineates the principles of submillimeter polarimetry, including grain alignment and polarization mechanisms. Chapter 4 presents the details of the SPARO design and deployment. Chapters 5 and 6 discuss the photometric and polarimetric calibration of SPARO, respectively. Chapter 7 introduces Hertz and details the analysis of the Hertz data. Finally, these data are interpreted in chapter 8 and conclusions are discussed in chapter 9.

CHAPTER 2

The Galactic Center: An Overview

2.1. The Environment

The Milky Way is a spiral galaxy that is about 25 kpc in diameter. Our solar system is located in one of its spiral arms, approximately 8.5 kpc from the center. At a radius of about 3 kpc, the transition between the flat spiral disk and the elliptical bulge is observed (Mezger, Duschl and Zylka 1996). Within this bulge, the kinematics are complicated due to the existence of a bar that extends to 2.4 kpc and is inclined to our line of sight by $\sim 16^\circ$ (Binney et al. 1991). Inside of this bar, the stable closed orbits are elongated, and into a radius of about 200 pc, they lie with their long axes parallel to the bar. Such orbits are referred to as x_1 orbits. At roughly 200 pc, stable orbits (called x_2 orbits) are those elongated perpendicular to the axis of the bar. The 200 pc transition between x_1 and x_2 orbits is the site of many collisions between clouds and also approximately coincides with a transition between atomic and molecular phases of Hydrogen and hence marks the outer boundary of the Central Molecular Zone (CMZ) (Morris and Serabyn 1996). The frequent collisions in this region are thought to explain the existence of molecular clouds in the CMZ that do not follow Galactic orbits, but rather fall in toward the Galactic center (Davidson 1996).

The CMZ is characterized by densities, velocity dispersions, and temperatures that are higher than for molecular clouds in the disk. It has been estimated that this region contains a gas mass of $5 - 10 \times 10^7 M_{\odot}$ (Morris and Serabyn 1996). In this thesis, the term “Galactic center” will refer to the region interior to a radius of 200 pc.

At optical wavelengths, the Galactic center is obscured from our view by 30 magnitudes of dust extinction, mostly associated with the Galactic disk. In the infrared, it becomes visible long-ward of about $5 \mu\text{m}$. At these mid-infrared wavelengths, thermal emission from stars and hot dust combine with the more complicated spectra of polycyclic aromatic hydrocarbons (PAHs) to produce most of the luminosity of the CMZ. Infrared observations of high proper motion stars in the central parsec (Ghez et al. 1998) have shown that the $2.6 \times 10^6 M_{\odot}$ central mass is confined to a volume smaller than 10^{-6}pc^3 . This is convincing evidence for the existence of a massive central black hole, because orbital instability arguments now rule out competing theories involving clusters of dim objects such as brown dwarfs and white dwarfs.

Moving into the far-infrared, the more abundant cold dust begins to dominate the continuum emission. In the submillimeter, the Galactic center appears to be filled with clouds of cold dust, the line of sight kinematics of which can be measured via emission lines of molecules such as CS (Tsuboi, Handa and Ukita 1999) and CO (Bania 1977). These lines are generally located in the millimeter region. At wavelengths greater than 1 cm, the dust emission tapers off significantly, leaving the continuum to be dominated by diffuse sources of hot gas that are optically

thin. At shorter wavelengths in this regime, we see mostly thermal bremsstrahlung sources that are characterized by flat spectra. Figure 2.1 shows a 20 cm image of a 30 pc region including Sgr A*. Here one can observe clouds of optically thin ionized gases such as the Sickle, the Arched Filaments, and Sgr A West. Sgr A West is an H II region believed to trace the inner edge of the Circumnuclear Disk (CND), a molecular structure encircling Sgr A* at a radius of a few pc. Moving to even longer wavelengths, the power law spectra of non-thermal sources begins to dominate. At these wavelengths, one can see the so-called Non-Thermal Filaments (NTFs) and Sgr A East, the radio source centered near Sgr A* and believed to be the remnant of an explosion. The long, unusually straight NTFs, of which the Galactic Center Radio Arc (GCRA) forms the largest group, run perpendicular to the Galactic plane and are believed to trace strong and organized magnetic fields (see § 2.2).

Short-ward of optical wavelengths, the Galactic center is beginning to be explored by the Chandra space-borne X-ray telescope. At these energies, compact sources are visible, the most prominent of which is Sgr A*. Here, it is possible to see what is believed to be radiation from gas heated by black hole accretion. The recent Chandra Galactic Center Survey (Wang, Gotthelf and Lang 2001) has shown the spatial extent of million degree gas to be similar to that of molecular gas and dust (Pierce-Price et al. 2000), covering most of the CMZ.

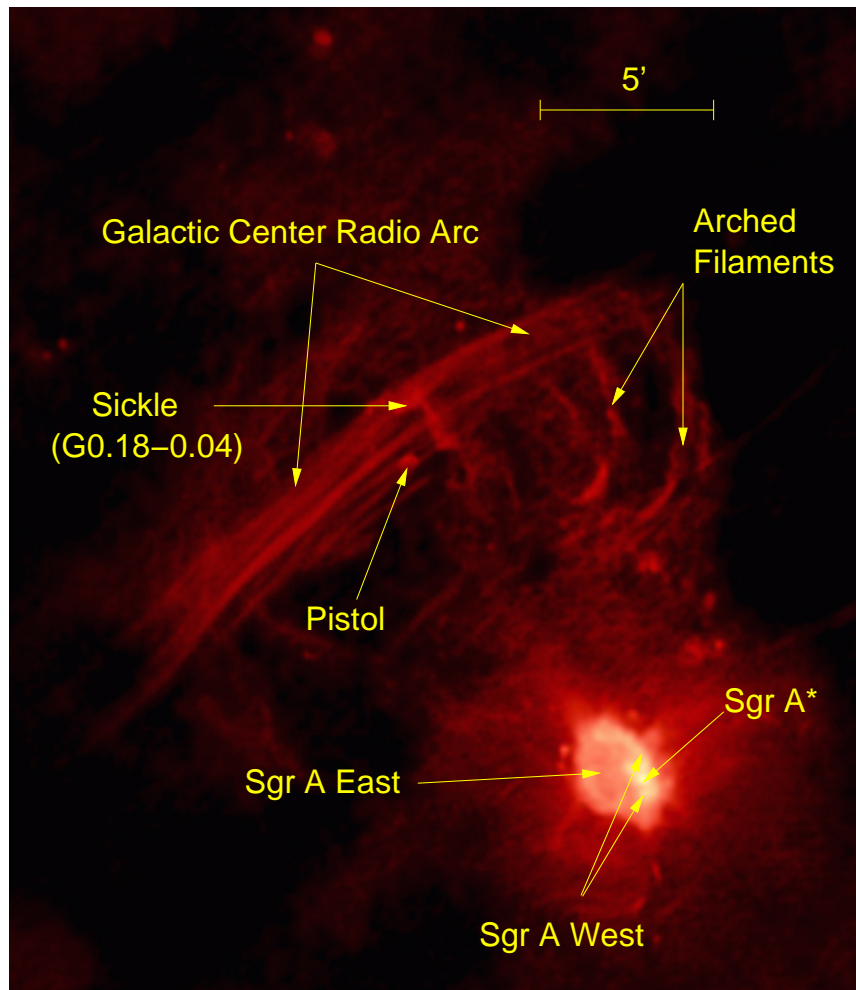


Figure 2.1. This 20 cm image (Yusef-Zadeh, Morris and Chance 1984) of the central 30 parsecs of the Milky Way shows some of the interesting phenomena of the Galactic center. At 20 cm, some synchrotron radiation is observed (the Galactic Center Radio Arc and Sgr A East), but bremsstrahlung from H II regions such as the Sickle, the Arched filaments and Sgr A West is also quite visible.

2.2. The Galactic Center Magnetosphere

The structure of magnetic fields and their subsequent effects on the dynamics in this region are not well known; however, determining the structure and strength

of these fields is crucial to developing an understanding of the structure of the Galaxy for several reasons. First, in the solar neighborhood, the energy density associated with the interstellar magnetic field is comparable to that associated with gas kinetic energy, radiation energy, and cosmic ray energy. The same relationship could hold in the Galactic center. Second, the magnetic field is well coupled, via flux-freezing, to matter (see § 3.1.2). Finally, magnetic fields are believed to be important for dynamics of AGN via angular momentum transport in accretion disks and jet dynamics.

The first evidence to be found for the existence of magnetic fields in this region lies in the morphology of the Non Thermal Filaments (NTFs), the most impressive examples of which are found in the Galactic Center Radio Arc (GCRA) (Yusef-Zadeh, Morris and Chance 1984). Polarization measurements (corrected for Faraday rotation) indicate that the NTFs are composed of relativistic electrons spiraling around magnetic field lines (Tsuboi et al. 1986). Within 20° , almost all of the NTFs in the Galactic center region are aligned with their long axes perpendicular to the plane of the Galaxy. This observation led to the idea that these filaments trace the inner part of a dipole magnetic field that has ever since been referred to as a poloidal field.

It has been observed that in many cases NTFs are interacting with Galactic center molecular clouds. The best example of this is in the center of the GCRA where the 25 km s^{-1} molecular cloud associated with G0.18-0.04 (the Sickle) is superposed on the filaments (Serabyn and Güsten 1991) (see fig. 2.1). The lack of observed distortion of the filaments allows one to set a lower limit for the strength

of the magnetic field. This argument yields $B > \text{few mG}$ (Morris and Serabyn 1996).

Two possibilities have been proposed for the relationship between these filaments and the overall field structure. First, the NTFs could be local enhancements or “flux tubes” in a poloidal field that is generally much weaker. In this scenario, a strong confinement mechanism is required to prevent the NTFs from disappearing on time scales of 300 years (Morris and Serabyn 1996). The second possibility is that a significant fraction of the Galactic center is filled with a mG field that is poloidal. However, the concern here is that such a field would dominate the dynamics of the central 100 pc. In addition, the field is known to fall off away from the plane of the Galaxy, as field strengths of 10-100 μG have been measured in high-latitude extensions of the GCRA (Tsuboi et al. 1986).

Another unknown concerning the GCRA is the mechanism by which the relativistic electrons are produced. One proposed explanation is magnetic reconnection via molecular cloud-NTF collisions (Davidson 1996). There are two ways in which this can happen. Either the cloud can locally distort the field in the filaments causing it to reconnect with itself, or the magnetic field in the cloud can reconnect with the field in the filaments.

Far-infrared and submillimeter polarimetry have provided evidence that the field in the dense molecular clouds is not consistent with the poloidal field traced by the filaments. Novak et al. (2000) have shown that in the molecular cloud M-0.13-0.08, the field is parallel to the Galactic plane, indicating that gravitational rotation and infall have sheared out the field. In addition, 60 μm polarimetry of

the molecular cloud associated with the Sickle has shown the field to be parallel to the Galactic plane (Dotson et al. 2000).

Uchida et al. (1985) have constructed a model that connects poloidal and toroidal fields. Because the magnetic flux is frozen into the matter (see § 3.1.2), differential rotation can shear an initially poloidal field into a toroidal one in sufficiently dense regions of the Galactic center. This model predicts that the direction of the line of sight component of the magnetic field should alternate in each of the four quadrants of the Galactic center (see § 8.1). Faraday rotation measures which are capable of measuring the line of sight component of the magnetic field have shown that this is indeed the case (Novak et al. 2002).

Over the past two decades, much has been learned concerning the composition and kinematics of the Galactic center; however, little is known about the role of magnetic fields here. Although data pertaining to the geometry of the field are suggestive, additional data are required for a complete understanding.

CHAPTER 3

Magnetic Fields and Polarimetry

3.1. Grain Alignment and Astrophysical Magnetic Fields

We have stated that polarimetry is a technique by which we can probe magnetic field direction, but until now we have omitted the details of the physics upon which this technique relies. The first aspect of the underlying physics that is important is that involved in producing partially-polarized radiation. The second aspect involves a description of the interaction of the magnetic fields with matter.

3.1.1. Polarization Mechanisms

In order for dust to produce polarized radiation by emission or absorption, it is necessary for the grains to be aligned. Such alignment is believed to be possible via the action of magnetic fields that run through these massive molecular clouds, the dynamics of which are described by the magnetohydrodynamic equations in § 3.1.2.

Dust grains are generally not in thermal equilibrium with the gas with which the dust coexists. In fact, the dust is generally much colder (Purcell 1979). However, atomic collisions, photoelectric emission of electrons by a grain, and hydrogen molecule production can all serve to produce suprathermal rotation of a grain.

In this case, the rotational kinetic energy of a typical grain is greater than that expected by equipartition when the grain is in thermal equilibrium with the gas.

Internal processes in each grain can decrease its rotational kinetic energy. An example of such a process is the inelasticity of the grain material under stresses induced by centrifugal forces. Because such processes are internal to each grain, they cannot decrease its total angular momentum. The minimum energy a grain can have for a constant value of angular momentum occurs for the case in which the grain is spinning about its axis of greatest moment of inertia. Because the time scale for this process is much shorter than that for spin-up processes (Purcell 1979), it is believed that a majority of grains will relax to this low energy state.

Though there is much debate over the details of the alignment mechanism (Lazarian 2000), it is generally agreed that alignment occurs due to magnetic fields and that a grain aligns such that its angular momentum axis is parallel to the ambient magnetic field. One alignment mechanism commonly invoked in explaining polarization from dust grains is paramagnetic relaxation (Davis and Greenstein 1951). This assumes quite self-evidently that the grains are paramagnetic (or in some cases, when infused with deposits of iron, super-paramagnetic). Figure 3.1 illustrates this phenomenon. When a grain spins in the presence of a magnetic field, the magnetic domains of the grain will align with the magnetic field as shown in figure 3.1A. However, if the spin axis does not coincide with the direction of the magnetic field, the domains will be immediately pulled out of alignment with the magnetic field by the grain's angular momentum as demonstrated in figure 3.1.

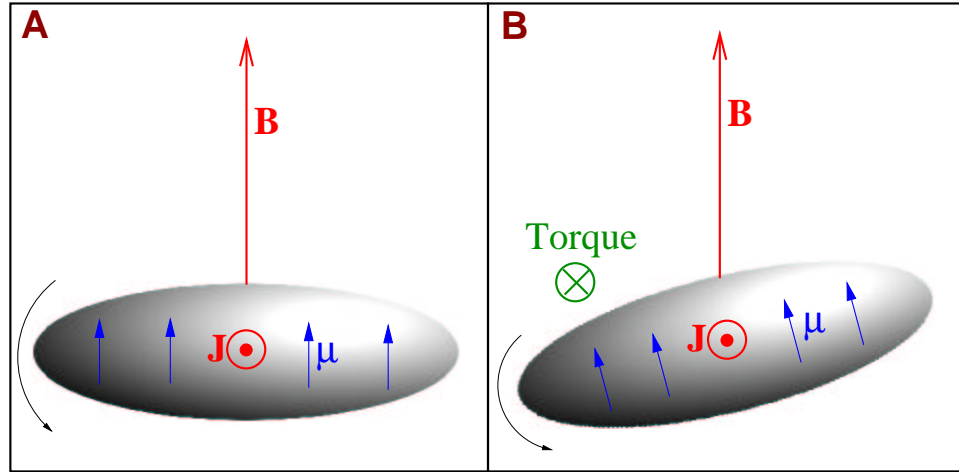


Figure 3.1. Dust grains are commonly represented by prolate spheroids. Imagine a dust grain spinning about its axis of greatest moment of inertial such that this axis is not co-aligned with the ambient magnetic field. If the dust grain is paramagnetic, the magnetic domains in the grain align parallel to the magnetic field (A). As the grain spins, the domains are pulled out of alignment with the magnetic field (B). This produces a torque on the grain ($\vec{\mu} \times \vec{B}$) that opposes the angular momentum of the grain.

This misalignment created a torque on the grains ($\vec{\mu} \times \vec{B}$) that is in the opposite direction of \vec{J} . After a slight misalignment, the domains are re-aligned with the field and the process continues. By this process, the spin axes of grains are preferentially aligned with the magnetic field.

The temperatures of these grains (typically 20-100 K in molecular clouds) are such that they emit thermal radiation in the submillimeter and far-infrared. The emissivity is dependent on the ratio of the wavelength of emitted light to the linear scale of a grain. As this ratio increases, the emissivity of a grain decreases such that longer wavelengths, the dust becomes more transparent. It is this effect that allows

us to see through to the denser dust at the center of the Galaxy at wavelengths long-ward of the visible part of the electromagnetic spectrum. Most models of the emission handle this dependency by employing a blackbody spectrum modified by an emissivity law that decreases as a power of the wavelength. This type of spectrum is often called a “greybody spectrum.”

If one dimension of the grain is slightly different than another, the emissivities of the linear polarization states parallel to each of the grain dimensions will differ slightly and the grain will emit linearly polarized radiation. If a significant fraction of the grains in a cloud are aligned by a magnetic field, then the resultant polarization from all of the grains in a telescope beam will be perpendicular to the field.

A similar scenario holds for the case where there is a hot source behind cold dust. An example of this is the optical and near-infrared polarization of starlight by dust in the Interstellar Medium (ISM). In this case, the dust selectively extinguishes the polarization component of the starlight having an electric field that is parallel to its axis of greatest moment of inertia. The measured polarization is then oriented perpendicular to this axis. Assuming the same alignment mechanism as above, the polarization in the case of absorption is *parallel* to the interstellar magnetic field.

3.1.2. Magnetohydrodynamics

Magnetohydrodynamics, or MHD, essentially involves grafting the Maxwell equations onto hydrodynamics to achieve a description of the dynamics of a conducting,

magnetized fluid. The model is one in which matter and fields interact in a specific manner under a given set of assumptions. These assumptions posit a neutral, ionized medium that has no magnetic permeability and is dense enough such that the rate of change of electromagnetic fields is small compared to the collisional frequency of the ions. In this regime, Ohm's law applies, and the conductivity is calculable via force balancing (Jackson 1975).

$$(3.1) \quad \mathbf{J} = \sigma \mathbf{E}' = \sigma \left(\mathbf{E} + \frac{1}{c} (\mathbf{v} \times \mathbf{B}) \right)$$

Here, \mathbf{E}' is the electric field in the rest frame of the medium and \mathbf{E} and \mathbf{B} are the electric and magnetic fields in a laboratory frame relative to which the medium is moving with a non-relativistic velocity \mathbf{v} . Since this is a neutral fluid, the charge density in either frame is zero.

Under the MHD assumptions, the Maxwell equations relating magnetic and electric fields are

$$(3.2) \quad \nabla \times \mathbf{E} = -\frac{1}{c} \frac{\partial \mathbf{B}}{\partial t}$$

and

$$(3.3) \quad \nabla \times \mathbf{B} = \frac{4\pi}{c} \mathbf{J}.$$

Here, the requirement that the collisional frequency of the electrons be high compared to the time variation of the fields allows for the omission of the displacement current, since in this model, the fields cannot separate the charges.

Putting these equations together yields the following equation for the fields.

$$(3.4) \quad \frac{\partial \mathbf{B}}{\partial t} = \nabla \times \mathbf{v} \times \mathbf{B} + \frac{c^2}{4\pi\sigma} \nabla^2 \mathbf{B}$$

For fluids at rest, the curl term vanishes and the result is simply the diffusion equation

$$(3.5) \quad \frac{\partial \mathbf{B}}{\partial t} = \frac{c^2}{4\pi\sigma} \nabla^2 \mathbf{B}.$$

Solutions of (3.5) are of the form $\mathbf{B} = \mathbf{B}_0 e^{-t/\tau}$. Thus the magnetic field decays on a time scale of $\tau = 4\pi\sigma L^2/c^2$ where L is a length characteristic of the system.

On the other hand, if the conductivity is high and the length scales are large, the curl term dominates.

$$(3.6) \quad \frac{\partial \mathbf{B}}{\partial t} = \nabla \times \mathbf{v} \times \mathbf{B}$$

Equation 3.6 implies that the magnetic flux through a loop stationary with respect to matter is conserved. This phenomenon is known as “flux freezing.”

Typical values of conductivity in the interstellar medium are of the order of $1 \times 10^{10} \text{ s}^{-1}$ (In SI units, this converts to about $1.1 \text{ } \Omega \text{ m}^{-1}$) (Spitzer 1998). Given

such conductivity, the time scale for ohmic diffusion over scales of 5 pc (a typical size for molecular clouds in the Galactic center) is $\sim 10^{19}$ years. Since this is older than any current reasonable estimate of the age of the universe, diffusion is not appreciably important in molecular clouds. The magnetic field lines become stretched, pulled, twisted, and compressed as the matter is stretched, pulled, twisted and compressed. However, doing such things to magnetic fields causes other forces to appear. The magnetic force is simply the Lorentz force in the absence of free charges:

$$(3.7) \quad \frac{1}{c}(\mathbf{J} \times \mathbf{B}) = -\frac{1}{4\pi}\mathbf{B} \times (\nabla \times \mathbf{B}).$$

Here we have made use of (3.3). It can be seen from (3.7) that the force is always perpendicular to the magnetic field lines, but using some vector identities allows the right hand side of this equation to be written in the form

$$(3.8) \quad -\nabla \left(\frac{B^2}{8\pi} \right) + \frac{1}{4\pi}(\mathbf{B} \cdot \nabla)\mathbf{B}.$$

The first term can be interpreted as the negative gradient of a magnetic pressure. Note that magnetic pressure is equivalent to the energy density of the field. Thus, as magnetic fields become compressed, this term resists further compression. The second term is a tension along the field lines that provides a force against bending the material. The existence of magnetic field lines in large clouds can have effects such as providing support against gravitational collapse.

3.2. Polarimetry

The system chosen for classifying polarization of incoming radiation in a given astronomical study is generally tailored to the science of interest. For example, in measuring the polarization of the Cosmic Microwave Background, it is customary to decompose the polarization over a broad region of the sky into curl-free and divergence-free modes. Such a non-local approach is convenient scientifically because the physical sources of these two modes are expected to be different. Curl-free modes are believed to be produced at the surface of last scattering via Thompson scattering of thermal radiation from quadrupole anisotropies in the CMBR. The divergence-free modes are expected to originate earlier, resulting from primordial gravitational waves.

By contrast, when using polarization to probe magnetic fields in Galactic molecular clouds, the ideal polarization characterization scheme involves the use of Stokes' parameters. Here we are concerned with the detailed spatial structure, and Stokes' parameters provide a complete local description of the polarization at each measured point in a cloud.

Stokes' parameters are easily extracted from instruments which employ dual arrays of bolometers (such as Hertz and SPARO) using fairly straightforward optical techniques.

3.2.1. Stokes' Parameters

For the simple case of monochromatic light, the electric field associated with radiation can be described in terms of its space and time variations with a complex vector amplitude.

$$(3.9) \quad \mathbf{E}(\mathbf{x}, t) = \mathbf{E}e^{i\mathbf{k}\cdot\mathbf{x}-i\omega t}$$

Here, \mathbf{E} is the complex vector amplitude of the wave in the plane perpendicular to \mathbf{k} that contains all of the information about the polarization state of the radiation. For monochromatic light, waves always add coherently such that the radiation is always 100% polarized.

In reality, however, light is never perfectly monochromatic. Incoherent superpositions of waves of differing frequencies make \mathbf{E} a cumbersome way of characterizing the polarization. Instead, the tradition is to re-parameterize the components of \mathbf{E} and their relative phase into four Stokes' parameters that are measurable for both monochromatic and polychromatic light. In the following discussion, Stokes' parameters are introduced as a re-parameterization of the vector amplitude of a monochromatic wave. They are then extended to the concept of polychromatic light. Since we are concerned with measuring polarization, in this approach we will keep in mind the techniques used to measure the Stokes' parameters.

We begin with (3.9), the equation for a monochromatic electromagnetic wave. The first step in the re-parameterization is to choose a two-dimensional basis for this vector. A very natural, though certainly not unique, choice of basis is a set of

two real, orthogonal unit vectors (e.g. two Cartesian unit vectors). In this basis (3.9) becomes

$$(3.10) \quad \mathbf{E} = (a_1 e^{i\delta_1} \hat{\epsilon}_1 + a_2 e^{i\delta_2} \hat{\epsilon}_2) e^{i\mathbf{k}\cdot\mathbf{x} - i\omega t}.$$

Here, a_1 and a_2 are the real amplitudes of the complex vector components, and δ_1 and δ_2 are the respective phases for each component. With this choice of unit vectors, the first Stokes' parameter, Q , is simply the difference between the flux observed with electric field parallel to each of these unit vectors. From an instrumentation standpoint, this corresponds to placing a wire grid in the path of light, taking a flux measurement, rotating the grid by 90° and repeating the measurement. The difference of the two fluxes is defined to be Q (Jackson 1975), and in terms of the complex amplitude of the electric field, it is expressed as

$$(3.11) \quad Q = |\hat{\epsilon}_1 \cdot \mathbf{E}|^2 - |\hat{\epsilon}_2 \cdot \mathbf{E}|^2 = a_1^2 - a_2^2.$$

Here, as in (3.10), $\hat{\epsilon}_1$ and $\hat{\epsilon}_2$ are two orthogonal unit vectors in the plane of the sky that correspond to the directions of the two orientations of the wire grid in our hypothetical instrumental measurement. The squares of the magnitudes of the quantities are required since the energy (the quantity measured by our detectors) is proportional to the square of the electric field amplitude.

Since three quantities are necessary to completely describe the polarization state of the incoming radiation, two more Stokes' parameters are introduced. These

involve the amplitudes and the relative phase between the components.

$$(3.12) \quad U = 2 \Re[(\hat{\epsilon}_1 \cdot \mathbf{E})^*(\hat{\epsilon}_2 \cdot \mathbf{E})] = 2a_1a_2 \cos(\delta_2 - \delta_1)$$

$$(3.13) \quad V = 2 \Im[(\hat{\epsilon}_1 \cdot \mathbf{E})^*(\hat{\epsilon}_2 \cdot \mathbf{E})] = 2a_1a_2 \sin(\delta_2 - \delta_1)$$

U and V can be thought of as the “in phase” and “out of phase” parameters. Once Q is measured, U gives an indication of how much the major axis of the polarization vector differs from that which defines Q (as fixed by the choice of basis vectors that are defined by the initial grid orientation). To the extent that the two components are “in phase” (as given by the value of the cosine of their relative phase difference), the real orthogonal components of \mathbf{E} will simply add and constitute a linear polarization in a direction given by the resultant of the two vectors. V gives an indication of how out of phase the two components are. If the components are out of phase, the resultant of the electric field will rotate in an elliptical pattern, the eccentricity and orientation of which are determined by Q and U . If both Q and U are zero and V is non zero, this pattern becomes circular. From this, it can be seen that V is a measure of the degree of circular polarization of the radiation.

The above choice of basis is not unique. One can easily transform into bases in which U or V take the simple form of a difference between components. The phase information then becomes contained in the remaining two parameters. To get U in a simple form, it is only necessary to rotate the above basis vectors by 45° . V 's simple form comes from using a set of complex basis vectors.

It will be seen in the discussion of Stokes' vectors and matrices that through the use of specialized optical elements, it is possible to transform one Stokes' parameters into another. Thus, one can measure U and V by transforming them each into Q and using the two detector differencing technique described above.

To complete the discussion of Stokes' parameters for monochromatic light, we introduce the Stokes' parameter I which is simply the total intensity of the incoming radiation.

$$(3.14) \quad I = |\hat{\epsilon}_1 \cdot \mathbf{E}|^2 + |\hat{\epsilon}_2 \cdot \mathbf{E}|^2 = a_1^2 + a_2^2 = \sqrt{Q^2 + U^2 + V^2}$$

Because monochromatic light is by definition completely polarized, the total power of an electromagnetic wave can always be divided among the three polarization states.

In reality, however, incoming radiation is composed of a superposition of waves which vary in phase, frequency, and amplitude. Because of this superposition, the electric fields will not generally add coherently. This condition allows for unpolarized or partially-polarized light. In this case, the definitions of the Stokes' parameters given above must be modified slightly such that they are equal to the

time averages of the quantities related to the complex amplitude vector.

$$(3.15) \quad I = \langle a_1^2 + a_2^2 \rangle$$

$$(3.16) \quad Q = \langle a_1^2 - a_2^2 \rangle$$

$$(3.17) \quad U = \langle 2a_1a_2 \cos(\delta_2 - \delta_1) \rangle$$

$$(3.18) \quad V = \langle 2a_1a_2 \sin(\delta_2 - \delta_1) \rangle$$

All four Stokes parameters are necessary since the possibility of unpolarized light provides an additional degree of freedom such that

$$(3.19) \quad I^2 \geq Q^2 + U^2 + V^2.$$

For polychromatic radiation, Stokes' parameters from different sources along the line of sight are additive in contrast to the case for monochromatic light in which the electric fields are additive.

3.2.2. Normalized Stokes Parameters and Stokes Matrices

For measuring linear polarization, it is convenient to introduce the normalized stokes parameters ($1, q = Q/I, u = U/I, v = V/I$). These now relate to the fraction of incoming light which contributes to each component of polarization.

Typical submillimeter and far-infrared polarimeters such as Hertz and SPARO are designed using polarizing grids that consist of taught, finely-spaced wires that

are suspended parallel to one another. These grids reflect the component of radiation in which the electric field is parallel to the wires and transmit the orthogonal component. Two arrays of detectors are used to capture these two polarization components of the radiation. Thus, the polarimeter is set up to measure one of the linear Stokes' parameters (by convention, this is designated q , but in reality, it is just as easy to call this u since they are related by a 45° rotation of the basis).

The question then arises of how to measure u , the other linear Stokes' parameter. A device that has the capability of retarding one component of the electric field by half of a wavelength with respect to its orthogonal counterpart produces an effect such that the linear polarization vector is reflected about one of the axes of the retardation (it does not matter which because polarization is a pseudo-vector; i.e. it is invariant under inversion in the plane of the sky). Such a device is capable of mapping one pair of linear Stokes' parameter into a different linear combination of q and u . An example of this type of device is a half-wave plate. A half-wave plate consists of a piece of birefringent quartz cut to a width $z = (2N - 1)\lambda/2(n_2 - n_1)$ where λ is the wavelength of interest, N is a positive integer, and n_2 and n_1 are the indices of refraction for the fast and slow axes, respectively.

It should be noted here in passing that a quarter wavelength retardation can map v into q and u and vice versa; however the focus of this investigation is on linear polarization and the rest of the thesis will focus on q and u .

To represent optical elements that affect the Stokes' parameters, it is convenient to define a four-component Stokes' vector: $(1 \ q \ u \ v)$ such that optical components can be represented by vectors and matrices. Table 3.1 gives some examples.

Mirror (M)	$\begin{pmatrix} 1 & 0 & 0 & 0 \\ 0 & 1 & 0 & 0 \\ 0 & 0 & -1 & 0 \\ 0 & 0 & 0 & -1 \end{pmatrix}$
Half-Wave Plate (H)	$\begin{pmatrix} 1 & 0 & 0 & 0 \\ 0 & \cos(4\theta) & \sin(4\theta) & 0 \\ 0 & \sin(4\theta) & -\cos(4\theta) & 0 \\ 0 & 0 & 0 & 1 \end{pmatrix}$
Horizontal Grid + Detector (G_V)	$\begin{pmatrix} \frac{1}{2} & \frac{1}{2} & 0 & 0 \end{pmatrix}$
Vertical Grid + Detector(G_H)	$\begin{pmatrix} \frac{1}{2} & -\frac{1}{2} & 0 & 0 \end{pmatrix}$

Table 3.1. Matrix representations of optical elements.

3.2.3. Polarization Techniques

Stokes' parameters present a convenient way to connect the theoretical concept of polarized electromagnetic radiation into quantities that can be readily measured. The following discussion describes the techniques used in both SPARO and Hertz to measure q and u , the two Stokes' parameters necessary for a complete description of the linear polarization.

The layout of a typical polarimeter is as follows. The incoming radiation passes through a rotating half-wave plate en route to an analyzer grid that splits the orthogonal components into two separate arrays of detectors. The general picture to keep in mind is that the analyzer and detectors measure q . The half-wave plate turns so as to map a different combination of q and u into q for each angle

at which a measurement is made. The equation that describe this mapping is a simple function of the half-wave plate angle and can be used to extract the linear Stokes' parameters from the data.

In both SPARO and Hertz, dual arrays are used. There are two advantages to doing this. First, because two arrays capture twice as much of the incoming light as the one array alternative, integration times are reduced as compared to the case of a single array. More importantly, measuring the normalized difference between the orthogonal polarizations eliminates effects of varying atmospheric transmission over the time span of an observation. This latter benefit is extremely important since for good weather, the atmospheric transmissions at 350 and 450 μm only approach 35% and can vary over the course of an observation.

In practice, the two arrays, designated R and T for the reflected and transmitted component of the flux with respect to the analyzer grid, are used in the following way. Using the matrices from table 3.1, the following expressions can be derived for R and T .

$$(3.20) \quad R = G_H H S^T = \frac{1}{2}I + \frac{1}{2}Q \cos(4\theta) + \frac{1}{2}U \sin(4\theta)$$

$$(3.21) \quad T = G_V H S^T = \frac{1}{2}I - \frac{1}{2}Q \cos(4\theta) - \frac{1}{2}U \sin(4\theta)$$

Here, S is the Stokes' vector of the incoming radiation described above. Note that for T , we use G_V since transmission by a horizontal grid is identical to reflection by a vertical one.

The normalized difference between these quantities is then simply (Platt et al. 1991)

$$(3.22) \quad \frac{R - T}{R + T} = q \cos(4\theta) + u \sin(4\theta).$$

It must be noted here that Hertz's analysis scheme differs slightly from SPARO's, which is described here. This difference stems from a modification made to optimize the Hertz analysis technique for low signal-to-noise sources (Dowell et al. 1998).

By making measurements at various half-wave plate angles (θ), it is possible to fit these data to the above function and solve for q and u . Note that (3.22) assumes that one of the birefringent axes of the half-wave plate is aligned with celestial north when $\theta = 0$ and that there is no sky nor dewar rotation.

The definition of the half-wave plate matrix implies the coordinate system shown in figure 3.2. For this coordinate system, we can transform from q and u to polarization (P) and polarization angle (ϕ).

$$(3.23) \quad P = \sqrt{q^2 + u^2}, \phi = \frac{1}{2} \tan^{-1} \left(-\frac{u}{q} \right)$$

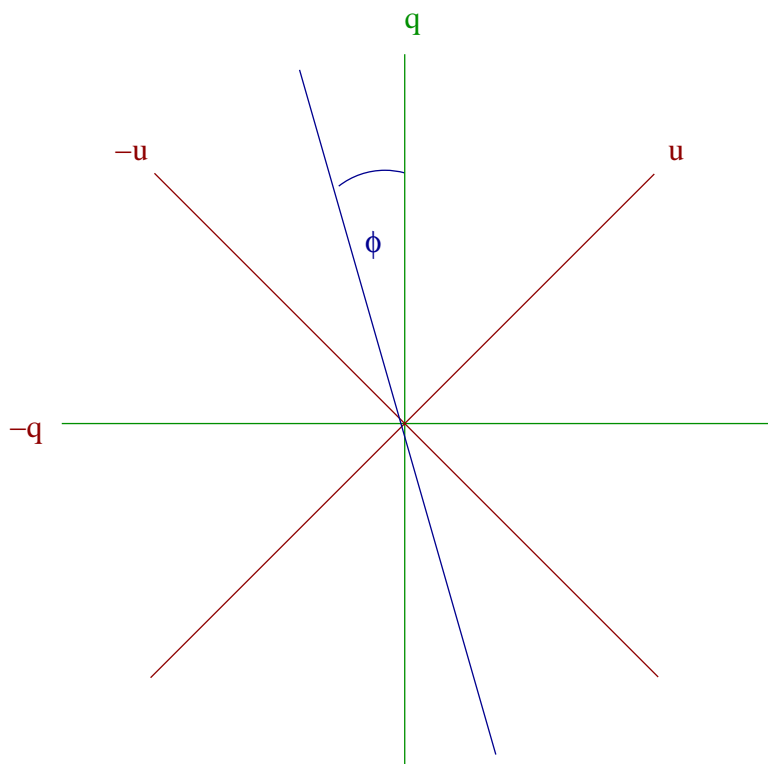


Figure 3.2. Here we show the coordinate system on the sky as defined by the half-wave plate matrix in table 3.1. Here, q is assumed to point to celestial north such that ϕ is measured from north to east.

Note that in 3.2, arrows are omitted from the axes and from the polarization vector to reinforce that polarization is a pseudovector.

CHAPTER 4

SPARO Instrument Overview

The SPARO polarimeter is designed for use at the South Pole’s Viper telescope. The combination of the relatively small collecting area of Viper, the excellent submillimeter transmission of the South Pole’s atmosphere, and the large beam size (6′) optimize the instrument for its primary task of mapping the large scale field in the extended submillimeter emission at the Galactic center.

This chapter provides an overview of SPARO. We discuss the instrument’s unique cryostat, its detectors, and its optics. We finish this chapter with an overview of the observing scheme.

4.1. Cryostat

SPARO’s cryostat utilizes dual ^3He systems in order to cool the detectors to their operating point of 285 mK (Renbarger 2002). The design of the SPARO cryostat is novel due to considerations of the environment in which it is operated. Harsh winter temperatures at the South Pole can reach -100°F , well below the rated temperature limit for elastomer o-rings. To counter this, no unheated o-rings are implemented on this system. All seals between metal surfaces are indium or copper-based.

In order to take advantage of the best submillimeter weather at the South Pole, it is necessary to gather data during the Austral winter. Unfortunately, because of extreme cold and darkness, the South Pole is inaccessible during this time. To overcome this difficulty, a “winter-over” crew is left at the station to run the instruments. Because of difficult working conditions of the winter-overs, care has been taken to make the process of operating SPARO as painless as possible.

Predecessors of SPARO have had multiple cryogens, complicated cycling processes, and relatively short hold times. SPARO’s multiple vapor-cooled shields and 15-liter ^4He reservoir combine to produce a 6 day hold time (Renbarger 2002). This factor of almost 10 improvement over previous instruments significantly reduces the number of outdoor helium fills required during a winter season. In addition, the vapor-cooled shields eliminate the need for the LN_2 reservoir normally responsible for thermal insulation. The dual vapor-cooled shield design relies on thermal contacts at the fill tube to utilize the escaping ^4He vapor to cool the shields. The system operates with negative feedback; as a greater heat load is placed on the ^4He reservoir, more liquid will evaporate, thereby causing a temperature drop in the shields and reducing the heat load on the reservoir. In operation at the South Pole, typical equilibrium temperatures of the OVCS and IVCS are 170 K and 80 K, respectively (Renbarger 2002).

The reservoir and the shields reduce the temperature of the detectors to 4 K. Typically in similar systems the next step in cooling the detectors involves pumping on the reservoir in order to get below the 2 K or so limit necessary to condense ^3He . In the case of SPARO, this is accomplished via a capillary-fed evaporation

refrigerator (DeLong, Symko and Wheatley 1971). In this design, the main ^4He reservoir is connected to a secondary reservoir (the “pumped pot”) via a small (0.005 inch) capillary. The pumped pot is pumped continuously to maintain the smaller reservoir at roughly 1.5 K (Dotson et al. 1998). The advantage of this system for a winter-over at the South Pole is that there is no need to set up a pump on the main reservoir in inclement weather during a cycle.

The pumped pot provides a condensing block for the dual ^3He systems. These are closed systems with charcoal pumps on one end and pots thermally connected to the detectors on the other. By heating the charcoal, ^3He gas is released and condensed into the pots by the pumped pot. After all of the gas has been driven off of the pumps, the pumps are cooled. When the pumps are cooled, they lower the vapor pressure above the newly-condensed liquid to achieve temperatures of 400 and 285 mK for the outer and inner stages, respectively. These vary slightly as a function of the ambient pressure and temperature.

4.2. Detectors

SPARO contains two detector arrays of nine pixels each. The detectors are NTD germanium bolometers mounted in individual cylindrical cavities. Each detector is optically coupled to a non-imaging Winston light concentrator to increase the sensitivity. The bolometers are biased with a current of $75\ \mu\text{A}$. The signals from the bolometers are amplified via JFET source followers which sit in thermally isolated boxes and are self-heated to $\sim 70\ \text{K}$ during operation. The detectors

have been measured to have an electrical NEP of $\sim 1.2 \times 10^{-16} \text{ W Hz}^{-\frac{1}{2}}$ at their operating temperature of 285 mK (Renbarger 2002).

4.3. Optics

The optical path of SPARO is as follows. Light enters the dewar through a diamond dust coated quartz pressure window and passes through a series of filters (black polyethylene at the OVCS, an Infrared Labs C170 blocking filter at the IVCS, and a Queen Mary College Instruments low-pass chemical filter with a cut-on at $180 \mu\text{m}$ at the 4 K snout). The radiation then passes through a field lens that re-images Viper's primary onto the pupil. It continues through the half-wave plate, a $450 \mu\text{m}$ bandpass filter ($\frac{\Delta\lambda}{\lambda} = 0.1$), and a pupil lens, all cooled to 4 K. The pupil lens re-images the sky onto the detector arrays by way of a gold-coated mirror and two orthogonal wire grids. Both lenses and the half-wave plate were anti-reflection (A/R) coated; however, the A/R coating failed during the cooldown. The effect of this failure is unknown but is thought to have contributed to the instrumental polarization described in chapter 5.

The optical efficiency of this system has been measured to be 2.6%. Since these data were taken, the A/R coatings have been re-applied and the filtering scheme revisited to yield a transmission of 8.6% in the current configuration of SPARO.

4.4. Observing Procedure

In the submillimeter, the sky has a non-negligible optical depth. (Typical values are of the order $\tau \leq 1.0$ for extremely good weather. This corresponds to a

transmission of 35%.) Thus, by Kirchoff's law, there is considerable emission from the atmosphere. This atmospheric transmission (or emission) is generally variable in time, and thus the observing scheme must take this into account.

As seen in chapter 3, the dual arrays help in reducing nefarious effects of variations in sky transmission (referred to as "sky noise"), but to compensate for the sky background, a complex system of high frequency and low frequency modulation is invoked.

The high frequency modulation is accomplished by moving a chopping mirror, or "chopper," on the telescope in a square wave pattern such that the detectors are alternatively placed on the source and off the source 0.5° in azimuth. This oscillation is typically done at 3.1 Hz. One cycle of the chopper is called a "chop." The data system automatically demodulates these chops by differencing the on-source and the off-source beams and combines them to produce a "frame," the values of which gets stored to the data file. Typically, for the Galactic center work, we use a value of 2 chops per frame. Successive "frames" are done with the source in the left beam of the chopper cycle to produce an "integration." (For the Galactic center, 24 frames per integration were taken.) Then the telescope is moved in azimuth such that its right beam is placed on the source. In this position, two consecutive integrations are taken before moving the source back to the left beam for a final integration. Each set of four integrations is called a "nod pair" and this process of low frequency modulation is called "nodding." Nodding is essential for eliminating potential signal offsets that are known to be a problem in chopping schemes that are asymmetric.

A polarization file then consists of six nod pairs; one taken at half-wave plate positions of 0° , 30° , 60° , 90° , 120° , 150° . Because polarization is a pseudovector and the polarization angle modulated by the half-wave plate has twice the rotational frequency of the half-wave plate, for 180° rotation of the half-wave plate, there are two complete cycles of the polarization signal. From here, the Stokes' parameters can be found as described in chapter 3. See Hildebrand et al. (2000) for a more complete description.

CHAPTER 5

SPARO Photometric Calibration

5.1. Pointing

Every telescope has errors in its pointing, and it is important to understand these errors along with their effect on the measurements. As our pointing calibration source, we have used the submillimeter peak of Sagittarius B2 (Sgr B2), smoothed to the $6'$ resolution of SPARO. This section details the analysis of the pointing and the development of a pointing model. We then use this pointing model to estimate the errors in pointing for our polarimetric observations.

5.1.1. Sagittarius B2

The pointing model we derived used SPARO observations of Sgr B2. We assumed the coordinates $\alpha_{2000} = 17^{\text{h}}47^{\text{m}}21^{\text{s}}$, $\delta_{2000} = -28^{\circ}23'00''$ for the submillimeter peak of Sgr B2. Later, we were able to verify that the initial coordinates that we assumed for Sgr B2 were correct based on the SHARC $350 \mu\text{m}$ map of the Galactic Center (Dowell et al. 1998). Smoothing the $20''$ beam map to $6'$ resolution using a boxcar filter showed that the migration of the peak when smoothed is negligible. The migration was measured to be under $15''$ which is less than 6% of a SPARO beam.

5.1.2. The Pointing Model

For a given position on the sky, SPARO’s coordinate (designated SSC for “SPARO Source Coordinate”) differs from the actual coordinate by the following relation:

$$(5.1) \quad \Delta = \overline{SPO} - A \sin(2\pi(\phi - \phi_o)).$$

Here $\Delta \equiv \text{SSC} - \text{ASC}$ is the difference between SPARO’s coordinate and the Actual Source Coordinate (ASC).

The first term in (5.1) is simply a constant offset. The second term is a sinusoidal variation due to a slight tilt of the azimuth ring of Viper with respect to the equator of the celestial sphere. A is the amplitude of the pointing modulation produced by this tilt. The zero point of the phase, ϕ_o , is defined as the point on the azimuth ring that corresponds to a right ascension of zero (first point of Aries) on midnight of January 1, 2000 Universal Time (UT). With respect to this convention, the position on the azimuth ring is a function of right ascension and time.

$$(5.2) \quad \phi = -(\text{RA}) \left(\frac{360}{24} \right) + (\text{UT}) \left(\frac{360}{24} \right) + (\text{Day of Year}) \left(\frac{360}{365} \right)$$

The first term is simply the right ascension of the source. The second and third terms are the diurnal and sidereal migration of the right ascension with respect to ϕ_o .

Fit Parameter	Value
\overline{SPO}_α	-0.877 ± 0.011
A_α	0.4 ± 0.2
$\phi_{\alpha(\alpha)}$	$126 \pm 15^\circ$
\overline{SPO}_δ	0.263 ± 0.005
A_δ	2.1 ± 0.2
$\phi_{\alpha(\delta)}$	$37 \pm 8^\circ$

Table 5.1. Results of Pointing Model Fit

The form of the pointing correction is the same for both right ascension and declination. For the case of telescope base tilt, the pointing corrections will be somewhat dependent on declination, and so Sgr B2 is a good choice for a pointing source given that it is located within the boundary of the CMZ.

A two-dimensional Gaussian fit was performed for each observation to find the SSC's of Sagittarius B2 as a function of time. The location of the source as a function of time was fit to (5.1) to find the parameters of the final pointing model. These parameters are displayed in table 5.1. The uncertainties in table 5.1 are obtained statistically from the errors in the fit. The sinusoidal variation in right ascension is more difficult to measure due to its small magnitude, and in this case, the uncertainties are estimates only. Note that the phases of the right ascension and declination sine curves differ by 90° . This is expected since the sinusoidal error in right ascension should disappear at the highest and lowest points on the ring, while that for the declination should be maximal at these locations.

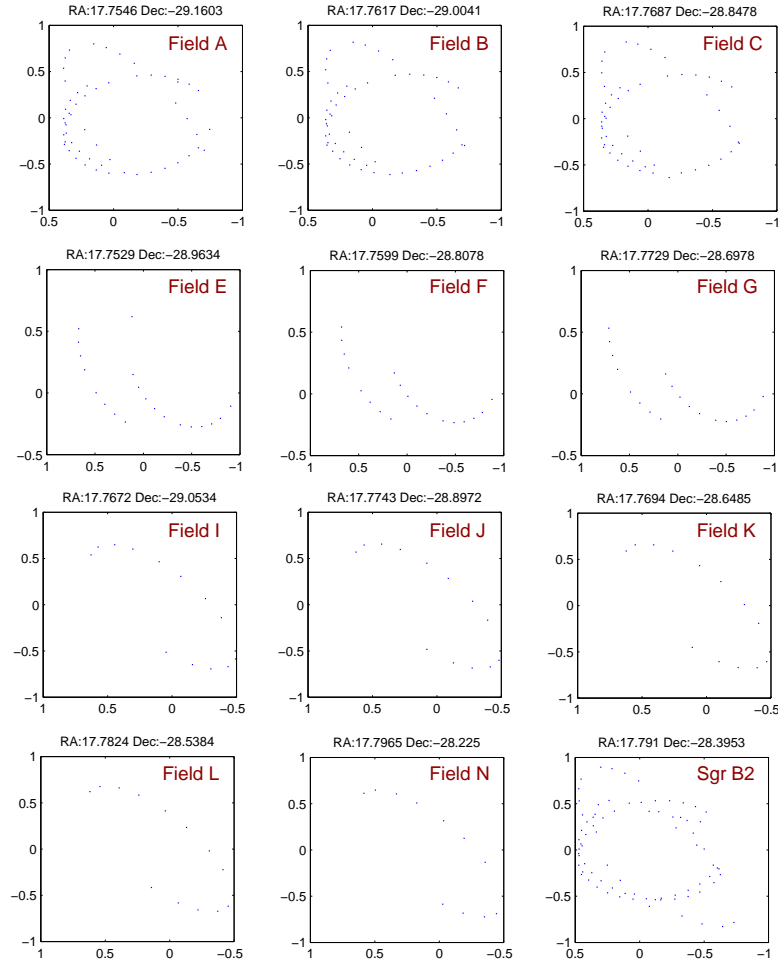


Figure 5.1. The pointing model of Viper was used to correct the reported telescope positions. Shown here are the pointing positions for each observed field that made the final cut. The average positions (0,0) are given above each pixel. The numbers on each axis are offsets from these positions in arcminutes. The pointing error of Viper during Austral Winter 2000 was ± 0.5 .

5.1.3. Pointing of SPARO

This pointing model has been applied to our data to determine pointing accuracy (see fig. 5.1). It can be seen from these plots that the pointing drifts tend to be

± 0.5 . Note that that some attempt to correct for azimuth ring tilt was made in declination during the observations.

Figure 5.2 is a plot of the coverage of the Galactic Center based on the above analysis.

The letters correspond to the names of each of the pointing position such that any pointing position can be referenced by a field letter plus a pixel number. “S” refers to the Sgr B2 pointing position.

5.2. NEFD

The NEFD, or Noise Equivalent Flux Density, can be intuitively understood as the amount of flux density from the source necessary to equal the the total effective flux density produced by the different sources of noise in the experiment. More precisely, if one observes a source with a flux density equal to the NEFD of the experiment for one second, the signal-to-noise ratio of the measurement will be unity. Thus, the NEFD provides a good indication of instrument performance.

We begin the discussion of SPARO’s NEFD by calculating the theoretical performance of the instrument based on measurements of the noise characteristics of the detectors and of the atmosphere. We then find the empirical NEFD as determined from polarization measurements of field A (central pixel coordinates: $\alpha_{2000} = 17^{\text{h}}45^{\text{m}}17^{\text{s}}$, $\delta_{2000} = -29^{\circ}9'37''$). Finally, we compare the empirical NEFD with the predicted NEFD.

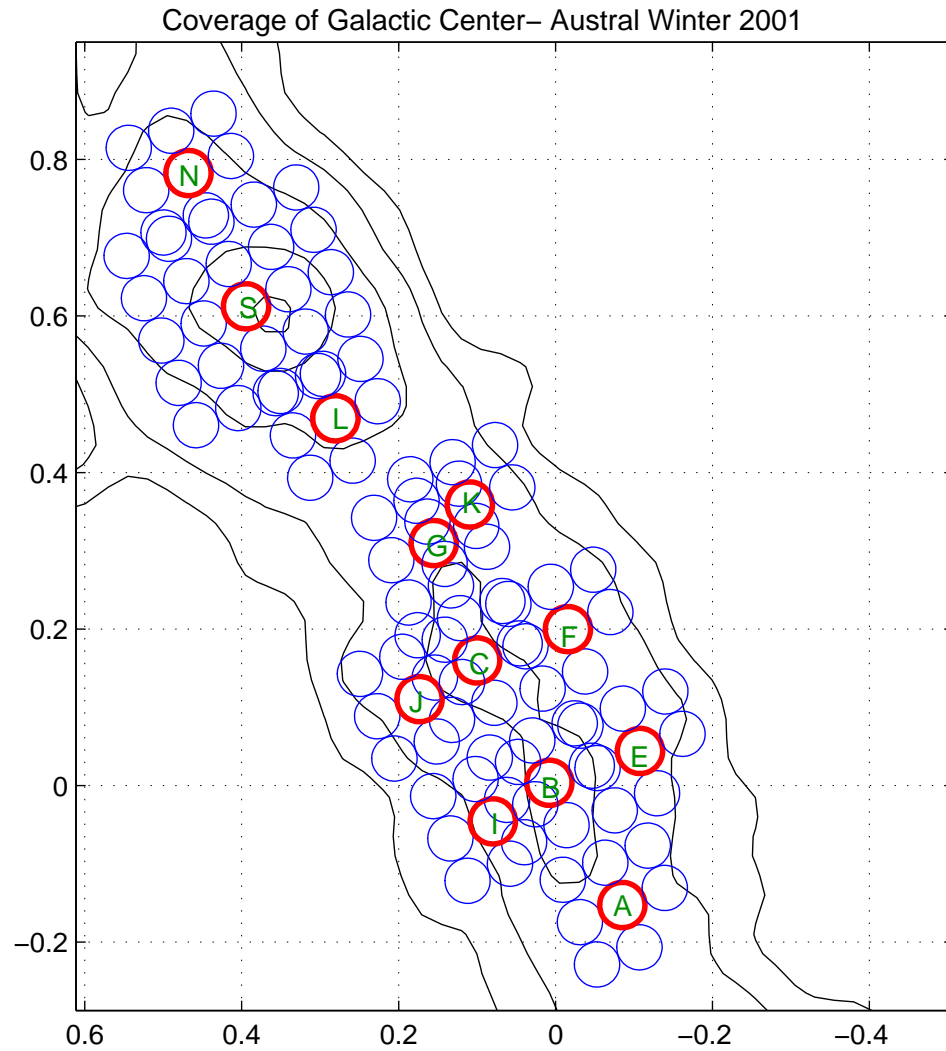


Figure 5.2. Pointing positions for each of SPARO's pixels in the Galactic center are overlaid over a contour map (also made by SPARO). Each bold circle represents the location of the central pixel in the SPARO array map. Each pixel is indexed according to the field designation followed by a pixel number (in the case of fields A through N) or a source number (in the case of S).

5.2.1. Theoretical NEFD

The NEFD of an instrument is related to the Noise Equivalent Power (NEP) of the system. The NEP gives a measure of the amount of power that the noise sources contribute to the detector signal. The sources of noise in a detector include those inherent to the electronics as well as those due to quantum fluctuations in the atmospheric emission. (Note that in ground-based submillimeter work, the atmospheric emission is always greater than that from the source, and thus quantum fluctuations in the source radiation are negligible.) The total of all detector noise has been measured for SPARO to be $\text{NEP}_{\text{detector}} = 1.2 \times 10^{-16} \text{ W Hz}^{-\frac{1}{2}}$ (Renbarger 2002). The contribution of photon noise to the NEP is given by Mather (1982) to be

$$(5.3) \quad \text{NEP}_{\text{photon}}^2 = 4 \frac{A\Omega}{c^2} \frac{(k_B T)^5}{h^3} \int_{x_1}^{x_2} \frac{x^4 dx}{e^x - 1} \left(1 + \frac{\epsilon Q_c}{e^x - 1} \right) \epsilon Q_c$$

where

k_B	Boltzmann's constant
c	Speed of light
h	Planck's constant
T	Temperature of the atmosphere
A	Area of Viper primary mirror
Ω	Solid angle of detector element
ν	Frequency
x	$h\nu/k_B T$
Q_c	Transition of cold (4K) elements
ϵ	Emissivity of the atmosphere

Quantity	Description	Value
T	Temperature of the atmosphere	200 K
A	Area of primary illuminated	$3.8 \times 10^{-3} \text{cm}^2$
Ω	Solid angle of a 6' beam	$2.4 \times 10^{-6} \text{sr}$
Q_c	Transmission of cold optics	1.9%
λ	Central wavelength of band pass filter	450 μm
$\Delta\lambda/\lambda$	Fractional band width of filter	0.1

Table 5.2. SPARO Characteristics from Renbarger (2002)

Using (5.3) it is possible to calculate $\text{NEP}_{\text{photon}}$. For this, we use values given in Renbarger (2002). These values are given in table 5.2. Note that at this wavelength and temperature, the Rayleigh-Jeans approximation applies, and $e^x - 1 \sim x$.

Because the atmosphere is generally opaque to 450 μm radiation, $\text{NEP}_{\text{photon}}$ depends only slightly on ϵ . Thus, we take $\epsilon \sim 1$. This leads to $\text{NEP}_{\text{photon}} = 1.8 \times 10^{-16} \text{ W Hz}^{-\frac{1}{2}}$. Adding this in quadrature with $\text{NEP}_{\text{detector}}$ gives $\text{NEP} = 2.2 \times 10^{-16} \text{ W Hz}^{-\frac{1}{2}}$.

To calculate the NEFD from the NEP, we use the following equation (Dowell et al. 1998).

$$(5.4) \quad \text{NEFD} = \frac{\sqrt{2} \text{NEP}}{\eta_{\text{chopper}} \eta_{\text{telescope}} A(\Delta\nu) Q} e^{\tau \sec z}$$

Here, $\eta_{\text{chopper}} = 0.8$ is the duty cycle of the chopper, $\eta_{\text{telescope}} = 0.35$ is the efficiency of the telescope, and $Q = 0.017$ is the total transmission of the dewar with respect to one array (Renbarger 2002). $\tau \sec z$ is the optical depth of the atmosphere at a zenith angle z . The factor of $\sqrt{2}$ is a quotient of a factor of 2 increase in NEFD due to the chopping process and a factor $\sqrt{2}$ decrease due to the use of two arrays

(Dowell et al. 1998). The theoretical estimate for SPARO's NEFD is

$$(5.5) \quad \text{NEFD} = 247 e^{\tau \sec z} \text{ Jy Hz}^{-\frac{1}{2}}.$$

5.2.2. NEFD Measurements

Equation 5.5 shows the functional dependence of the NEFD on τ and z . For the measurement of SPARO's NEFD, we assume the same form:

$$(5.6) \quad \text{NEFD} = C e^{\tau x \sec z}$$

Here, we have introduced the constant x as a calibration factor that converts the optical depth as measured by the $350 \mu\text{m}$ tipper at the South Pole (τ) to the actual optical depth of the atmosphere at $450 \mu\text{m}$. This value has been measured to be 0.75 such that for the Galactic center, $x \sec z = 1.5$. We use SPARO polarization data to estimate C and thus to determine the NEFD of SPARO as a function of airmass ($\sec z$) and τ . In order to make such a determination, we take advantage of the fact that the NEFD is related to the measured uncertainty in the polarization (Novak et al. 1989).

$$(5.7) \quad \sigma_p = \frac{100\sqrt{2} \text{NEFD}(x \sec z, \tau)}{\eta F \sqrt{t}}$$

In 5.7, η is the efficiency of the polarimeter, F is the flux into the SPARO beam and t is the integration time. The integration time can be calculated by knowing

the parameters of the data files. In the case of the field A files, the integration time is:

$$(5.8) \quad \frac{0.323 \text{ s}}{1 \text{ chop}} \times \frac{2 \text{ chops}}{1 \text{ frame}} \times \frac{24 \text{ frames}}{1 \text{ int}} \times \frac{4 \text{ ints}}{1 \text{ nodpair}} \times \frac{6 \text{ nodpairs}}{1 \text{ file}} = 373 \text{ s/file}$$

Putting together the equations for σ_p and NEFD, we can get the following relation.

$$(5.9) \quad \sigma_p = \left(\frac{100\sqrt{2}C}{\eta F \sqrt{t}} \right) e^{\tau x \sec z}$$

We take the natural log of this equation and get

$$(5.10) \quad \ln(\sigma_p) = \tau x \sec z + \ln \left(\frac{100\sqrt{2}C}{\eta F \sqrt{t}} \right).$$

This result is an expression that relates the observables σ_p , τ , and F to the constant C . t is constant for all of the field A observations and is given above, σ_p follows from the normal data analysis methods, and τ has been recorded for each of the observations.

A plot of the natural log of the polarization error versus τ for a given bolometer pair is expected to be a straight line with a slope of 1.5 and an intercept, ξ , that is related to C and F by

$$(5.11) \quad \xi = \ln \left(\frac{100\sqrt{2}C}{\eta F \sqrt{t}} \right)$$

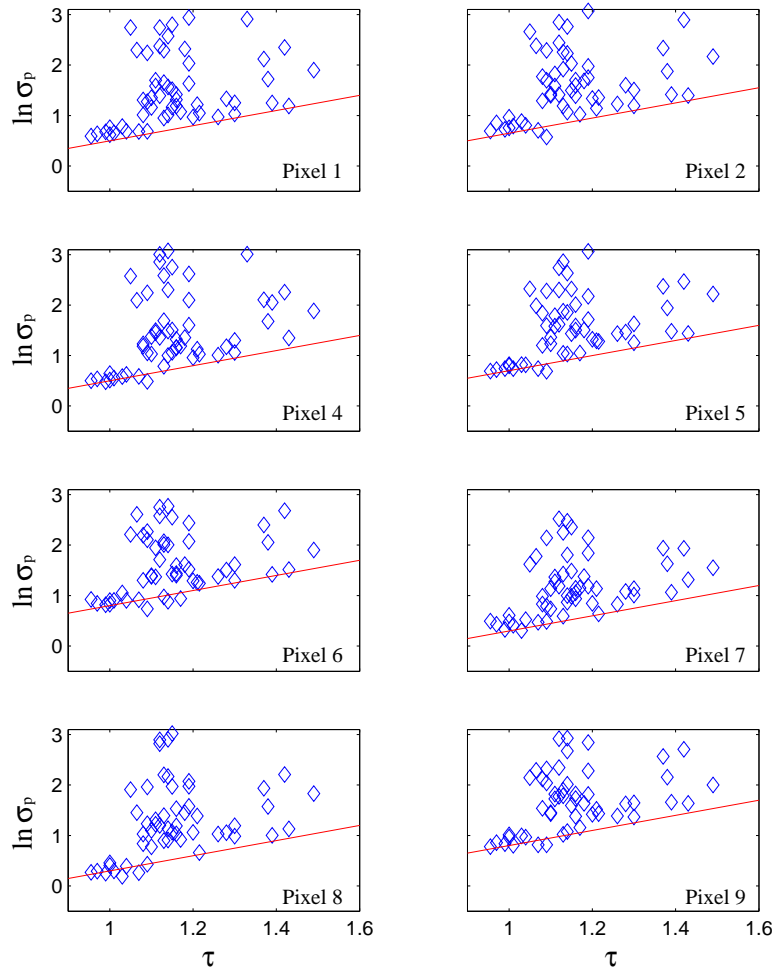


Figure 5.3. Polarization uncertainty is plotted against τ , the atmospheric opacity for each of SPARO’s 8 pixels. The slopes are set at 1.5 and the intercepts are chosen to correspond to the noise floor.

In practice, factors such as sky noise and noise due to microphonics prevent the system from being background or detector limited. In light of such systematics, this equation places a lower limit of noise on the system exhibited in figure 5.3 as a “noise floor” in the $\ln \sigma_p$ versus τ plot. In figure 5.3, each pixel is examined. The

Pixel	Intercept	$C/F(10^{-2}\text{S}^{\frac{1}{2}})$	$F/F_{\text{Sgr B2}}$	$C/F_{\text{Sgr B2}}(10^{-2}\text{S}^{\frac{1}{2}})$
1	-1.00	4.47	0.21	0.94
2	-0.85	5.19	0.20	1.04
4	-1.00	4.47	0.21	0.94
5	-0.80	5.46	0.21	1.15
6	-0.70	6.04	0.18	1.09
7	-1.20	3.66	0.28	1.03
8	-1.20	3.66	0.26	0.95
9	-0.70	6.04	0.18	1.09

Table 5.3. Results for Noise Floor Estimates

lines corresponding to the noise floor were determined by holding the slope constant at a value of 1.5 and then varying the intercept for each individual picture until the best value was estimated. The uncertainty in the intercept using this method is estimated to be ± 0.1 . The resulting intercept along with the value for C/F for each pixel is shown in table 5.3. Also shown in table 5.3 are the fluxes measured by each pixel relative to the flux measured for Sgr B2. From these data it is possible to compute $C/F_{\text{Sgr B2}}$ for each pixel.

5.2.3. Flux of Sgr B2

The final and most uncertain quantity we require for our estimate of the NEFD of SPARO is the $450 \mu\text{m}$ flux of Sgr B2 into a $6'$ beam. When the data for the SCUBA $450 \mu\text{m}$ Galactic center survey (Pierce-Price et al. 2000) becomes available, it will be possible to make a direct measurement of the $450 \mu\text{m}$ flux from Sgr B2 which will improve the accuracy of SPARO's NEFD estimate. For now, however, we use the SHARC $350 \mu\text{m}$ map of the Galactic Center (Dowell et al. 1998) and the 800

μm map of Lis & Carlstrom (1994). From these maps, we infer that the flux values for 6' beam are 145,660 Jy and 3,935 Jy for 350 and 800 μm , respectively.

In order to estimate the flux from Sgr B2 at 450 μm , we employ a spectral model for the emission to which we fit the above two data points. We begin with the Planck function:

$$(5.12) \quad B_\nu(T) = \frac{2h\nu^3}{c^2}(e^{h\nu/kT} - 1)^{-1}.$$

The ratio of fluxes at two different frequencies is typically given by the ratio of Planck functions each modified by an emissivity law that goes as ν^n (see chapter 3).

$$(5.13) \quad \frac{B_1(T)}{B_2(T)} = \left(\frac{\nu_1}{\nu_2}\right)^3 \left(\frac{\nu_1}{\nu_2}\right)^n \frac{e^{h\nu_2/kT} - 1}{e^{h\nu_1/kT} - 1}$$

For various values of n , we solve this equation numerically for T , the average temperature of the 6' region around Sgr B2. We find that the temperature curve given by the two data points is steeper than typical optically thin molecular clouds. In fact, this equation cannot be solved for $n < 2.4$. Table 5.4 gives temperatures and inferred flux values for Sgr B2's 450 μm flux for various values of n .

It must be noted here that (5.13) is only an approximation and does not apply particularly well to Sgr B2, a region that is quite complex. Typically, values of n range from 1.5 to 2 in molecular clouds. The high values of n we find for Sgr B2 are consistent with the abnormally high values for the spectral index found by

n	T(K)	$F_{450\mu\text{m}}$ (Jy beam ⁻¹)
2.4	446	48,708
2.5	111	49,096
2.6	65	49,508
2.7	47	49,940
2.8	37	50,388
2.9	31	50,851
3.0	26	51,327

Table 5.4. Derived Values for 450 μm Fluxes as a Function of n

Pierce-Price et al. (2000). Nonetheless, we will cautiously use this model in light of the lack of a direct measurement of the 450 μm flux.

Spectra of the far-infrared and submillimeter emission from various peaks of Sgr B2 (Goldsmith et al. 1992) peak around $\sim 100 \mu\text{m}$ corresponding to a color temperature of ~ 30 K. This low temperature eliminates the lower values of n in table 5.4 and gives a value of $\sim 51,000$ Jy for the Sgr B2 flux into a SPARO beam.

5.2.4. Results

Using this estimate of the flux of Sgr B2, we measure $C = 510$, a value twice that of our prediction. It is highly likely that the telescope efficiency is overestimated, since its calculation was based on reflective losses without taking into account optical effects. To completely understand the throughput of the telescope it will be necessary to measure the fraction of light from a point source that is detected by the designated pixel in the focal plane.

CHAPTER 6

SPARO Data Analysis

This chapter discusses the polarimetry data analysis procedures used for data collected with SPARO during Austral Winter 2000. Previous generations of polarimeters have taken advantage of the relative sky rotation that occurs in the focal plane of an alt-az telescope. There is no sky rotation at the South Pole due to the co-alignment of the equatorial and horizon coordinate systems. Thus, SPARO data analysis requires some changes from that of previous submillimeter and far-infrared polarimeters.

6.1. Determination of χ Angle and Polarization Efficiency

6.1.1. Determination of χ

The χ angle can be thought of as the zero angle for the half wave plate. The convention that exists in polarimetry is that the polarization angle is measured from celestial north and increases counterclockwise (toward the east). However, the Stokes parameters that are measured by a half wave plate with an unknown orientation have a zero angle that is generally not aligned with celestial north. Because of this, a calibration angle, χ , is necessary to bring the coordinate system of the half-wave plate into alignment with that of convention. (See fig. 6.1 for a

ϕ	P	$\phi - \chi$
45°	88.88 ± 1.11	66.3° ± 0.4
90°	88.75 ± 1.70	108.0° ± 0.6

Table 6.1. Grid Test Results

diagram of the coordinate system.) To account for this, our definition of ϕ , the polarization angle, includes an offset χ :

$$(6.1) \quad \phi = \frac{1}{2} \text{atan} \left(\frac{q}{u} \right) + \chi.$$

In general, the expression for ϕ is more complicated, involving instrument and sky rotation angles, but at the South Pole there is no sky rotation (i.e. the parallactic angle, α is always zero).

The procedure for measuring χ involves placing a polarizing test grid in front of the pressure window at two angles corresponding to polarization angles of 90° and 45°. Polarization measurements under these conditions give $\phi - \chi$. The results of these grid tests are shown in table 6.1.

The background source in these measurements was NGC 6334. We can ignore polarization from the instrument and the source, as they contribute only about 1% (Renbarger 2002).

From these measurements, we discern $\chi = -21.3$. In reporting χ , we use the value from the 45° orientation, since it is a much more accurate angular placement

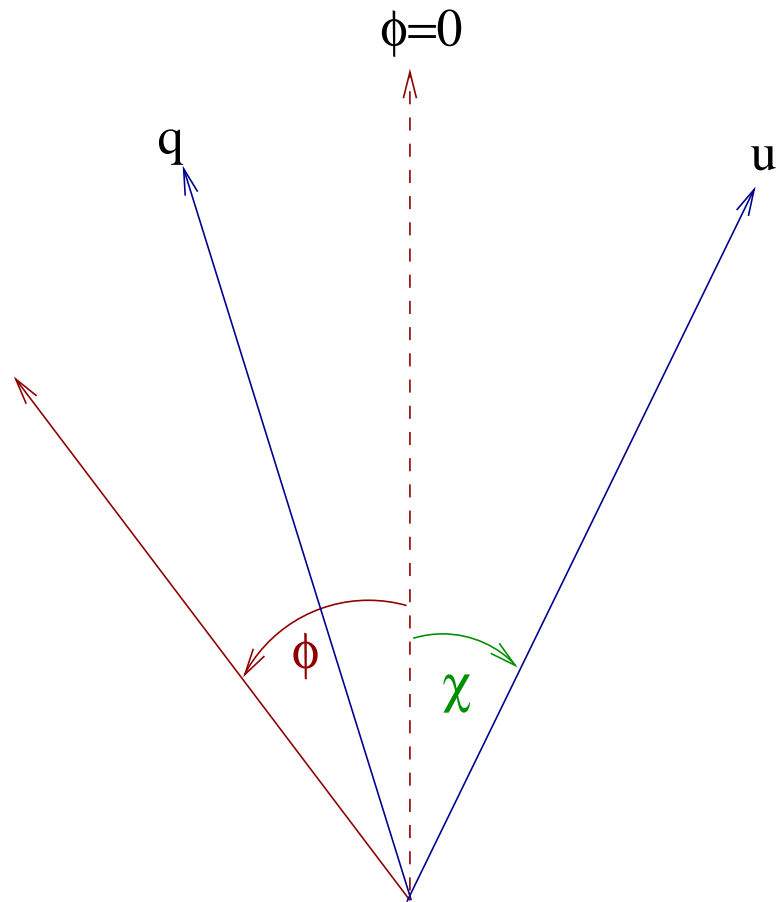


Figure 6.1. The coordinate axes q and u are determined by the relative orientation of the half-wave plate with respect to celestial north. χ is the angle from which the u axis differs from north. Both ϕ and χ are measured from north to east, such that in this diagram, χ has a negative value.

of the grid than the second positioning. The second positioning is necessary to verify that the half wave plate is moving in the direction that conforms to the coordinate system in figure 6.1. Moving the half-wave plate in the opposite direction changes the relative orientation of u and q along with the value of χ .

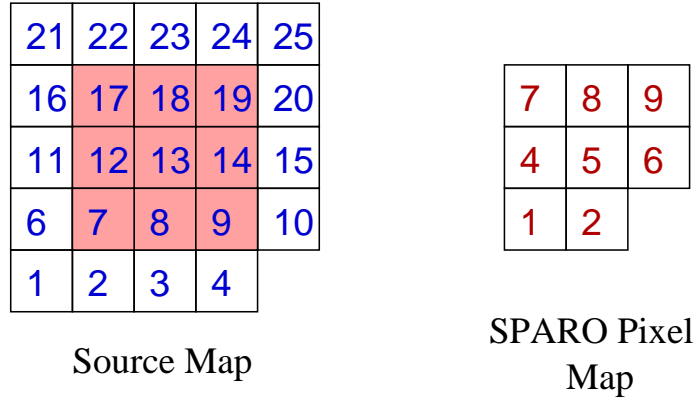


Figure 6.2. Shown are the geometries and numbering schemes used for source and SPARO pixel maps in the measurement of instrumental polarizations for the cases of Sgr B2 and the Moon. The shaded sources are those covered by pixel 5 during the observations.

6.1.2. Polarization Efficiency

Because of imperfections in the analyzer grid, the polarization that SPARO measures is less than the true polarization of the source. Thus, the data must be corrected by the reciprocal of the polarization efficiency. Part of the calibration of a polarimeter is to determine this quantity. Fortunately, the grid test also provides a test of polarization efficiency by supplying a source of highly polarized light.

If we assume that the light entering the dewar is 100% polarized, the measured polarization then gives the polarization efficiency. The results for each of the eight operating pixels are shown in table 6.2.

Pixel	$\phi = 90^\circ$	$\phi = 45^\circ$
1	64.32 ± 10.48	76.02 ± 5.71
2	80.21 ± 3.93	83.06 ± 1.96
4	75.99 ± 5.57	81.18 ± 2.86
5	89.75 ± 1.70	88.88 ± 1.11
6	88.74 ± 1.96	87.25 ± 1.81
7	71.41 ± 5.41	80.98 ± 5.59
8	88.74 ± 1.96	87.69 ± 1.89
9	92.58 ± 1.98	86.59 ± 2.24

Table 6.2. Polarization Efficiencies

The measured polarization peaks in the central pixel where the flux is at a maximum. Some fluxes in the outer (low polarization) pixel are as low as 20% of the flux in the central pixel. Given the uniformity of the analyzer grid, it is unlikely that the polarization efficiency of the outer pixels is less than that of the central pixel. In addition, one does not observe systematically low polarizations in these pixels over the extent of our data. Rather, the lower polarization measurements in table 6.2 are most likely due to contamination from the test grid frame.

We take the polarization efficiency to be 89%, the average of the polarization efficiencies for the pixel with the peak flux. Thus, for all of our polarization measurements, we need to multiply the polarization and its corresponding errors by 1.12 to obtain the true polarization of the source. Note that this preserves the signal-to-noise ratio, and thus the angle that is measured and its corresponding errors are unaffected by this correction.

6.2. Instrumental Polarization

It is expected that the instrument and telescope will induce small polarizations in the incoming radiation. There are two reasons why understanding this effect is desirable. First, it is necessary to verify that the polarization signals measured are not dominated by this instrumental contribution. Second, by understanding this effect, it is possible to subtract the instrumental polarization from the final results. In this way, the threshold of measurable polarizations is lowered, thus increasing the sensitivity of the instrument.

The observing method involves measuring source polarizations with different pixels and then making use of these various cross-correlations between pixels and sources by employing an algorithm that fits the data with an observing model. The instrumental and source polarizations are extracted from this fit.

6.2.1. Observations

Observations for the instrumental polarization study were made using both the Moon and Sgr B2 as sources. The observational procedure for each of these sources is as follows. First, a central pointing position is chosen. For the Moon, this is an arbitrary point near the center. For Sgr B2, it is the submillimeter peak. Each pixel (including pixel 3 which is broken) is then centered on this location and

polarimetry data are taken. Figure 6.2 shows a footprint of the array next to a footprint of the source positions. As the array footprint is moved such that each pixel is centered on central source (or such that pixel 5 covers each of the shaded sky positions), the array covers the 24 positions shown in the source map on the left side of figure 6.2.

6.2.2. IP of Pixel 5

This observing procedure has one limitation. Because the observing scheme has translations of the array with respect to the sources but no rotation, the fitting algorithm will have degenerate solutions for the instrumental and source polarizations that differ from one another by a constant polarization. In order to break this degeneracy, at least one of the parameters must be specified a priori.

The polarization of Sgr B2 is known but is not useful for the set of observations done on the Moon. For the sake of uniformity in the two sets of observations, we use the source polarization of Sgr B2 to measure the instrumental polarization of pixel 5. This is possible because the majority of our data on Sgr B2 was taken with pixel 5 centered on the peak.

Hertz data taken in the region centered on Sgr B2 and averaged into a $6'$ beam give $P = 0.49\%$, $\phi = 82^\circ$. Because these results are a weighted average of many measurements, each with a signal-to-noise ratio greater than three, the statistical

error is small enough to be negligible. In addition, the uncertainty in SPARO's beam size is also negligible since the majority of the polarized flux is concentrated near the peak of Sgr B2, and so polarized flux in the outer part of the beam contributes little to the sum. The variation of the polarization spectrum of Sgr B2 is assumed to be negligible in going from $350 \mu\text{m}$ to $450 \mu\text{m}$.

Based on the coordinate system in figure 6.1, q and u are found from the following definitions.

$$(6.2) \quad \tan[2(\phi - \chi)] = \frac{q}{u}, \quad P^2 = u^2 + q^2$$

Recall from earlier in this chapter that χ , the zero angle of the half-wave plate has been measured to be $-21^\circ.3$. Sgr B2 then has $q = -0.00222$ and $u = -0.00437$.

These numbers represent the polarization measured by a $6'$ beam of a perfect polarimeter. Since the polarization efficiency of SPARO is 89%, these must be multiplied by 0.89 in order to get the value of polarization SPARO would measure for Sgr B2. This leads to $q = -0.00198$, $u = -0.00389$.

Since we know the source polarization, we can subtract it from our signal to find the instrumental polarization of pixel 5 to be $P = 0.40\%$, $\phi = 27.2^\circ$. This corresponds to $q = 0.0040 \pm 0.0005$, $u = -0.0005 \pm 0.0005$.

Index(j)	Parameter	Index(j)	Parameter	Index(j)	Parameter
1	Pixel 1	12	Source 6	23	Source 17
2	Pixel 2	13	Source 7	24	Source 18
3	Pixel 4	14	Source 8	25	Source 19
4	Pixel 6	15	Source 9	26	Source 20
5	Pixel 7	16	Source 10	27	Source 21
6	Pixel 8	17	Source 11	28	Source 22
7	Pixel 9	18	Source 12	29	Source 23
8	Source 1	19	Source 13	30	Source 24
9	Source 2	20	Source 14	31	Source 25
10	Source 3	21	Source 15		
11	Source 4	22	Source 16		

Table 6.3. Parameter List for Observing Model

6.2.3. Fitting the Observing Model

The observing model based on the method in § 6.2.1 is illustrated in figure 6.2. For either source (the Moon or Sgr B2), we label the grid of 24 sky positions mapped out by SPARO observing scheme. We also label the elements of SPARO’s array map.

Next, we define a parameter vector p_j that contains the 31 unknowns. The mappings from the physical quantities shown in figure 6.2 to the index of this vector are given in table 6.3.

Position 13 in the sky map corresponds to center of the Moon or the peak of Sgr B2, depending on the source in question. The observing method described in § 6.2.1 yields 8 relations between pixels and sources for each of 9 pointings.

The result is 72 different equations which relate a measured Stokes' parameter (d_n) to the Stokes' parameter of a source ($p_s(n)$) and the Stokes' parameter of the instrumental polarization of the pixel used to make the measurement ($p_i(n)$). The relation is

$$(6.3) \quad d_n = p_{s(n)} + p_{i(n)}.$$

The index n refers to the observation number. s and i are integer functions of n that index the appropriate source and instrument parameter for a given observation. These functions are given in table 6.4. The observations involving pixel 5 have no index associated with them since this parameter is held fixed. In the equations involving pixel 5, $p_{i(n)}$ is replaced by a constant. Note that (6.3) states that a measured Stokes' parameter is simply the sum of the contributions to that parameter from the source and the instrument, respectively. This additive property of Stokes' parameters is a consequence of low polarizations.

The next step is to calculate a merit function χ^2 .

$$(6.4) \quad \chi^2 = \sum_{n=1}^{72} \frac{(d_n - p_{s(n)} - p_{i(n)})^2}{\sigma_{d_n}^2}$$

Here the errors in the d_n is used. These errors (σ_{d_n}) are determined statistically in the data analysis procedures.

n	$s(n)$	$i(n)$	n	$s(n)$	$i(n)$	n	$s(n)$	$i(n)$
1	8	1	25	12	1	49	17	1
2	9	2	26	13	2	50	18	2
3	12	3	27	17	3	51	22	3
4	13	-	28	18	-	52	23	-
5	14	4	29	19	4	53	24	4
6	17	5	30	22	5	54	27	5
7	18	6	31	23	6	55	28	6
8	19	7	32	24	7	56	29	7
9	9	1	33	13	1	57	18	1
10	10	2	34	14	2	58	19	2
11	13	3	35	18	3	59	23	3
12	14	-	36	19	-	60	24	-
13	15	4	37	20	4	61	25	4
14	18	5	38	23	5	62	28	5
15	19	6	39	24	6	63	29	6
16	20	7	40	25	7	64	30	7
17	10	1	41	14	1	65	19	1
18	11	2	42	15	2	66	20	2
19	14	3	43	19	3	67	24	3
20	15	-	44	20	-	68	25	-
21	16	4	45	21	4	69	26	4
22	19	5	46	24	5	70	29	5
23	20	6	47	25	6	71	30	6
24	21	7	48	26	7	72	31	7

Table 6.4. Observing Model

The idea now is to determine the set of parameters which minimizes this merit function. This involves a set of 31 equations in which the derivative of the merit function with respect to each parameter is zero.

$$(6.5) \quad \frac{\partial \chi^2}{\partial p_j} = 2 \sum_n \left(\frac{p_{s(n)} + p_{i(n)} - d_n}{\sigma_{d_n}^2} (\delta_{sj} + \delta_{ij}) \right) = 0$$

This set of equations gives rise to a matrix equation which can be solved by matrix inversion. The method of matrix inversion used is Gauss-Jordan (Press et al. 1992).

This matrix is symmetric. This can be shown by observing that the n th element in a row can be found by taking the partial derivative of 6.5 with respect to the n th parameter. Thus, the matrix elements are given by

$$(6.6) \quad A_{ij} = \frac{\partial}{\partial p_j} \left(\frac{\partial \chi^2}{\partial p_i} \right) = \frac{\partial}{\partial p_i} \left(\frac{\partial \chi^2}{\partial p_j} \right) = A_{ji}$$

The errors can be calculated using the standard error propagation equation.

$$(6.7) \quad \sigma_{p_n}^2 = \sum_m \sigma_{d_n}^2 \left(\frac{\partial p_m}{\partial d_n} \right)^2$$

We have to calculate the partials on the right hand side. The equation we are trying to solve in order to find the parameters can be expressed as

$$(6.8) \quad p_i = \sum_j A_{ij}^{-1} D_j$$

Here, D_j is a vector containing linear combinations of data and errors defined by the observing model. Since the matrix elements do not have any dependence on

Pixel	P	ϕ	q	u
1	$0.38 \pm .12$	38.6 ± 9.7	$.0033 \pm .0012$	-0.0019 ± 0.0013
2	0.63 ± 0.12	46.5 ± 5.6	$.0044 \pm .0011$	-0.0045 ± 0.0013
4	0.53 ± 0.10	30.4 ± 6.1	$.0052 \pm .0010$	-0.0013 ± 0.0011
5	0.40 ± 0.05	27.2 ± 3.5	$.0040 \pm .0005$	$-.0005 \pm 0.0005$
6	0.25 ± 0.14	77.3 ± 14.7	$-0.0007 \pm .0012$	$-.0023 \pm 0.0015$
7	0.53 ± 0.12	9.0 ± 7.1	$0.0046 \pm .0012$	0.0026 ± 0.0014
8	0.56 ± 0.12	153.6 ± 5.7	$-0.0009 \pm .0010$	0.0052 ± 0.0012
9	0.79 ± 0.13	104.2 ± 5.5	$-.0075 \pm .0013$	$-.0026 \pm 0.0015$

Table 6.5. IP Fit Results for Sgr B2 Observations

the parameters,

$$(6.9) \quad \frac{\partial p_i}{\partial d_m} = \sum_j A_{ij}^{-1} \left(\frac{\partial D_j}{\partial d_m} \right)$$

The partial derivatives on the right hand side of this equation can be calculated directly, and hence a vector of errors can be calculated.

The fitting routine was applied to both the Moon data and to the Sgr B2 data. Tables 6.5 and 6.6 show the instrumental polarization matrices derived for the case of Sgr B2 and the Moon, respectively. The errors for both sets of data have been inflated so that the fit gives a χ^2 of 1. Initially the χ^2 values for each observation were as follows. For the Moon, $\chi_q^2 = 5.49$ and $\chi_u^2 = 6.77$. For Sgr B2, $\chi_q^2 = 1.53$ and $\chi_u^2 = 2.04$.

The resulting source polarizations for the two sources are shown in figure 6.3 and figure 6.4.

Pixel	P	ϕ	q	u
1	$0.49 \pm .04$	56.0 ± 1.9	$.0021 \pm .0003$	-0.0044 ± 0.0004
2	0.47 ± 0.04	57.2 ± 2.0	$.0018 \pm .0003$	-0.0043 ± 0.0004
4	0.62 ± 0.02	39.3 ± 1.2	$.0053 \pm .0002$	-0.0032 ± 0.0003
5	0.40 ± 0.05	27.2 ± 3.5	$.0040 \pm .0005$	$-.0005 \pm 0.0005$
6	0.27 ± 0.04	68.3 ± 3.4	$.00003 \pm .0003$	$-.0027 \pm 0.0004$
7	0.49 ± 0.02	14.7 ± 1.5	$0.0047 \pm .0002$	0.0015 ± 0.0003
8	0.15 ± 0.03	143.7 ± 4.5	$-0.0007 \pm .0003$	0.0013 ± 0.0003
9	0.41 ± 0.03	91.6 ± 2.2	$-.0029 \pm .0003$	$-.0028 \pm 0.0003$

Table 6.6. IP Fit Result for Moon Observations

Note that these maps are both in array coordinates. The direction of north is shown in the legend.

Note the pattern of polarization the fit gives for the Moon in figure 6.4. The pattern is generally radial with minimal polarization near the center and increasing to close to 1% near the edges. The approximate size of the Moon is shown as a circle. Our results are qualitatively similar to Barvainis et al. (1988) who find a radial pattern at the edge of the Moon with a polarization magnitude of about 1% at 1.3 mm.

6.2.4. Final IP and Systematics

The best estimate for a final IP matrix is determined from a weighted average of the two cases. Once again, the errors have been inflated to obtain a χ^2 of unity.

The final results are given in table 6.7 and illustrated in figure 6.5.

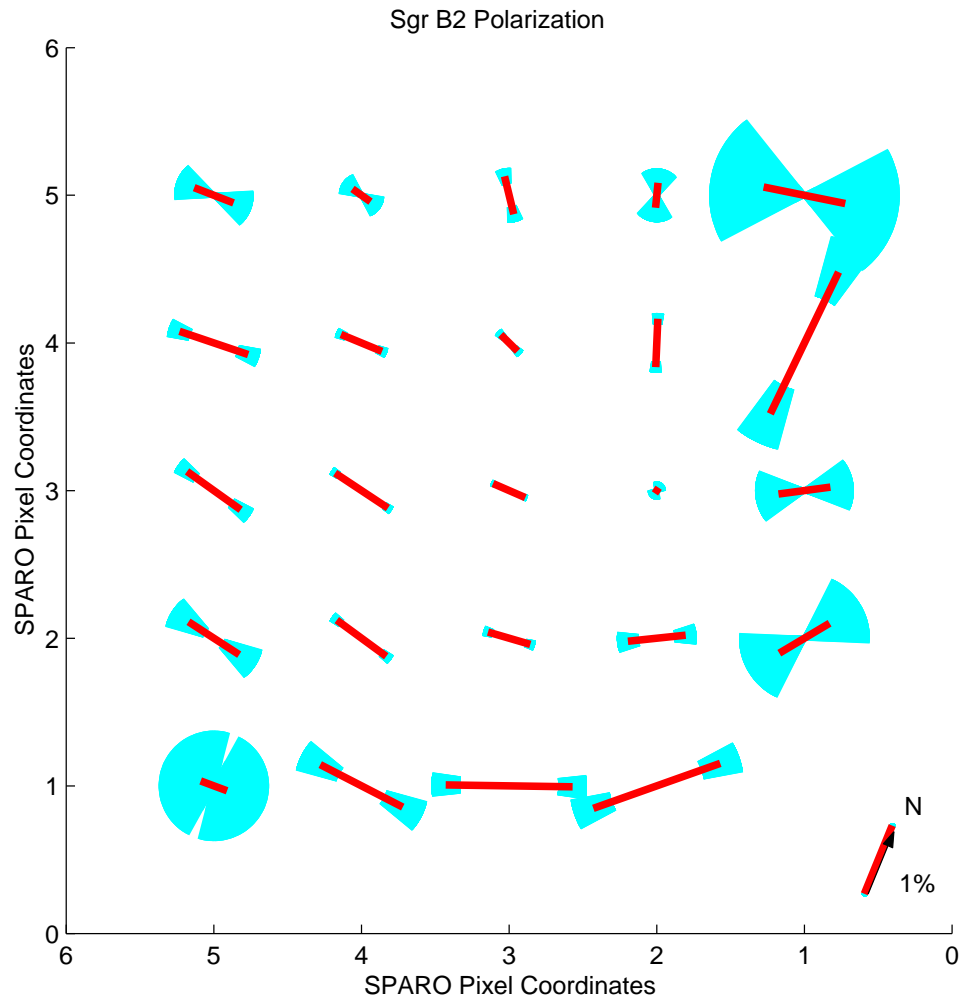


Figure 6.3. The measured source polarizations for the 24 positions of Sgr B2 are shown. The shaded “bow ties” represent the uncertainties in each of the polarizations.

It is of course possible that we are not limited by statistical errors and that systematic errors are responsible for the lack of agreement between the two independent measurements of instrumental polarization. This is different than the

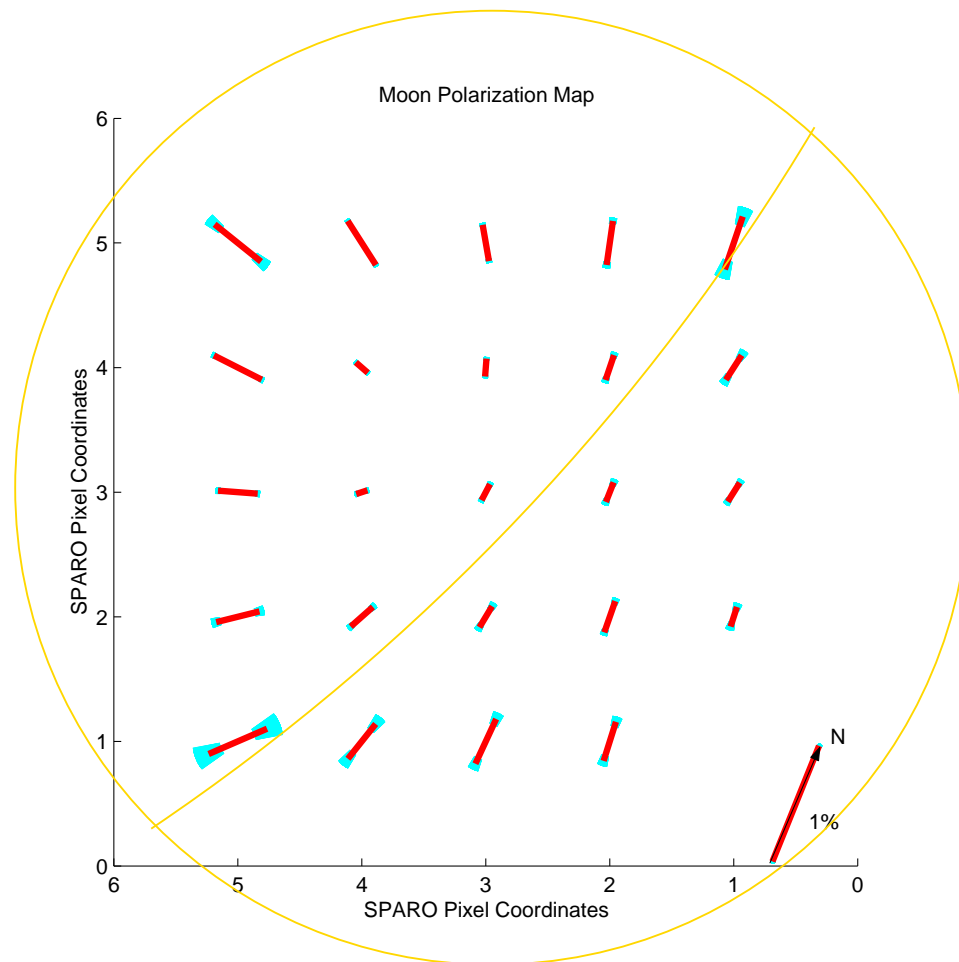


Figure 6.4. The measured source polarizations for the 24 positions of the Moon are shown. The shaded “bow ties” represent the uncertainties in each of the polarizations. The size of the Moon is indicated by the circle and the bisecting curve gives a rough depiction of the phase of the Moon during the observations.

case that we have assumed above in which the lack of agreement is due to limited sampling of a statistical ensemble and can be compensated for by a simple error inflation. In the case of systematic errors, we would like to get an estimate of

Pixel	P	ϕ	q	u
1	$0.47 \pm .05$	55.1 ± 2.9	$.0021 \pm .0005$	-0.0042 ± 0.0005
2	0.47 ± 0.05	56.2 ± 2.9	$.0020 \pm .0005$	-0.0043 ± 0.0005
4	0.61 ± 0.04	36.5 ± 1.8	$.0053 \pm .0004$	-0.0031 ± 0.0004
5	0.40 ± 0.05	27.2 ± 3.5	$.0040 \pm .0005$	$-.0005 \pm 0.0005$
6	0.26 ± 0.05	68.8 ± 5.1	$-.00002 \pm .0005$	$-.0027 \pm 0.0005$
7	0.49 ± 0.03	14.5 ± 2.2	$0.0047 \pm .0003$	0.0015 ± 0.0004
8	0.16 ± 0.04	145.1 ± 6.2	$-0.0007 \pm .0003$	0.0015 ± 0.0004
9	0.42 ± 0.04	92.7 ± 3.3	$-.0032 \pm .0004$	$-.0028 \pm 0.0005$

Table 6.7. Final IP Matrix

a threshold below which we do not believe our results. Of course, instrumental polarization is not the only possible systematic, so we attempt here to consider its contribution to the systematics of the experiment. To do so, for each pixel, we consider the difference between the two measurements.

$$(q_i(\text{Sgr B2}) - q_i(\text{Moon}))$$

We do the same for u . In doing so, it is useful to plot the differences which are shown in figure 6.6.

We can see from this plot that there seems to be no general offset from one measurement to the next which would indicate a systematic change in the instrument from one test to the other. In order to estimate the effects of systematics, we can take the standard deviation of differences in the q and u parameters. This leads to $\sigma_q = 0.0023$ and $\sigma_u = 0.0015$. Adding these in quadrature gives the estimate of

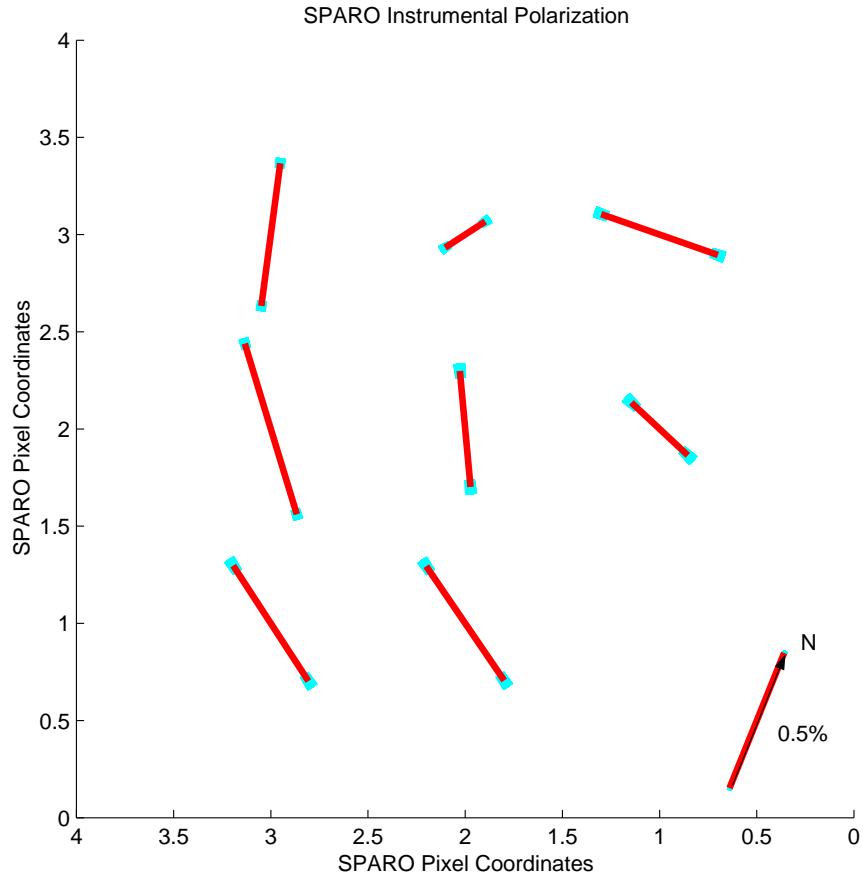


Figure 6.5. The final instrumental polarization matrix was determined from an error-weighted average of the matrices derived from the Sgr B2 and Moon fit results. Uncertainties are again illustrated by “bow ties.”

systematic error to be 0.27%. To be safe, we will set the lower limit of polarization measurements that we believe at 0.5%.

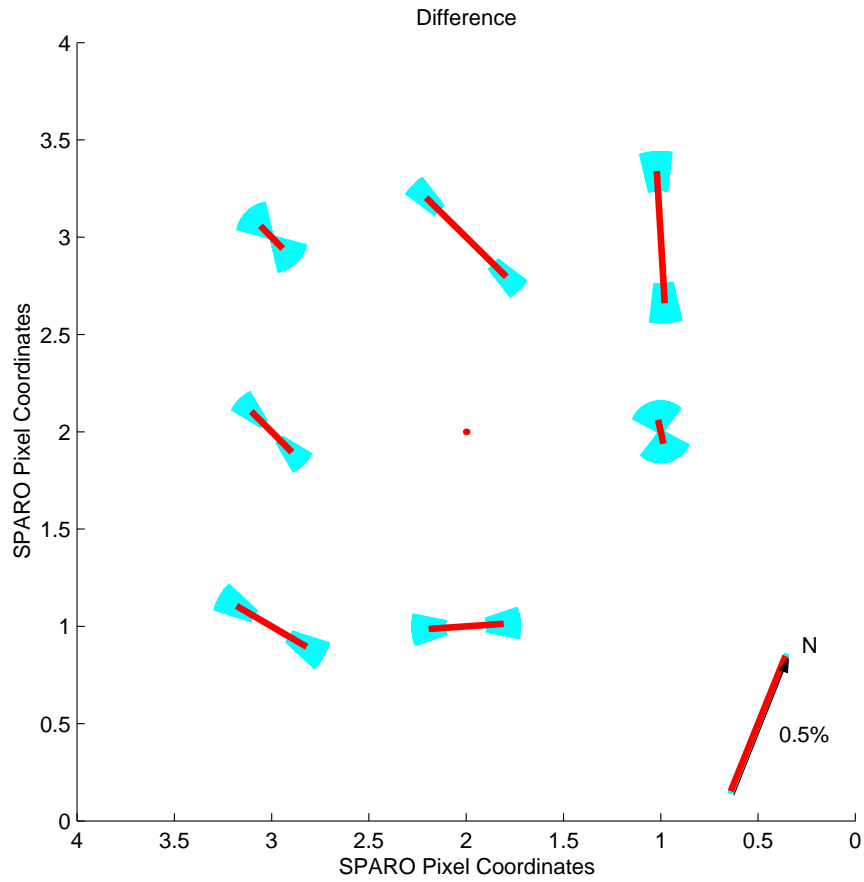


Figure 6.6. In order to gauge the consistency of our results, it is helpful to plot the vector difference between the results from the Moon and Sgr B2.

6.3. Snow on the Tertiary

We have discovered that a polarization measurement is highly affected by the amount of snow present on the tertiary mirror of Viper. Specifically, the snow has the effect of producing polarizations in the N-S direction in excess of 4%.

A small camera installed on Viper takes pictures of the tertiary periodically during the data taking process. Typically, photos are taken after every 12 polarimetry files. In an attempt to quantify the amount of snow on the mirror, we have assigned an integer value of 0 through 4 based on the amount of snow visible on the tertiary. Here a value of 0 applies to a completely snow-free tertiary while 4 corresponds to one that is completely covered. Figure 6.7 gives examples of the 5 levels of snow.

To examine the effect of snow on the data, we once again use the submillimeter peak of Sgr B2 as a calibration source. For this target, there are 79 files taken with a zero snow rating and 67, 6, 14, and 13 files associated with snow levels of 1 through 4, respectively. Figure 6.8 quantifies polarization parameters as a function of snow level.

Notice that the effect of the snow is to induce a high ($\sim 4\%$) polarization at an angle of 0° (or 180°). This is the north-south direction on the sky and the vertical direction on the primary. It appears that level 0 and 1 are unaffected by this phenomenon. Considering the magnitude of the effect is so large at snow level 2, there are only two usable levels (0 and 1); however, we wish to check for an insidious smaller contribution at snow level 1.

To study this we analyze our 88 pointings two different ways. First, we include only snow level 0 data. Then we repeat the analysis, but this time, we include both

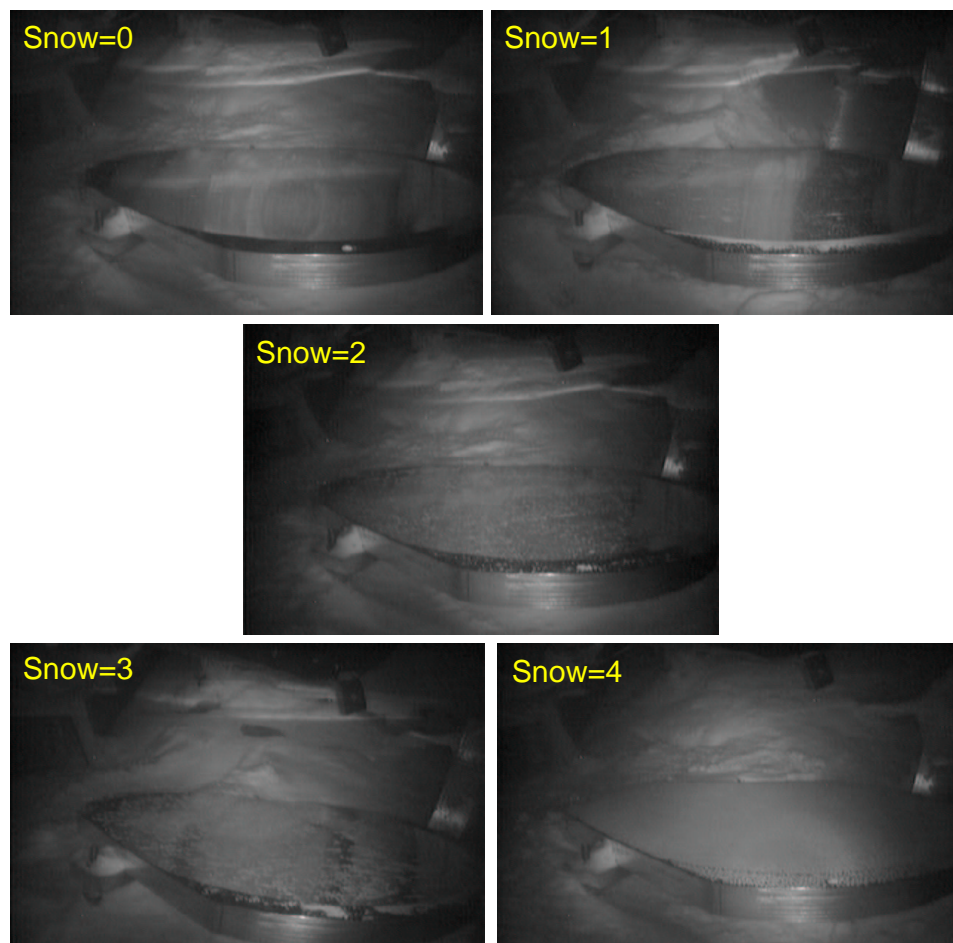


Figure 6.7. Here are examples of each of the 5 snow coverage conditions of the tertiary mirror on Viper. They were taken after every 12 data files by a small camera mounted to the telescope and operated remotely.

snow level 0 and 1 data. We compare these two cases by plotting the difference between the Stokes' parameters in each of the 88 pointings. The results are shown in figure 6.9.

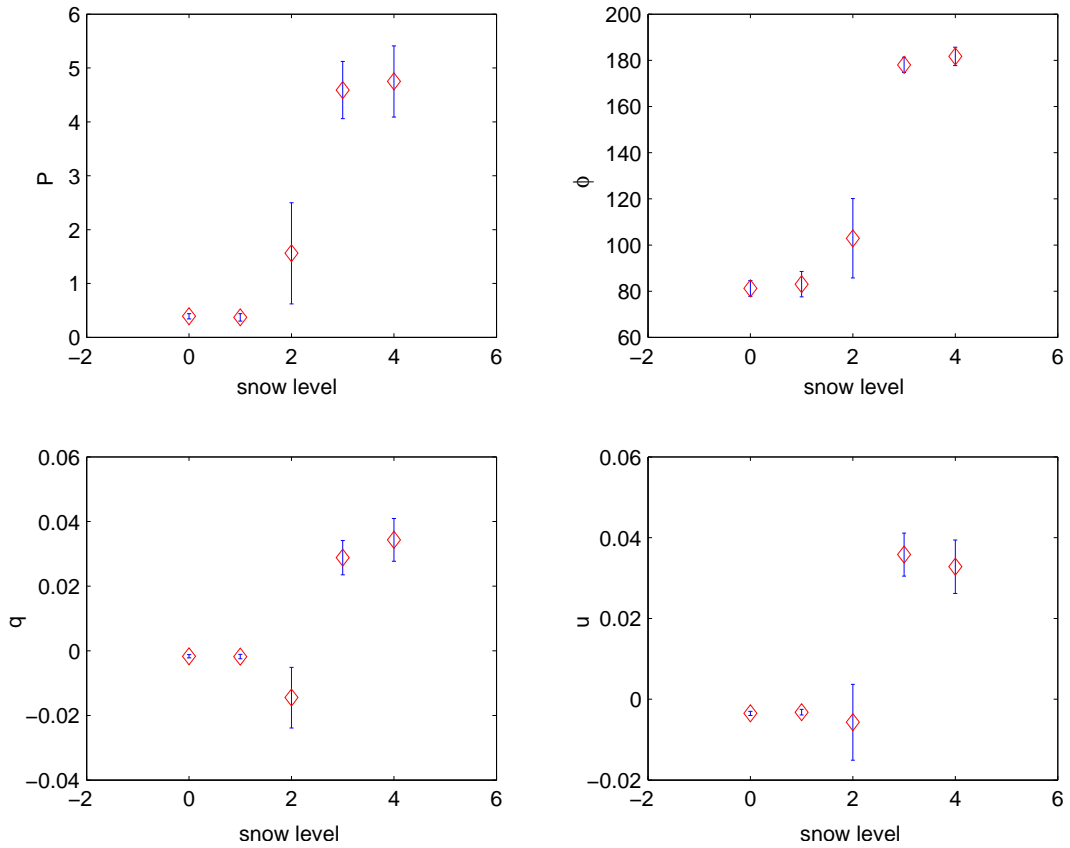


Figure 6.8. Plots of the effect of the snow on the measurement of polarization of Sgr B2 are shown. The data are binned by the degree of snow coverage and the effect on q , u , P , and ϕ is observed. Note that for snow coverages of 0 and 1 there seems to be little effect, but by a snow coverage of 3, the polarization increases and the angle of the polarization begins to point toward N-S (180°).

The mean difference in q is $9.2 \times 10^{-5} \pm 2.8 \times 10^{-4}$ and that in u is $4.9 \times 10^{-4} \pm 2.6 \times 10^{-4}$. Thus there is no effect in q that is discernible here and any systematic effect in u is below 0.1%. Thus, we can be reasonable sure that these snow level 1 data are not appreciably contaminated by snow on the tertiary mirror.

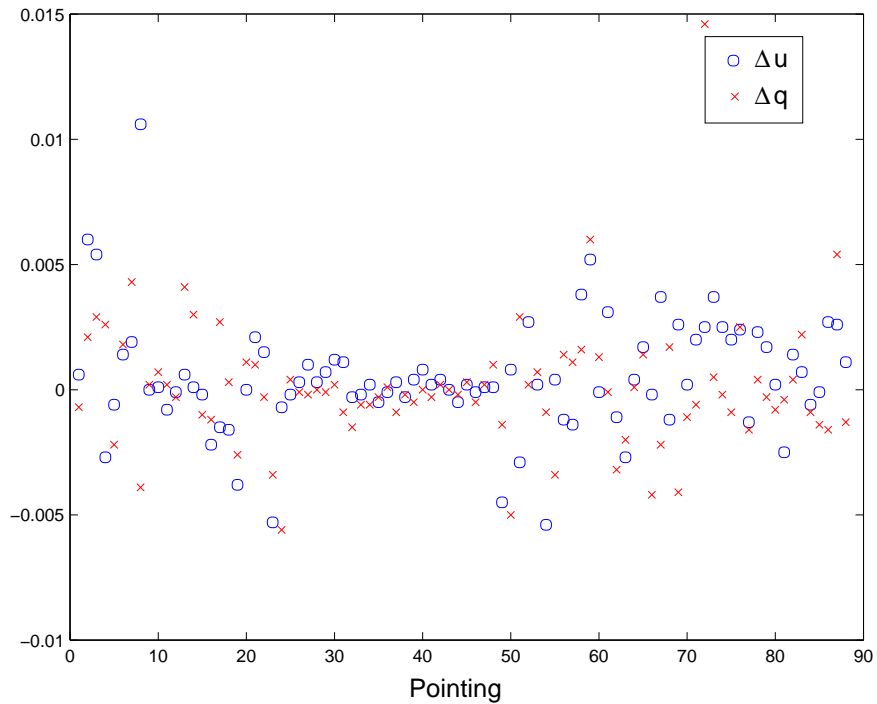


Figure 6.9. For each of the 88 pointings of SPARO, the difference between the measurements for the case of snow level 0 data alone and the case of snow levels 0 and 1 is plotted here for both q and u .

6.4. Time Dependence

As a precaution, it is necessary to consider the possibility that a long term drift systematic could be plaguing our data. In figure 6.10, the data have been binned by date and the polarization parameters have been plotted.

Note that there is no trend in the data indicating that this systematic is negligible. The spike at the fourth data point is due to a predominance of level 2 and level 4 snow on the tertiary on this date.

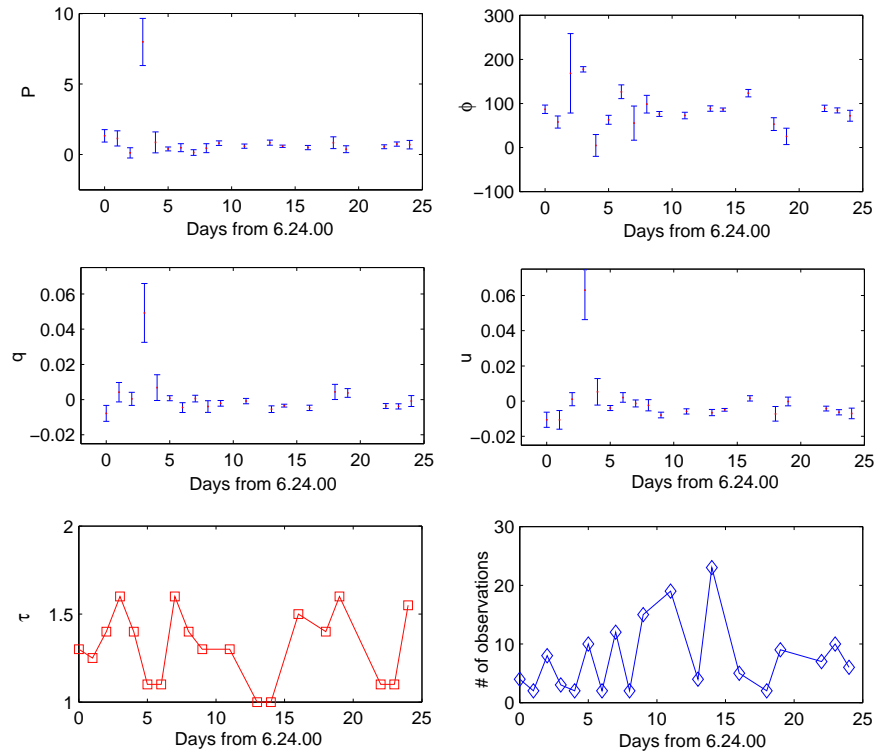


Figure 6.10. The various properties of measured polarization of Sgr B2 are plotted against time. Also plotted are two key measures that affect signal-to-noise: the optical depth of the atmosphere (τ) and the time of integration (number of observations).

6.5. Edge Effect

The edge effect refers to the effect of a possible spatial dependence of instrumental polarization within the focal plane. In other words, the measured polarization of a point source varies continuously across the focal plane and not discretely from pixel to pixel. For diffuse sources such as the CMZ, this should not be much of a concern, but we would like to try to test it. Normally, this effect can be measured

by moving a compact source around in a pixel and comparing its polarization measurements. For SPARO no point sources (e.g. planets) were available during Austral Winter 2000. The brightest, most compact source we have observed is Sgr B2. Since the position of Sgr B2 varies in our beam within a radius of about $0'.5$ (see chapter 5), it is possible to test for pointing dependent systematics (such as the edge effect) by plotting the polarization parameters versus position in both spatial coordinates (fig. 6.11).

The lines indicate the best fit line to the points. The top four figures represent the plots for right ascension and the bottom for are those for declination. These plots show no obvious systematics with respect to pointing or edge effect.

6.6. Final Data

Our chosen cutoff for signal-to-noise in the case of the SPARO data is 2.75. This threshold was chosen so as to maximize the big picture while still maintaining as large as possible of a cutoff threshold.

Combining polarization vectors can potentially supply additional high signal-to-noise measurements in areas where two observations overlap.

We define the spatial threshold for combining vectors to be $0'.5$. This corresponds to approximately 10% of a SPARO beam. This low threshold was chosen because in the area of bright sources (such as Sgr B2), pointing errors are the

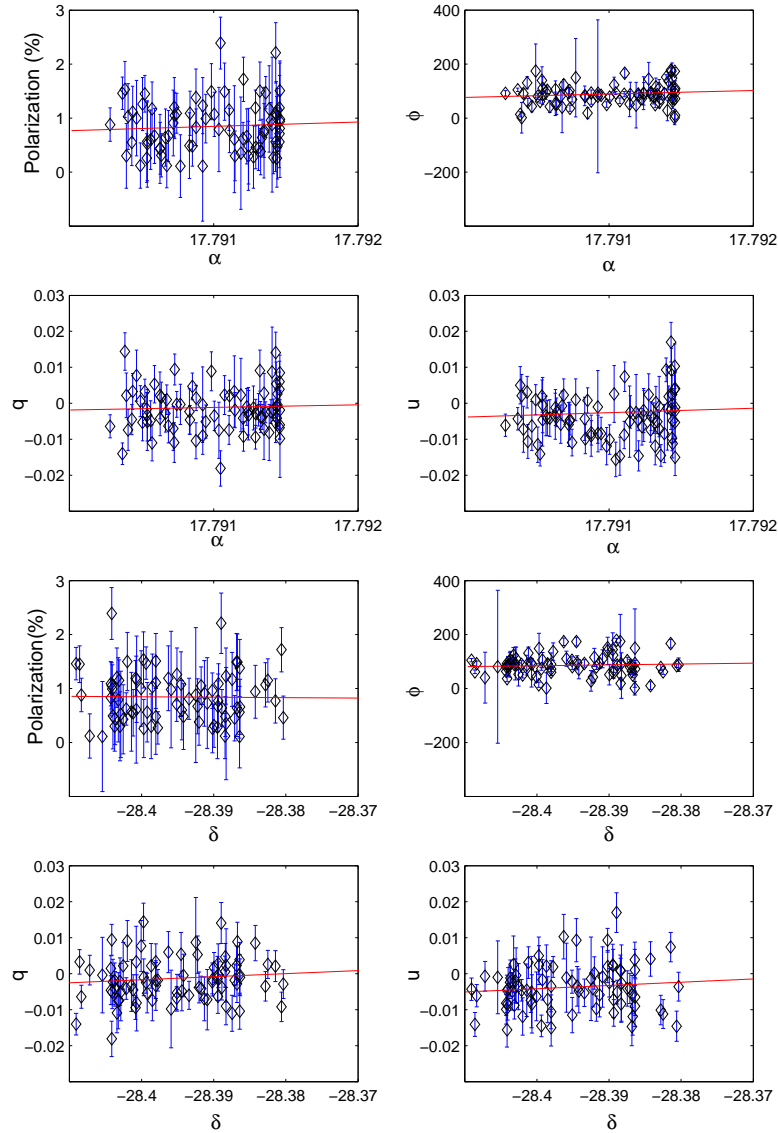


Figure 6.11. If the instrumental polarization varies on scales in the focal plane smaller than the size of a pixel, the polarization measured from the source could depend on the location of the source in the pixel. This is normally referred to as the “edge effect” and is tested here by utilizing Viper’s imperfect pointing. We measure the polarization parameters as functions of right ascension and declination and see that the straight line fits are relatively flat, thus exonerating SPARO of a significant edge effect.

Field 1	Field 2	Separation(arcminutes)	P	ϕ
B6	E4	0.5	0.57 ± 0.24	127.9 ± 11.8
B9	E7	0.5	1.0 ± 0.22	115.6 ± 6.4
C6	F4	0.5	1.22 ± 0.22	109.4 ± 5.2
C9	F7	0.5	1.42 ± 0.25	103.9 ± 4.8
L7	SgrB2:3	0.4	1.71 ± 0.34	110.7 ± 6.0
L8	SgrB2:4	0.4	1.20 ± 0.33	114.5 ± 8.2
N1	SgrB2:23	0.6	0.25 ± 0.21	31.1 ± 26.8
N2	SgrB2:22	0.6	0.42 ± 0.27	99.7 ± 19.24

Table 6.8. Overlap Candidates

dominant error introduced. This is supported in the region around Sgr B2 where the polarization changes fairly abruptly as one gets $\sim 10'$ away from the peak.

Table 6.8 contains potential overlap candidates. As one can see, there are 5 pairs that meet both the S/N and spatial criteria. In the final list of vectors, each pair that qualifies has been replaced by a single vector that is the weighted average of the two polarizations at an average position.

The final SPARO data are shown in the table 6.9. Thirty-seven points with $P/\sigma_P > 2.75$ were measured. The inferred magnetic field vectors are shown in figure 6.12 superposed on a photometry map taken with SPARO.

$\Delta\alpha^\dagger$	$\Delta\delta^\dagger$	P(%)	σ_P	ϕ	σ_ϕ	$\Delta\alpha^\dagger$	$\Delta\delta^\dagger$	P(%)	σ_P	ϕ	σ_ϕ
26.5	43.5	1.71	0.34	116.7	6.0	2.7	10.9	1.34	0.26	114.6	5.4
25.0	40.0	0.67	0.14	95.8	6.5	6.0	9.6	1.02	0.22	112.7	6.4
28.2	38.7	0.93	0.17	75.6	4.8	-5.2	5.9	2.13	0.74	108.2	9.5
23.7	36.7	0.53	0.06	88.5	3.0	-1.5	4.8	0.98	0.25	116.7	7.3
26.9	35.4	0.96	0.13	78.3	3.4	1.8	3.5	0.73	0.18	87.6	7.2
19.1	34.8	0.74	0.17	19.7	7.5	0.5	0.2	0.81	0.18	102.5	6.5
30.1	34.1	1.00	0.33	76.4	8.6	3.7	-1.1	1.09	0.22	103.1	5.9
14.9	32.7	1.35	0.43	112.9	9.0	1.6	-1.4	2.22	0.49	105.4	6.3
25.6	32.2	0.68	0.15	89.8	6.3	-4.5	-1.9	1.99	0.60	117.4	8.4
28.8	30.9	1.10	0.34	93.2	8.9	-0.8	-3.0	1.56	0.17	118.9	3.1
20.1	26.8	1.99	0.60	99.1	8.4	2.4	-4.3	1.57	0.21	110.6	3.8
15.5	24.9	2.55	0.60	100.5	6.6	-7.1	-4.6	1.31	0.45	120.1	9.6
13.9	20.5	2.25	0.76	124.0	9.5	-3.8	-5.9	0.83	0.27	117.9	9.2
8.5	17.0	2.13	0.54	121.7	7.2	-0.6	-7.2	1.53	0.27	120.8	5.1
8.0	15.3	1.74	0.48	116.9	7.7	-8.4	-7.8	1.57	0.43	155.9	7.9
3.8	14.0	1.42	0.25	103.8	4.8	-1.9	-10.5	2.00	0.31	116.2	4.5
7.3	12.8	1.08	0.22	119.7	5.8	-6.4	-12.4	2.31	0.40	122.8	4.9
10.5	11.5	1.53	0.34	126.3	6.3	-3.2	-13.7	1.48	0.36	119.5	6.7
23.1	44.5	2.05	0.61	131.6	9.0						

†Offsets in Right Ascension and Declination are measured relative to the position of Sgr A* in arcminutes.

Table 6.9. SPARO Polarimetry Results

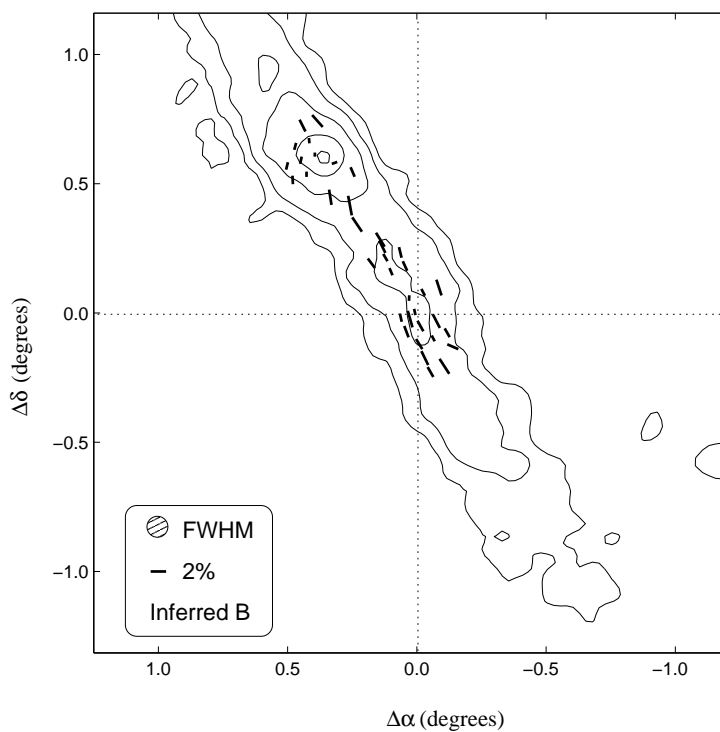


Figure 6.12. Inferred magnetic field vectors are shown plotted over the $450\ \mu\text{m}$ contours obtained with SPARO. The contour levels are at 0.075, 0.15, 0.30, 0.60 and 0.95 of the peak flux which is located at the position of Sgr B2. Positions are in offsets from Sgr A* in degrees.

CHAPTER 7

Hertz

7.1. Instrument Overview

Hertz optics and detectors are similar to those in SPARO; however there are notable differences. Whereas SPARO employs 9 bolometers in each array, Hertz has 32 arranged in six by six squares with the corners removed. Because of the difference in collecting area between the CSO and Viper, each pixel has a spatial resolution of $20''$ with a detector spacing of $18''$. The diffraction limit of the CSO at $350 \mu\text{m}$ ($1.22 \frac{\lambda}{D}$) is roughly $9''$, about half of Hertz's current resolution. Winston concentrators similar to those in SPARO are used in Hertz. These cones help to increase the coupling of the radiation to the bolometers; however, they take up excess physical space in the focal plane and prevent Hertz from being diffraction limited. The bolometers in Hertz are identical to those in SPARO (NTD-10 Ge) and operate at a temperature of 260 mK, cooled by a dual ^3He system. The transmission of Hertz is between 1.6%-1.8% (Dowell, et al. 1998).

7.2. Observing Scheme

The observing scheme of Hertz is similar to that of SPARO with one notable exception. Since the CSO is not located at the South Pole, the equatorial coordinate system does not co-align with the altitude azimuth coordinate system of the

telescope, and one has to concern oneself with the changing parallactic angle of a given source. The parallactic angle is simply the angle made by the great circle running from north to south with the great circle running from horizon to zenith at the location of the source on the sky. The parallactic angle is measured with the same convention as polarization angle; that is, measured east from celestial north. From the point of view of the array of detectors, the changing parallactic angle appears as a sky rotation with respect to the focal plane of the telescope. To compensate, Hertz is placed on an instrument rotator and the array is rotated so that for successive files, each pixel stays pointed on the same patch of sky (normally aligned with the equatorial coordinate system).

In addition, throughout an observation of a source, the pointing is changed by an integral amount of pixels and the dewar is also rotated by 90° . The purpose of this procedure is to allow different pixels to map to the same sky position. (This is known as changing boresightings.) This technique provides a number of cross-correlations that can be exploited in a large fitting program which is used to determine the polarizations of each pixel along with the instrumental polarization (Platt et al. 1991).

7.3. Analysis

There are two major differences between Hertz and SPARO data analysis. The first has been alluded to in the previous section and ties into the differences in observing method. While for SPARO the instrumental polarization is determined in separate tests, for Hertz the instrumental polarization is obtained via the same

large fit which is done for the data. The rotations and various boresightings give enough parameters to provide a non-degenerate solution for both the sky polarizations and those of the instrument for the various pixels.

The second difference in the analysis method involves something a bit more subtle. For SPARO, the relative gain for a corresponding pair of R and T pixels is obtained by normalizing each signal by the sum of that pixel's value over all of the half-wave plate positions.

$$(7.1) \quad R = \frac{R'}{\sum_{i=1}^6 R'_{\theta_i}}$$

$$(7.2) \quad T = \frac{T'}{\sum_{i=1}^6 T'_{\theta_i}}$$

The polarization signal is then calculated as described in § 4.4. Since each pair of pixels points at the same spot on the sky, the average measurement for each of the two bolometers should be the same. However, due to different responsivities and variations in gain from detector to detector, any pair of detectors is unlikely to have identical gains. The above correction compensates for this effect and leads to an accurate polarization signal.

This method is extremely effective if the noise in each pixel in a pair is uncorrelated. On the other hand, it is possible for noise to be correlated in corresponding pixels of the two arrays. The major source of correlated noise is changing atmospheric transmission over the course of a single polarization file (sky noise). In this case, the average unpolarized flux into either pixel is ill-defined and a new

approach is necessary. For a pair of pixels, if the polarization is low, the signal in the R array can be written in terms of the signal in the T array as $R = fT$, where f is the relative gain of R with respect to T. Notice that even with correlated noise, this relationship holds and f for each of the pixel pairs is simply the slope of an R v. T plot. Changing transmission does not affect f as R and T will rise and fall together. This method of calibration is detailed in Dowell et al. (1998) and is used in the Hertz analysis. The polarization signal in this case becomes:

$$(7.3) \quad S(\theta) = \frac{R(\theta) - fT\theta}{R(\theta) + fT\theta}$$

As a final note of comparison, the atmosphere at the South Pole seems to be more stable than that at Mauna Kea, and thus correlated noise is more of a problem at the latter site.

7.4. Results

Tables 7.1-7.7 show the Hertz data. We have set our signal-to-noise threshold to 3.

$\Delta\alpha^\dagger$	$\Delta\delta^\dagger$	$P(\%)$	σ_P	$\phi(^{\circ})$	σ_ϕ
-54	72	3.04	1.06	108.1	8.6
-36	72	2.21	0.71	99.1	9.0
-36	90	2.61	0.94	100.2	9.8
-36	108	4.98	1.48	102.4	7.8
18	-54	1.21	0.41	107.3	9.4
36	-54	1.41	0.40	91.3	8.1
54	-36	1.41	0.42	70.5	8.7
72	-90	1.83	0.57	97.4	8.7
72	-54	2.07	0.48	82.2	6.7
90	-54	2.46	0.57	87.2	6.6
108	-54	2.20	0.70	58.8	9.5

\dagger Sky positions are relative to $17^{\text{h}} 45^{\text{m}} 37^{\text{s}}.30, -29^{\circ} 5' 39''.78$ in arcseconds.

Table 7.1. Polarization Results for M-0.13-0.08

$\Delta\alpha^\dagger$	$\Delta\delta^\dagger$	$P(\%)$	σ_P	$\phi(^{\circ})$	σ_ϕ
-54	-18	2.76	0.85	107.6	8.8
-54	18	2.75	0.74	88.5	7.7
-36	-54	3.66	1.14	107.7	9.0
-36	-36	3.17	0.60	103.8	5.4
-36	-18	2.66	0.59	100.2	6.2
-36	0	3.16	0.63	91.3	5.7
-36	18	1.82	0.59	85.4	9.4
-36	36	3.08	0.73	80.3	6.8
-18	-54	3.20	0.89	112.8	8.2
-18	-36	1.46	0.39	98.0	7.7
-18	-18	1.74	0.42	78.5	6.9
-18	0	2.72	0.55	83.2	5.8
-18	18	2.33	0.56	66.4	6.8
-18	36	2.02	0.57	68.9	8.2
-18	54	2.20	0.69	63.2	9.6
0	-36	1.74	0.36	81.8	6.0
0	-18	2.09	0.32	95.2	4.3
0	0	1.13	0.32	75.1	8.2
0	18	1.88	0.43	79.6	6.5
0	36	2.75	0.45	60.7	4.7
0	54	2.47	0.80	79.0	9.6
18	-36	1.33	0.34	79.1	7.2
18	-18	2.13	0.30	91.3	4.1
18	0	1.18	0.27	73.3	6.6
18	18	2.27	0.39	63.7	4.9
18	36	3.08	0.60	76.5	5.7
36	-36	1.71	0.59	75.4	9.9
36	-18	1.69	0.38	68.6	6.5
36	0	1.98	0.30	67.6	4.3
36	18	2.43	0.52	63.5	6.3
36	36	3.53	0.85	67.7	7.0
54	-18	2.23	0.75	58.7	9.8
54	0	3.22	0.70	63.3	6.9

\dagger Sky positions are relative to $17^{\text{h}} 45^{\text{m}} 42^{\text{s}}.10, -28^{\circ} 56' 5''.1$ in arcseconds.

Table 7.2. Polarization Results for 50 km s^{-1} Cloud, Position 1

$\Delta\alpha^\dagger$	$\Delta\delta^\dagger$	$P(\%)$	σ_P	$\phi(^{\circ})$	σ_ϕ
-54	0	2.13	0.51	102.8	7.1
-54	36	1.68	0.47	80.7	8.0
-36	18	0.97	0.32	83.0	9.4
-36	36	1.45	0.40	79.0	7.8
-18	-36	2.05	0.41	92.9	5.8
-18	0	1.46	0.46	78.9	8.9
-18	36	2.01	0.46	61.9	6.4
0	36	1.33	0.46	73.3	9.7
18	-36	1.07	0.30	60.8	7.8
18	0	1.36	0.34	56.4	7.1
18	18	1.63	0.37	55.5	6.4
18	36	1.49	0.48	60.6	9.0
18	54	2.60	0.73	64.3	7.8
36	-36	0.98	0.34	66.7	9.7
36	-18	1.50	0.31	50.5	5.9
36	0	1.12	0.33	45.5	8.4
36	18	2.31	0.36	58.0	4.3
36	36	2.22	0.47	58.9	6.1
54	-36	2.56	0.80	52.2	9.0

†Sky positions are relative to $17^{\text{h}} 45^{\text{m}} 46^{\text{s}}.7, -28^{\circ} 57' 30''.0$ in arcseconds.

Table 7.3. Polarization Results for 50 km s^{-1} Cloud, Position 2

$\Delta\alpha^\dagger$	$\Delta\delta^\dagger$	$P(\%)$	σ_P	$\phi(^{\circ})$	σ_ϕ
-54	-18	0.84	0.26	68.8	9.1
-54	0	0.78	0.24	62.0	8.8
-54	18	1.33	0.23	55.8	5.0
-54	36	1.27	0.33	43.8	7.5
-36	-18	0.88	0.23	53.1	7.5
-36	18	1.17	0.21	37.2	5.0
-36	36	0.81	0.22	38.1	7.4
-36	54	1.13	0.35	48.7	9.1
-18	-36	1.52	0.22	57.9	4.4
-18	-18	1.46	0.23	43.4	4.5
-18	0	1.28	0.25	42.5	5.6
-18	18	1.46	0.37	42.2	7.2
-18	36	1.70	0.28	29.2	4.5
-18	54	2.35	0.36	42.7	4.4
0	-36	1.44	0.25	54.6	5.2
0	-18	1.58	0.26	41.0	4.6
0	0	1.58	0.26	39.5	4.7
0	18	1.92	0.42	29.4	5.8
0	36	1.99	0.40	44.0	5.7
0	54	2.16	0.45	47.3	6.0
18	-54	2.30	0.55	65.5	7.2
18	-36	1.08	0.30	41.1	7.9
18	-18	1.13	0.33	44.5	8.4
18	0	1.90	0.41	25.7	5.8
18	18	1.75	0.46	38.0	7.4
18	36	2.94	0.65	34.3	6.1
18	54	3.25	0.72	49.4	6.5
36	-36	1.81	0.51	45.0	8.1
36	-18	1.20	0.44	20.7	9.9
36	18	3.30	0.60	29.0	5.0
54	0	4.63	1.09	37.7	7.0
54	18	6.69	1.41	32.9	6.0

†Sky positions are relative to $17^{\text{h}} 45^{\text{m}} 55^{\text{s}}.0, -28^{\circ} 57' 29''.7$ in arcseconds.

Table 7.4. Polarization Results for 50 km s^{-1} Cloud, Position 3

$\Delta\alpha^\dagger$	$\Delta\delta^\dagger$	$P(\%)$	σ_P	$\phi(^{\circ})$	σ_ϕ
-54	-36	1.49	0.31	58.5	6.5
-54	-18	1.03	0.18	49.7	5.1
-54	0	1.26	0.16	49.3	3.5
-54	18	1.18	0.16	53.7	3.9
-54	36	1.44	0.26	53.0	5.0
-36	-54	1.38	0.38	54.7	8.1
-36	-36	1.30	0.22	43.5	4.8
-36	-18	0.67	0.18	47.3	7.6
-36	0	0.71	0.17	43.8	6.6
-36	18	0.80	0.16	39.1	5.8
-36	36	1.60	0.21	35.2	3.6
-36	54	1.34	0.38	41.3	8.2
-18	-54	2.38	0.56	34.4	6.5
-18	-18	0.59	0.19	37.5	9.2
-18	18	1.18	0.24	24.2	5.9
-18	36	2.15	0.23	36.1	3.0
-18	54	1.44	0.39	25.2	8.1
0	-54	2.25	0.64	51.1	8.2
0	-36	1.82	0.30	37.3	4.7
0	-18	1.52	0.21	31.0	4.0
0	0	1.15	0.21	39.6	5.1
0	18	1.94	0.26	37.9	3.8
0	36	2.53	0.32	28.0	3.6
0	54	2.27	0.56	37.6	7.3
18	-18	1.27	0.25	27.6	5.5
18	0	0.94	0.27	34.2	8.3
18	18	2.13	0.34	34.1	4.7
18	36	3.25	0.52	38.4	4.6
18	54	3.55	0.79	31.2	6.7
36	-18	1.61	0.35	29.8	6.4
36	0	2.25	0.38	39.7	4.9
36	18	2.48	0.45	39.1	5.2
36	36	4.00	1.19	41.0	8.6

†Sky positions are relative to $17^{\text{h}} 45^{\text{m}} 59^{\text{s}}.3, -28^{\circ} 59' 4''.5$ in arcseconds.

Table 7.5. Polarization Results for 50 km s^{-1} Cloud, Position 4

$\Delta\alpha^\dagger$	$\Delta\delta^\dagger$	$P(\%)$	σ_P	$\phi(^{\circ})$	σ_ϕ
-54	-18	2.64	0.88	49.3	9.5
-36	-18	1.76	0.47	60.7	7.8
-36	0	2.54	0.83	54.8	9.0
-36	36	5.82	1.97	46.2	9.6
-18	-54	2.04	0.60	37.4	8.6
-18	-36	1.44	0.27	45.0	5.4
-18	-18	1.18	0.28	48.1	6.8
-18	0	1.65	0.52	47.2	9.0
-18	18	2.16	0.76	57.6	9.2
0	-54	1.17	0.40	176.2	9.9
0	-36	1.13	0.23	4.4	5.8
0	0	0.62	0.22	55.2	9.9
18	-54	1.74	0.46	160.0	7.3
18	-18	0.88	0.23	158.1	7.5
18	54	2.39	0.80	131.4	9.5
36	-36	1.79	0.49	158.1	7.3
36	-18	2.13	0.30	138.7	4.0

†Sky positions are relative to $17^{\text{h}} 46^{\text{m}} 4^{\text{s}}.3, -28^{\circ} 54' 44''.3$ in arcseconds.

Table 7.6. Polarization Results for 50 km s^{-1} Cloud, Position 5

$\Delta\alpha^\dagger$	$\Delta\delta^\dagger$	$P(\%)$	σ_P	$\phi(^{\circ})$	σ_ϕ
-54	18	1.99	0.46	74.9	6.9
-54	36	1.62	0.55	73.2	9.9
-36	-36	1.09	0.35	113.1	9.2
-36	54	2.25	0.51	35.6	6.6
-18	36	1.14	0.29	61.7	7.6
18	-54	2.01	0.60	0.4	8.5
18	-36	0.84	0.22	174.3	7.6
18	-18	1.02	0.19	161.1	5.4
18	0	0.73	0.19	125.8	7.3
36	-36	1.95	0.43	168.1	6.5
36	-18	0.75	0.24	166.3	9.3
36	18	0.93	0.28	151.3	8.9
54	0	1.42	0.46	140.1	9.4

†Sky positions are relative to $17^{\text{h}} 46^{\text{m}} 10^{\text{s}}.2, -28^{\circ} 53' 6''.6$ in arcseconds.

Table 7.7. Polarization Results for 50 km s^{-1} Cloud, Position 6

CHAPTER 8

Discussion

Because the Non-Thermal Filaments (see § 2.2) are such convincing tracers of magnetic fields in the Galactic center, any model attempting to explain the magnetic field structure in this region must take them into account. Specifically, these NTFs trace a field that is geometrically poloidal.

In discussing the geometry of the Galactic center magnetosphere, we use the terms “poloidal” and “toroidal.” The term “poloidal” in referring to a field, indicates that the field (using cylindrical coordinates) lacks an azimuthal component, ϕ . “Toroidal,” on the other hand, refers to a field that has only a ϕ component (see fig. 8.1).

Uchida et al. (1985) have proposed a model in which an initially poloidal field (that is frozen into the matter) can be sheared out by the differential rotation of the Galaxy into a toroidal field in regions where gravitational energy density is greater than that of the magnetic field. Both SPARO and Hertz data will be used to test this model on two different spatial scales.

On large scales, the 6' resolution of SPARO can test the field in parts of the Galactic center that have uniform fields. At low Galactic latitudes, SPARO should see a toroidal field. Extending to higher latitudes, the field should return to a poloidal configuration as the matter densities fall off. The data taken in Austral

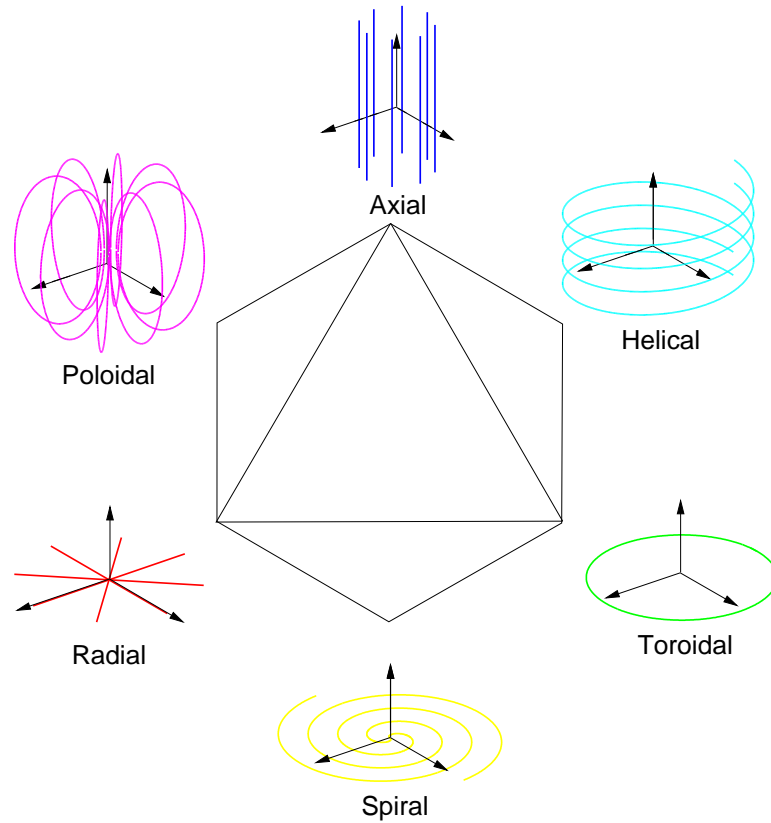


Figure 8.1. The basis set of fields in cylindrical coordinates is shown. This consists of, in $(\vec{B} \cdot \hat{e}_\rho, \vec{B} \cdot \hat{e}_\phi, \vec{B} \cdot \hat{e}_z)$, radial $(B_\rho(\rho, \phi, z), 0, 0)$, toroidal $(0, B_\phi(\rho, \phi, z), 0)$, and axial $(0, 0, B_z(\rho, \phi, z))$. Poloidal, helical, and spiral components can be generated by taking linear combinations of the elements of this primary basis. In this diagram, opposite pairs of field configurations can lead to complete descriptions of a field configuration. If \vec{B} represents a magnetic field, axial and radial fields are eliminated by $\nabla \cdot \vec{B} = 0$. A natural breakdown for magnetic fields is to use poloidal and toroidal fields since these are the geometries created by a circular and a linear current, respectively.

Winter 2000 have explored the first of these two regions and have found that the field is toroidal on large scales.

Hertz, on the other hand has high enough spatial resolution ($20''$) to explore finer spatial structure. In the central 30 pc, the matter distribution is clumpy on spatial scales resolvable with Hertz. Here, we find that the magnetic field structure is complex. Some regions contain poloidal fields, and some contain toroidal ones. We find that on the whole, the denser regions have fields that are preferentially toroidal. We argue that this can be explained by the model of Uchida et al. (1985) as it applies to a region with a clumpy matter distribution.

Throughout this discussion we will refer to “inferred magnetic field vectors.” Note that since we are dealing strictly with polarization by emission (see § 3.1.1), this refers to rotating the measured polarization vectors by 90° . The magnitude of an inferred magnetic field vector is simply the magnitude of the corresponding polarization vector.

8.1. The Large Scale Field

The magnetic field vectors inferred from the SPARO data (from table 6.9) are shown in figure 8.2 superposed on the 90 cm continuum image of the Galactic center (LaRosa et al. 2000). Also shown are contours tracing $850 \mu\text{m}$ flux as measured by SCUBA (Pierce-Price et al. 2000).

In figure 8.2, the direction of the Galactic plane can be seen in the $850 \mu\text{m}$ emission that traces the cold dust component. The SPARO data provide the best evidence to date that the magnetic field in the cold dust component on large scales is oriented parallel to the Galactic plane. From this we infer that the direction of

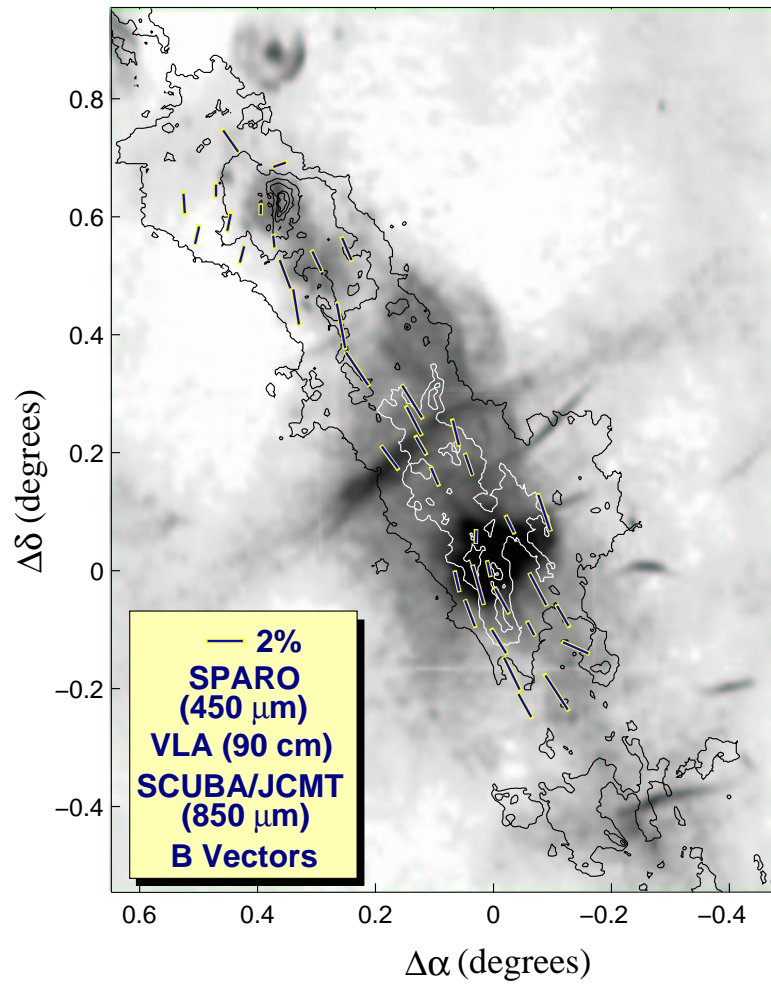


Figure 8.2. SPARO polarization data are superposed on a 90 cm map of the Galactic center (LaRosa, et al 2000). Contours show the 850 μm SCUBA data (Pierce-Price, et al 2000). Inferred magnetic field vectors are shown.

the magnetic field that permeates the cold dust is perpendicular to that traced by the Non-Thermal Filaments.

Novak et al. (2002) point out that the SPARO data are consistent with the model of Uchida et al. (1985) when juxtaposed with Faraday rotation measurements of the line-of-sight magnetic field direction. This model predicts a general toroidal dominance near the plane where gravitational energy density is large enough to drag magnetic field lines from a poloidal configuration to one that is toroidal. This prediction is verified by the SPARO data that show a toroidal field configuration in the dust emission of the CMZ. The model also predicts that on large scales, the direction of the line-of-sight component of the magnetic field should vary from quadrant to quadrant of the Galactic center. At positive Galactic longitudes, where the rotation of the Galaxy causes the matter move away from us, one expects that shearing of an initially poloidal field will produce a line-of-sight component of the magnetic field at positive Galactic latitudes that is opposite that at negative latitudes. At negative Galactic longitudes, a negative image of the sign pattern is produced such that fields in opposite quadrants are expected to have the same signs.

Line-of-sight magnetic fields that pass through ionized gas produce different indices of refraction for right and left-handed circular polarization states of the observed radiation. The resultant effect on linearly polarized radiation is a wavelength-dependent rotation of the polarization vector. The direction of this rotation depends on the direction of the line-of-sight magnetic field. This effect is called Faraday rotation (Harwit 1998) and has been measured for linearly polarized NTFs in each of the four quadrants (Lang, Morris and Echevarria 1999) of

the Galactic center. The result is in agreement with that predicted by the model described above.

In the region of figure 8.2 between Sgr A East and the GCRA where few vectors are present, SPARO has placed upper limits on the polarization of $\sim 0.5\%$. Two possibilities exist to explain this deviation from uniform polarization: either the polarization is inherently low in this region because of poor grain alignment or weaker magnetic fields, or the structure of the field in this region varies on scales smaller than SPARO's beam can measure.

8.2. Morphology of the Inner 30 Parsecs

The Hertz observations have focused on this region of the Galactic center in which SPARO fails to measure significant polarizations. The results of the new 2001 observations are listed in tables 7.1-7.7. The magnetic field vectors inferred from these data are displayed in figure 8.3 combined with those of Novak et al. (2000) (region III). Also shown in this figure are $100\ \mu\text{m}$ data from the Kuiper Airborne Observatory (Dotson et al. 2000) of the Arched Filaments (region II) and $60\ \mu\text{m}$ data (Dotson et al. 2000) of the Sickle (region I). The contours trace $850\ \mu\text{m}$ flux (Pierce-Price et al. 2000). Major molecular features are labeled.

8.2.1. M-0.13-0.08

One feature of interest in figure 8.3 is the molecular cloud M-0.13-0.08 (commonly called the $20\ \text{km s}^{-1}$ cloud). This cloud has an elongated shape, and its long axis is oriented at a shallow (15°) angle to the Galactic plane. In projection, the

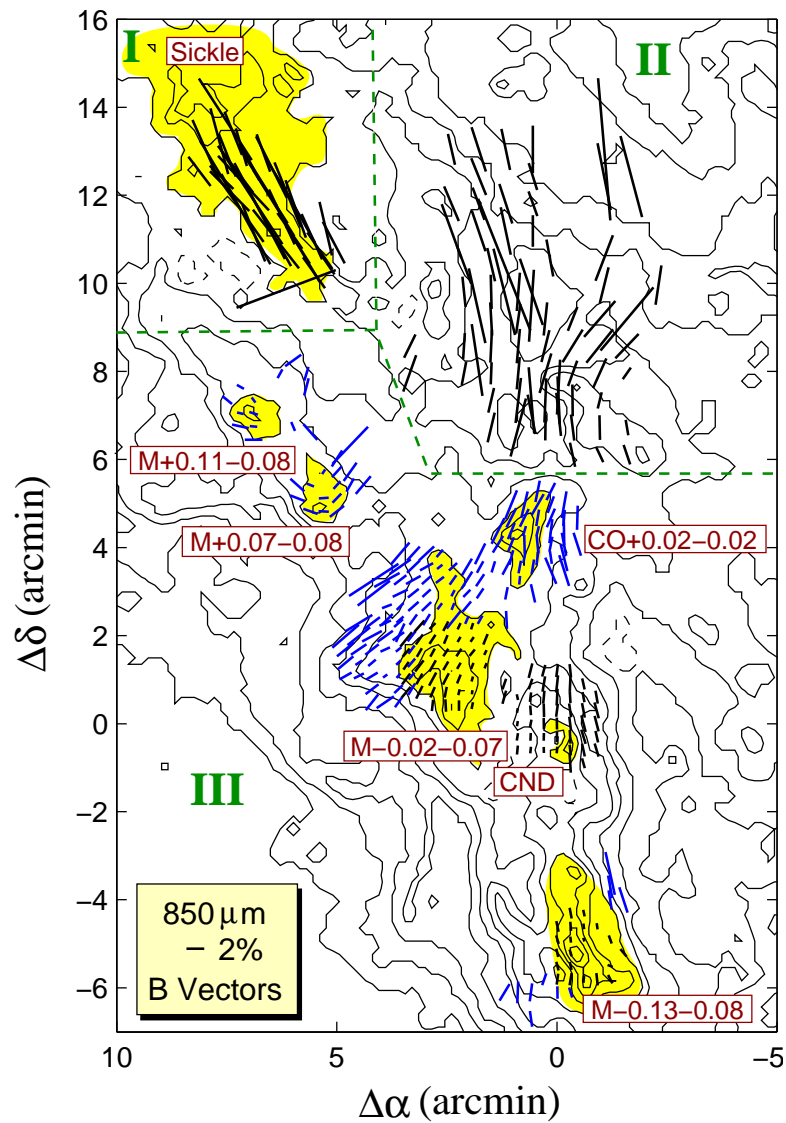


Figure 8.3. The inferred magnetic field directions for polarization measurements in the Galactic center are displayed on 850 μm contours from SCUBA/JCMT (Pierce-Price et al. 2000). Region I shows 60 μm polarimetry of the Sickle (Dotson et al. 2000). Region II shows 100 μm polarimetry of the Arched Filaments (Dotson et al. 2000). Region III shows new 350 μm inferred magnetic field vectors along with the 350 μm vectors from Novak et al. (2000). Important dust features are shaded and labeled.

long axis of this cloud points in the direction of Sgr A*. This fact is suggestive that this cloud is undergoing a gravitational shear as it falls toward Sgr A*. This is supported by other observations including a high velocity gradient along the long axis (Zylka, Mezger and Wink 1990), increasing line widths and temperatures along the cloud in the direction of Sgr A* (Okumura et al. 1991), and an extension of the cloud detected in NH₃ emission to within 30'' of Sgr A* in projection (Ho et al. 1991).

Novak et al. (2000) have discovered that the magnetic field structure is such that the field is parallel to the long axis of the cloud. They point out that for gravitationally sheared clouds, a consequence of flux-freezing is that regardless of the initial configuration of the field, the field will be forced into a configuration in which it is parallel to the long axis of the cloud. In addition, these authors note that this is not only true for the dense material inside of the cloud, but also for the more diffuse molecular material that belongs to the ambient region. They note that the southern end of this cloud exhibits a flare both morphologically and in magnetic field structure. They suggest that this flare is a connection to the large scale vertical field traced by the NTFs.

Our 7 new vectors in this region provide additional support for this interpretation, but a more extensive mapping of this cloud is necessary before a complete interpretation is made.

8.2.2. G0.18-0.04

The H II region G0.18-0.04 (commonly called the “Sickle”) can be seen in 20 cm thermal emission in figure 8.4. It is believed to be the ionized surface of a molecular cloud that is interacting with the Radio Arc (Serabyn and Güsten 1991). Its molecular counterpart can be seen in the 30 km s^{-1} panel of figure 8.5. It has even been suggested that this interaction is responsible for producing the relativistic electrons necessary to light up the Radio Arc via magnetic reconnection (Davidson 1996).

The relationship between the geometry of the cloud and its magnetic field structure is similar to that of M-0.13-0.08. The cloud is elongated parallel to the plane of the Galaxy and its magnetic field as inferred from far-infrared polarimetry is parallel to the long axis. These similarities to M-0.13-0.08 suggest that the origin of the field in both cases is the same.

One difference between these two clouds is that unlike M-0.13-0.08, there is no observed flaring of the field in the molecular material associated with the Sickle. In fact, there seems to be little evidence for a connection between the toroidal field geometry of the molecular material and the pristine poloidal geometry of Radio Arc. There are several possibilities for why this might be the case. First, the polarimetry coverage may be too limited in this region. If enough data are taken, we may see a return to a poloidal field in the surrounding region. Second, this cloud may be more evolved than M-0.13-0.08, and so we may be observing a magnetic field that has had enough time to shear into a more parallel configuration

than that of M-0.13-0.08. Finally, because this molecular cloud is farther from Sgr A* than is M-0.13-0.08, the tidal forces on it are weaker, thus allowing for a more uniform shearing along its length.

8.2.3. M+0.11-0.08 and M+0.07-0.08

M+0.11-0.08 and M+0.07-0.08 are two peaks of a molecular cloud complex that, like M-0.13-0.08 and the molecular cloud associated with the Sickle, is elongated nearly parallel to the plane with its long axis pointed toward Sgr A*. The radial velocity of this complex has been measured to be 50 km s^{-1} (see 50 km s^{-1} panel of fig. 8.5).

The inferred magnetic field configuration for this complex is quite interesting. The field appears to wrap around the southern and eastern edges of this cloud. From this configuration, we conclude that the cloud is moving toward Sgr A* in projection and is sweeping up magnetic flux from the intercloud medium as suggested by Novak et al. (2000) for the case of M-0.13-0.08. The direction of travel inferred from the polarization data indicates that in projection, this cloud is moving toward a region dominated by a poloidal field (see northeast side of M-0.02-0.07 in fig. 8.3). As the cloud moves through the less dense intercloud medium, this poloidal flux then is wrapped around the cloud into a toroidal configuration as seen along the eastern edge of the cloud.

Interior to this cloud complex, there are few measurements; however, those that exist hint at a field that is parallel to its long axis, similar to that of M-0.13-0.08 and the molecular cloud associated with the Sickle.

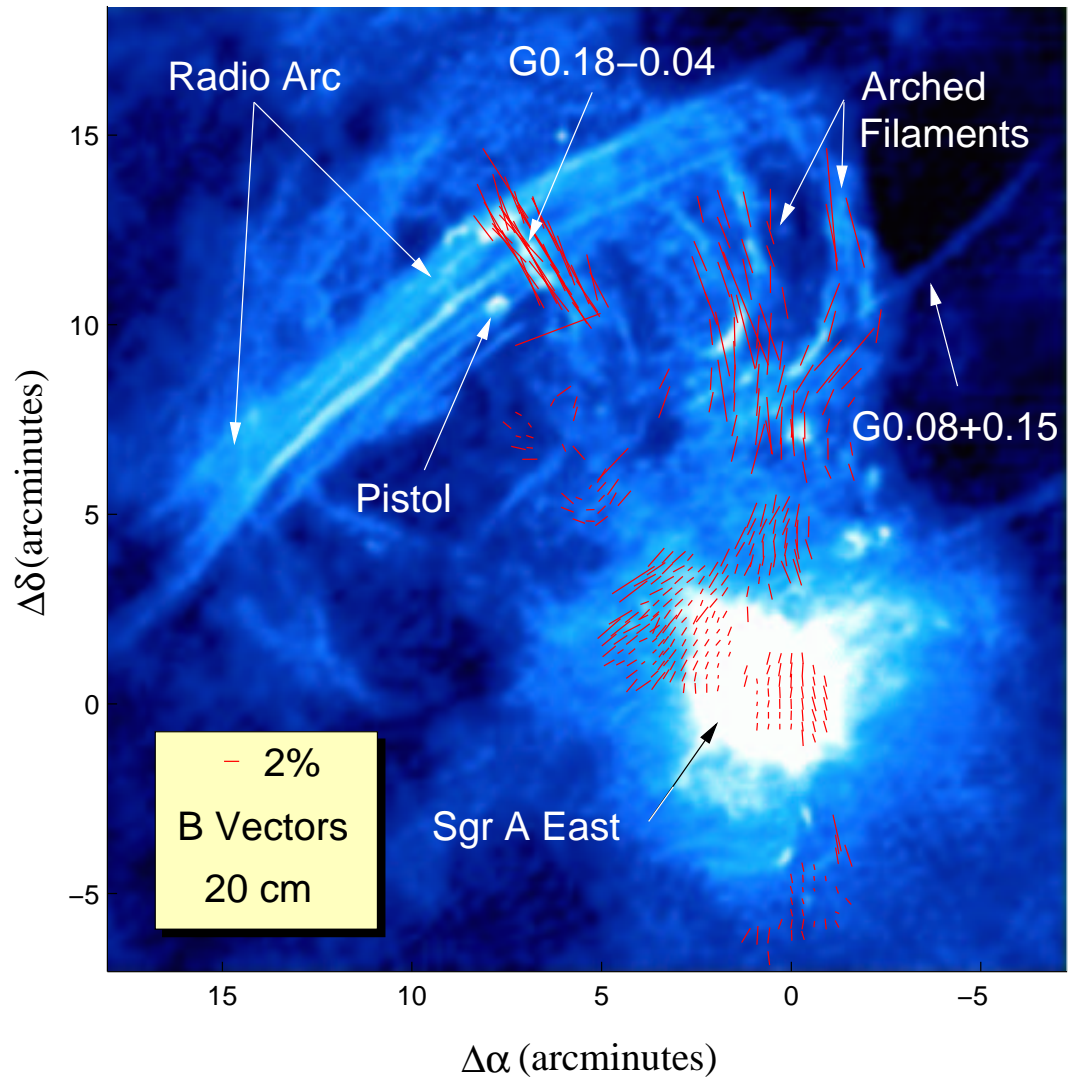


Figure 8.4. Inferred B vectors are superposed on a 20 cm map (Yusef-Zadeh, Morris and Chance 1984) taken with the VLA. Important thermal and non-thermal structures are labeled. The $100\ \mu\text{m}$ vectors appear to trace the Arched Filaments. The field in the molecular cloud associated with G0.18-0.04 is perpendicular to the field associated with the Radio Arc.

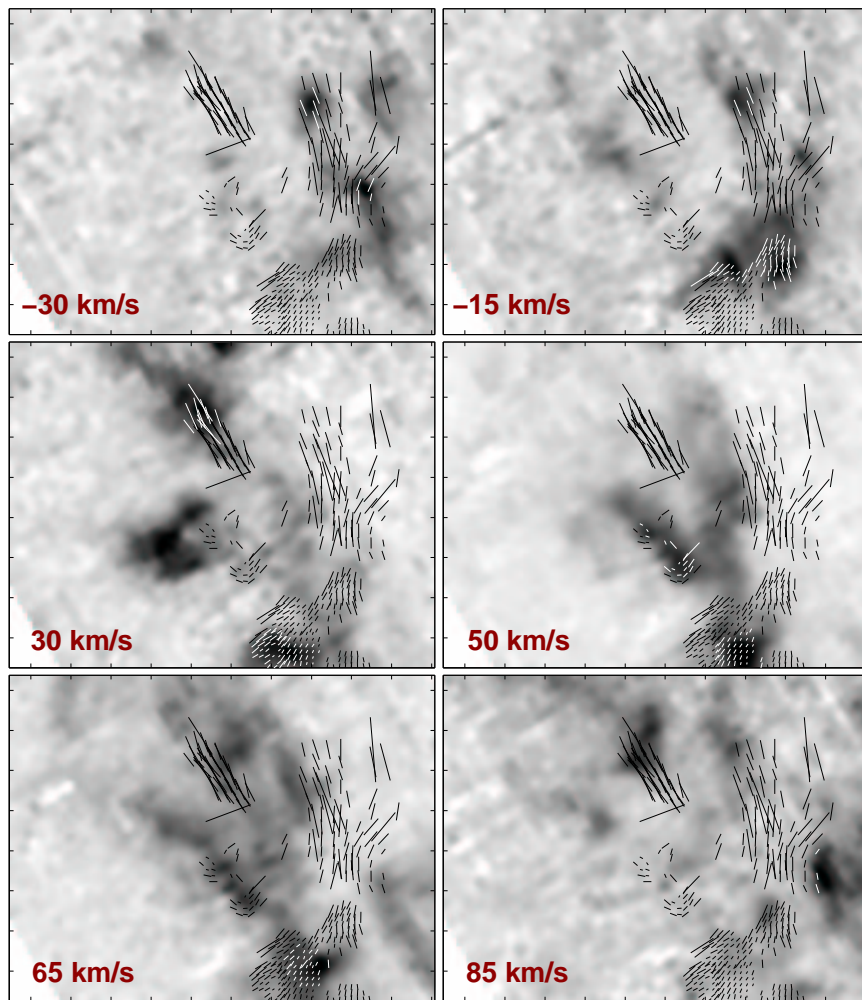


Figure 8.5. CS velocity maps (Tsuboi, Ukita and Handa 1997) are shown with polarization data superposed.

8.2.4. The X Polarization Feature

The $350 \mu\text{m}$ polarimetric observations of M-0.02-0.07, the CND, and CO+0.02-0.02 provide evidence for a magnetic field structure that is contiguous with that derived from the $100 \mu\text{m}$ polarimetric observations of the Arched Filaments to

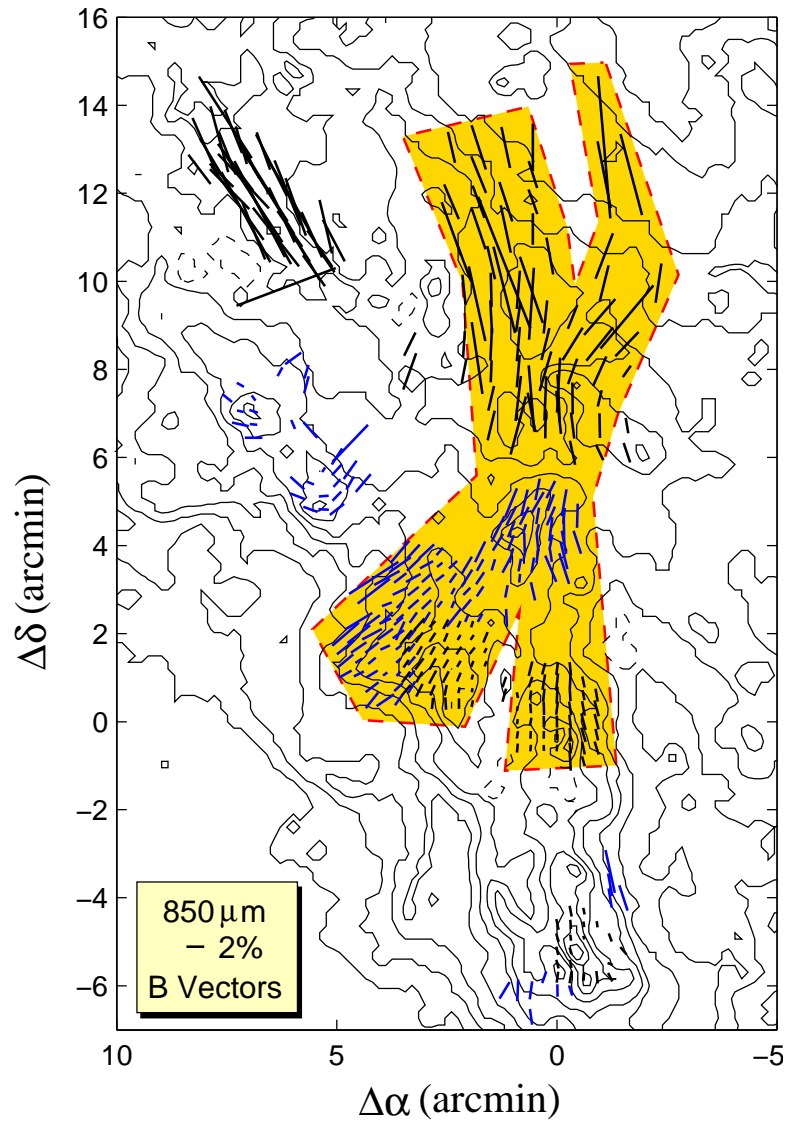


Figure 8.6. This is a reproduction of figure 8.3 in which the X Polarization Feature has been shaded.

form an “X-shaped” feature that we will refer to as the “X Polarization Feature.” (See fig. 8.6.) The most interesting aspect of this feature is that the magnetic field in the dust seems to be coherent over scales (30 pc) significantly larger than

those of typical molecular clouds in this region (5-10 pc). This implies a degree of decoupling of polarization measurements from the dense molecular clouds. In other words, there is a component of cold dust that exists in the intercloud medium that is emitting polarized radiation.

In the following discussion, we present two possible explanations of the X Polarization Feature.

The first possibility is that the X Polarization Feature corresponds to a single physical structure that is subject to the dynamics of the Galactic center. This hypothesis is motivated by the continuity of the polarization vectors over distances of up to 30 pc. However, unlike for the case of the individual clouds discussed above, there are no submillimeter nor radio features that are traced by the entire length of this feature.

On the other hand, a corresponding photometric structure is shown in figure 8.8 where the magnetic field vectors are superposed on an 8 μm (Band A) map from the MSX/SPIRIT III survey (Price et al. 2001) of the Galactic plane. The scale of this structure is large compared to the size of molecular clouds in this region.

In figure 8.8, 7.2 μm PAH line emission makes a contribution to the measured flux (Simpson et al. 1999); however, it is unlikely that PAHs are responsible for far-infrared and submillimeter fluxes. There could exist a cold dust component within the structure traced by these PAHs. Such a component could be responsible for the polarization we measure.

The shape of the eastern side of the X Polarization Feature suggests that the magnetic field vectors trace out a curve of some radius. This curve could be

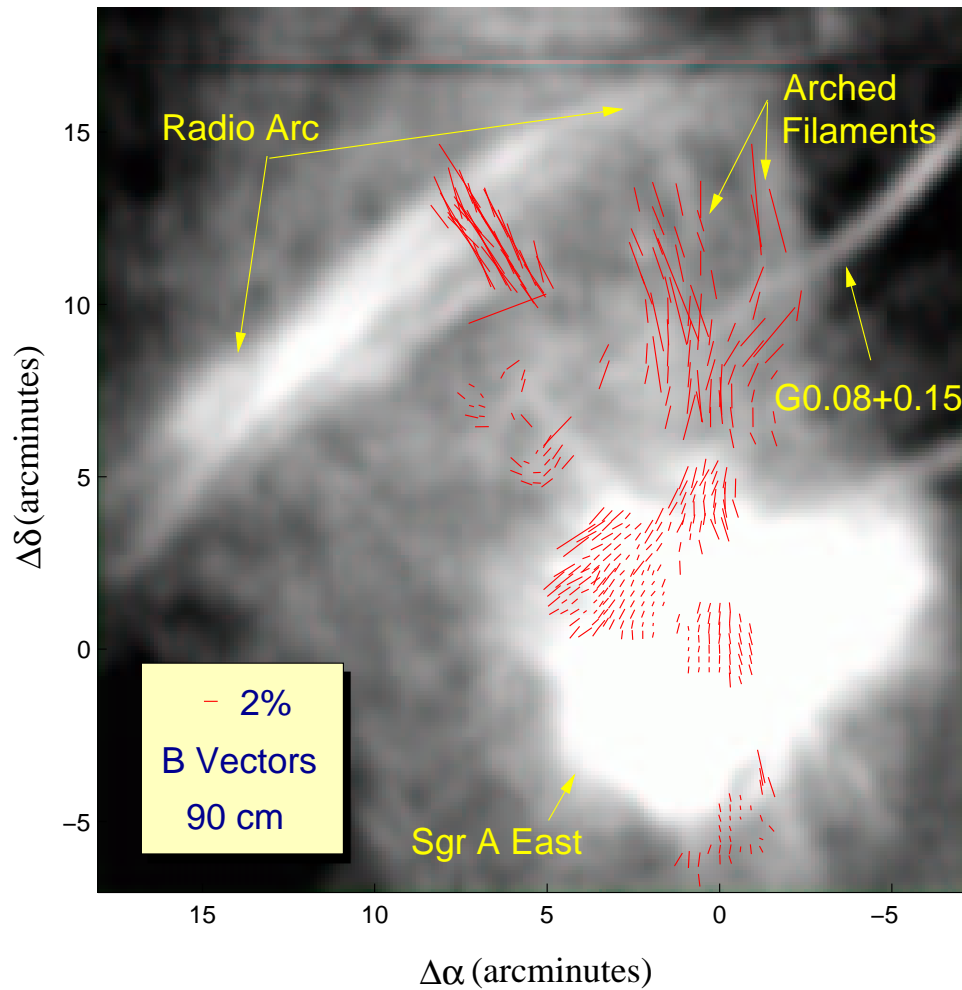


Figure 8.7. Inferred B vectors are superposed on 90 cm map (LaRosa et al. 2000) taken with the VLA. Here, the NTFs are more prominent than in figure 8.4 due to the power law spectra of non-thermal sources. The field as inferred from far-infrared polarimetry at the western edge of the Arched Filaments seems to follow the Northern Thread.

a two dimensional projection of the surface of a bubble produced by some sort of explosion. To investigate this possibility, we have used data from tables 7.2 through 7.5 and those from the Arched Filaments (Dotson et al. 2000) having

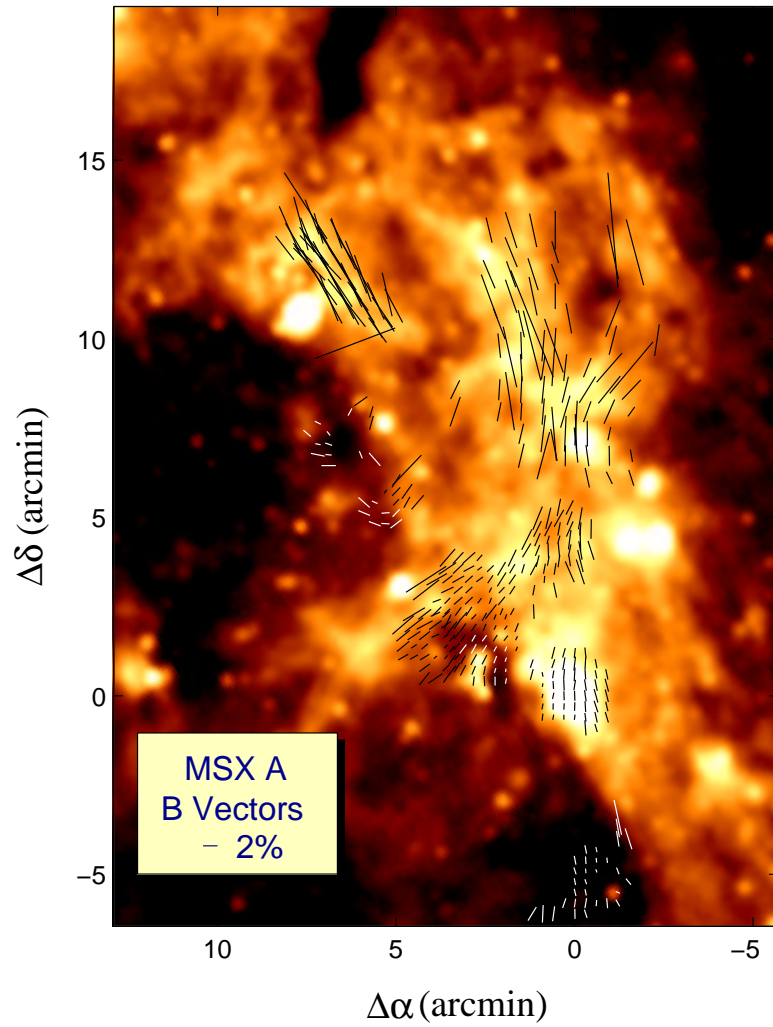


Figure 8.8. Inferred B vectors superposed on $8 \mu\text{m}$ map of Galactic center from the MSX/SPIRIT III survey.

$\Delta\alpha > 0$. We compare the intersection of each pair of polarization vectors in this set of data. Results are shown in figure 8.9. The mean position of intersection is calculated giving the center of curvature to be $(\alpha, \delta) = (17^{\text{h}}46^{\text{m}}16^{\text{s}}.9, 28^{\circ}53'8''.7)$. No evidence has been found for any unusual sources near this location.

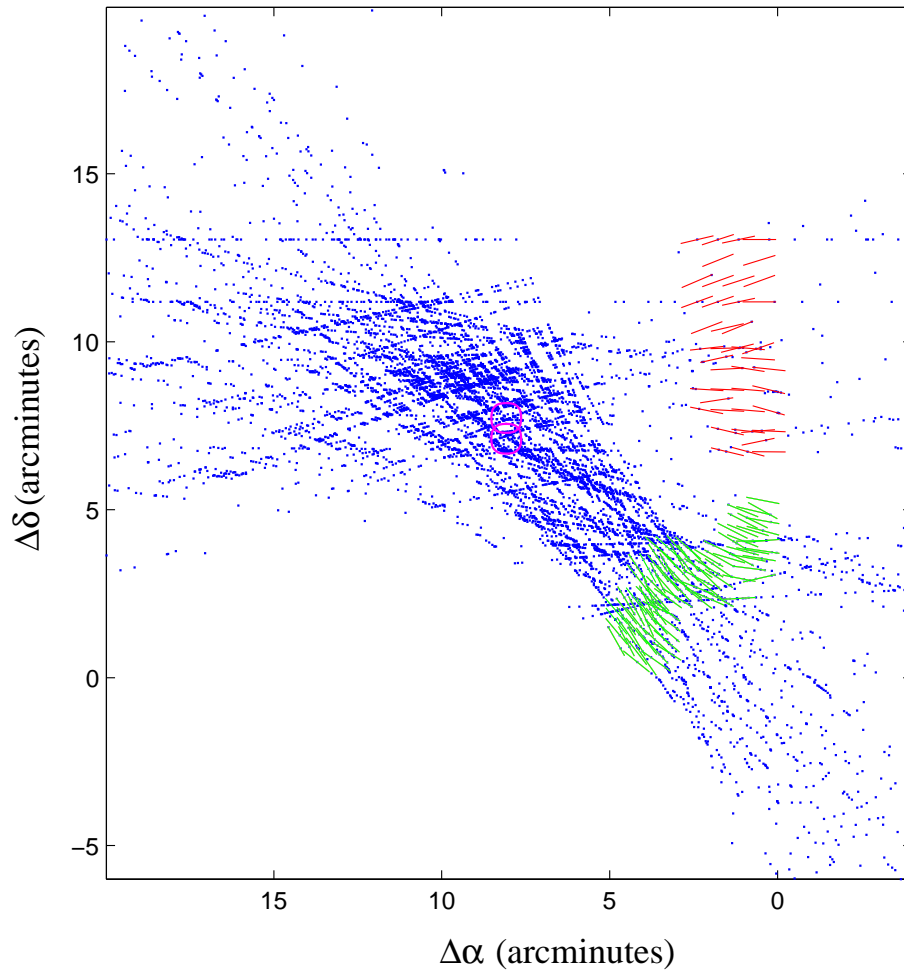


Figure 8.9. The intersection of each pair of polarization vectors for point locations in the structure which corresponds to the Arched Filaments has been determined, and the mean and median position of a projected “center of curvature” were determined to be (in arcminute offsets from Sgr A*) $(\Delta\alpha, \Delta\delta) = (8.077, 7.736)$ and $(8.077, 7.115)$, respectively. These positions are marked by the circles near the center of the figure.

The second possible interpretation is that the X Polarization Feature is a line of sight superposition of regions of poloidal and toroidal fields. In this picture, the Galactic center is clumpy. The orientation of the observed magnetic field at any given location depends on the relative polarized emission from poloidal and toroidal clumps that intersect the line of sight.

The poloidal field is seen to dominate in the eastern part of the M+0.02-0.07 cloud and at the western edge of the Arched Filaments. The toroidal field dominates in the eastern edge of the Arched Filaments and around the CND. The two fields mix in CO+0.02-0.02.

Another example of line of sight mixing of poloidal and toroidal fields occurs at the western edge of the Arched Filaments. Here, we see several magnetic field vectors oriented perpendicular to the plane that are in close proximity to the NTF G0.08+0.15, a feature that traces a poloidal field. Just to the north, the magnetic field vectors return quite abruptly to a toroidal configuration in the vicinity of the molecular features that correspond to the Arched Filaments (see fig. 8.5). It is possible that the molecular material at $v \sim -25 \text{ km s}^{-1}$ is displaced along the line of sight from G0.08+0.15, and the net polarization observed consists of contributions from dust associated with the respective neighborhoods of these two features. To the south of G0.08+0.14, the vectors again become indicative of a toroidal field as they wrap around the molecular cloud visible in the 85 km s^{-1} panel of figure 8.5.

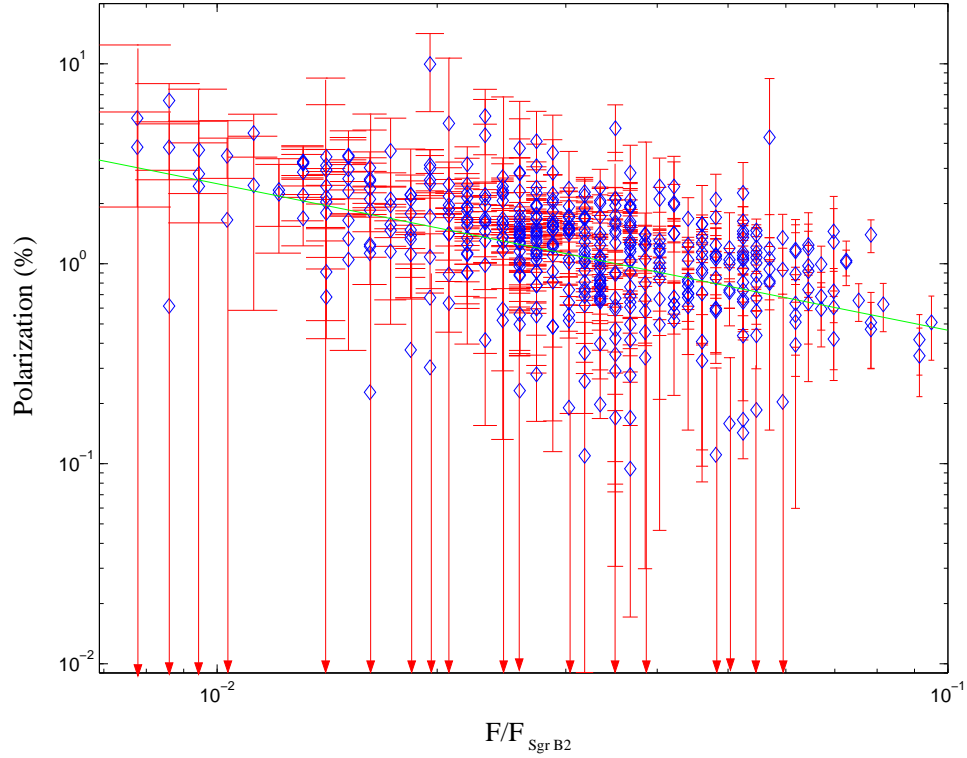


Figure 8.10. The polarization as measured by Hertz is compared with the $350 \mu\text{m}$ SHARC flux (Dowell et al. 1998). We find a slope of -0.73 . We have included all measurements with a signal-to-noise greater than 1 and have corrected the polarizations according to $P' = \sqrt{P^2 - \sigma_P^2}$ (Serkowski 1974).

8.3. Polarized Flux

Figure 8.10 shows a plot of Galactic polarization measured by Hertz versus $350 \mu\text{m}$ flux as measured by SHARC. A linear fit gives a slope of -0.73 . In this plot, we have included all points with a polarization signal-to-noise (S/N) greater than 1 and have corrected the polarization by $P' = \sqrt{P^2 - \sigma_P^2}$ in order to account for the systematic overestimation of polarization (Serkowski 1974) inherent in the

conversion from q and u to P and ϕ . The reason for such a low cut-off is to avoid biasing the measurement by systematically eliminating low S/N points with low fluxes and low polarizations. However, a data set dominated by random noise would produce a slope of -1 in a log-log plot of polarization versus flux. By raising the cutoff to a S/N of 3, the slope only increases to -0.67 and thus it is reasonable to conclude that the origin of the slope is physical and not systematic. In addition, a polarization versus flux comparison for individual pointings of Hertz gives an average slope of -0.96 ± 0.32 .

This slope is similar to the values found by Matthews et al. (2001; 2002) for various Galactic molecular clouds. Matthews et al. (2002) suggest three possibilities for the depolarization effect. First, the lower polarization could be due to poor grain alignment or low polarization efficiency in the cores of these clouds. Second, the depolarization could be a result of a geometrical projection of a three dimensional helical field. Finally, it is possible that the spatial structure of the magnetic fields in the cores of clouds is too small to be resolved by Hertz's beam.

The evidence for depolarization in the Galactic center does not provide enough information to differentiate among the three proposed explanations; however, it does indicate that the depolarization effect is observable in clouds that are a factor of ~ 10 larger than molecular clouds in the disk.

On the other hand, the same study done with SPARO data in the Galactic center (see fig. 8.11) gives a slope of -0.24, a value much closer to zero. Thus, this depolarization effect is not nearly as significant at the 200 pc scale.

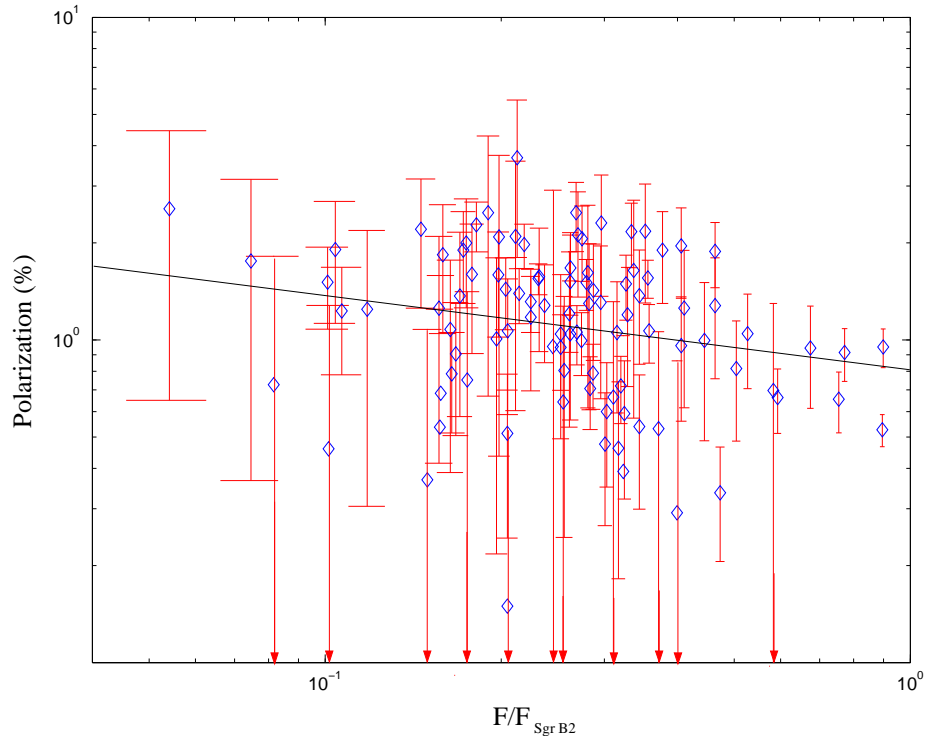


Figure 8.11. The polarization versus flux relation for SPARO data in the Galactic center shows a much weaker relationship than for Hertz data. The slope of this line is -0.24 and could potentially be an artifact of low signal-to-noise. Points with signal-to-noise > 1 were included and corrected according to $P' = \sqrt{P^2 - \sigma_P^2}$.

While SPARO does not see a flux-dependent depolarization, it does see a general decrease in the magnitudes of polarization near the 30 parsecs of the Galactic center (see fig. 8.2). Our Hertz data indicate that on average, the degree of polarization in this region is not significantly less than that for the outer regions of the CMZ measured by SPARO. In this case, the lower polarizations are a result of magnetic fields varying on scales too small to be detected by SPARO. While this

suggests that depolarization is due to insufficient spatial resolution, the only way to test for this in bright peaks of molecular clouds is to measure those regions with a polarimeter with better spatial resolution.

The most important conclusion from figure 8.11 is that it provides evidence that the SPARO data are free from reference beam contamination that could have affected the data. This will be discussed in § 8.4.

8.4. Reference Beam Contamination

8.4.1. Theory

In performing differential measurements using chopping techniques (see § 4.4), polarized flux in the reference beam positions is a potential hazard. Several attempts have been made to quantify this issue (Novak et al. 1997; Schleuning et al. 1997; Matthews, Wilson and Fiege 2001). The goal of this section is to assess the level of reference beam contamination in our data.

For a general Stokes' parameter, x , the measured value, x_m , is related to the value in the source beam, x_s , the average value in the reference beam, x_r , and the relative strength of the average flux in the reference beams compared to that in the source beam, $\eta \equiv I_r/I_s$ by

$$(8.1) \quad x_m = \frac{x_s - x_r \eta}{1 - \eta}.$$

8.4.2. SPARO Data

To estimate the effect of reference beam contamination on polarimetry data, we first consider the extreme case of a highly polarized reference beam and a source with zero polarization. In this case, all of the measured polarized flux originates from the reference beam, and thus the measured polarized flux will be independent of source flux. A constant polarized flux means that as flux in the source beam increases, the measured polarization decreases, leading to a slope of -1 in a log-log plot of polarization versus flux. As seen in § 8.3, a slope of -1 can have many origins; however, a slope of zero indicates a negligible reference beam contamination. Because the slope of figure 8.11 is far from -1, we conclude that there is no significant reference beam contamination for the SPARO data. This conclusion will be used in the next section to place upper limits on the reference beam contamination for Hertz.

8.4.3. Hertz Data

Because we are trying to uncover the geometry of magnetic fields, we concern ourselves with reference beam contamination as it applies to Hertz insofar as it affects the polarization angle measured. As a worst case scenario, if $\eta < 1$, and $x_r \eta > x_s$, a polarization in the reference beam could show up rotated by 90° in the final measurement.

In order to get a handle on the effect of this contamination, we used the SCUBA 850 μm map (Pierce-Price et al. 2000) to find η by averaging the flux in a Hertz

array footprint and comparing it to the average flux in the reference beams of our 8 observation fields. We used the SCUBA map here because its good sensitivity to extended flux gives the most conservative estimate of reference beam contamination. From this study, we have found that on average, $\eta \sim 0.5$. From the SPARO observations, the upper limit of polarization at $450 \mu\text{m}$ is 2%. Because of sky rotation during the course of an observation, the Hertz reference beam is spread out over the sky, so that this 2% upper limit should apply to the Hertz data, assuming no large wavelength dependence from $450 \mu\text{m}$ to $350 \mu\text{m}$. Under these assumptions, the source position must be polarized by less than 1% in order for reference beam contamination to begin to dominate. Since a good deal of our vectors have $P > 1\%$, and we see no sudden 90° spatial discontinuities in our polarization data, we conclude that although reference beam contamination may affect the magnitude of our polarization, there is little effect on the measured polarization angle. This is further evidenced by the correlation of the position angles with morphological features.

Reference beam contamination is a potential problem with Hertz because of Hertz's small ($6'$) chop throw. SPARO's larger (0.5°) chop throw does not have this problem. However, it should be noted that Hertz's small chopper throw may be an advantage to investigating fields near the Galactic center. If the molecular material between the central 40 pc of the Galaxy and the Sun is gravitationally dominant and therefore has a fairly uniform toroidal field, it may be desirable to "chop out" the extended uniform component of the polarization. Because of this,

we may be probing only the central core of the Galaxy's magnetic field with these measurements.

8.5. Poloidal Versus Toroidal Fields

In studying the magnetic field in the central 30 pc of the Galaxy, we revisit the model of Uchida et al. (1985) as it applies to the Galactic center. Specifically, we keep in mind that the Galactic center is clumpy and that some regions seem to be dominated by a field that is poloidal while others are dominated by a field that is toroidal. In the spirit of this model, we adopt a picture in which gravity is assumed to dominate the dynamics in regions of toroidal fields while in regions of poloidal dominance, magnetic fields are energetically more important.

8.5.1. Dependence on Galactic Longitude

Figure 8.12 shows a plot of the polarization angle (ϕ) versus distance from Sgr A* in arcminutes of Galactic longitude. The upper and lower 20° bands are centered on polarization angles that correspond respectively to toroidal and poloidal fields. From this plot, it is evident that there is a section of the Galactic center, located between Sgr A East and the Radio Arc, in which the field as measured in the cold dust component is preferentially poloidal. As one goes away from this section in either direction, the field very quickly returns to a nearly toroidal configuration.

The fact that the region of the poloidal field is offset from the location of Sgr A* is a bit mysterious; however, it is not any more mysterious than the general asymmetry of matter distribution in the Galactic center (see fig. 8.2). It is also

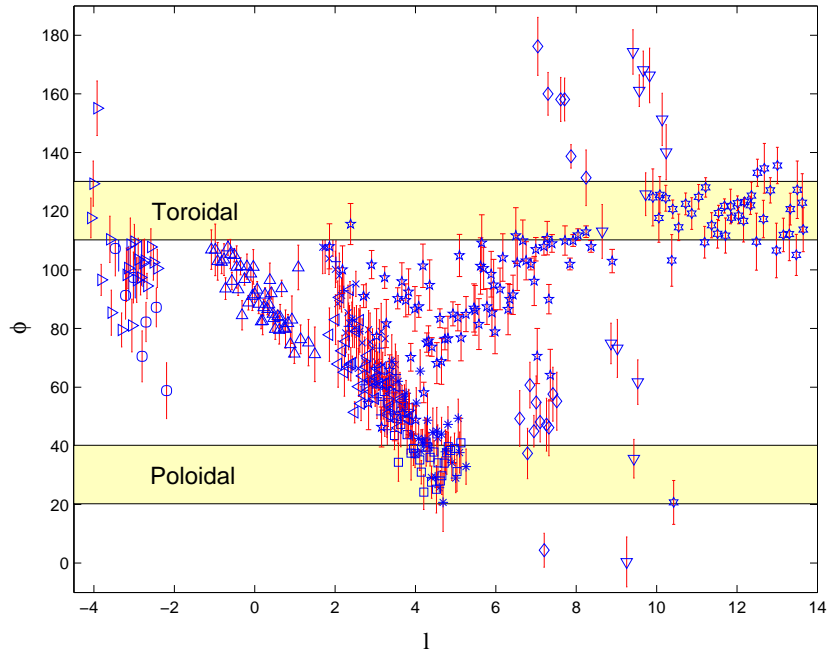


Figure 8.12. The polarization angle is plotted against Galactic longitude. The yellow bands represent angles which correspond to poloidal and toroidal magnetic fields. They are 20° thick to represent the error on a 3σ ($S/N=3$) detection. The different symbols correspond to the different Hertz pointings.

not the first indication that there is something special about this region. It has been speculated that the Radio Arc (Yusef-Zadeh, Morris and Chance 1984) is evidence of an enhancement of the Galactic magnetic field in this region. Other NTFs such as the Northern (G0.08+0.15) and Southern (G359.96+0.09) Threads also permeate this region (Lang, Morris and Echevarria 1999).

8.5.2. Strength of the Magnetic Field

Historically, unknowns such as degree of grain alignment have limited the ability of far-infrared and submillimeter polarimetry to probe field strength. However, the following method presents a possibility for determining a characteristic strength for the field that permeates the central 30 pc of our Galaxy.

Figure 8.13 illustrates the dependence of the polarization angle on the flux measured by SHARC. In this figure, we plot the absolute deviation from a poloidal field ($|\phi - \phi_{\text{poloidal}}|$) versus $350 \mu\text{m}$ flux. This relationship shows that for regions having higher flux (and thus higher column densities), the field is toroidal and hence gravity-dominated. For lower intensities, the trend is that the field becomes poloidal and thus magnetic field dominated. Somewhere between these two extremes is a flux for which the energy density of the poloidal field equals that of the gravitational energy density. In order to proceed with the estimate, we will assume that this density corresponds to a measured angle $|\phi - \phi_{\text{poloidal}}| = 45^\circ$. This choice is somewhat arbitrary. In order to find the flux corresponding to this angle, we perform various binnings as shown in figure 8.14. Linear fits to each of these four plots give a flux of 125 Jy beam^{-1} . To a crude approximation, this energy balance condition is represented by

$$(8.2) \quad \frac{1}{2}\rho v^2 = \frac{B^2}{8\pi}.$$

Here, the kinetic energy density of material orbiting in the gravitational potential well of the Galaxy is equated to the magnetic energy density.

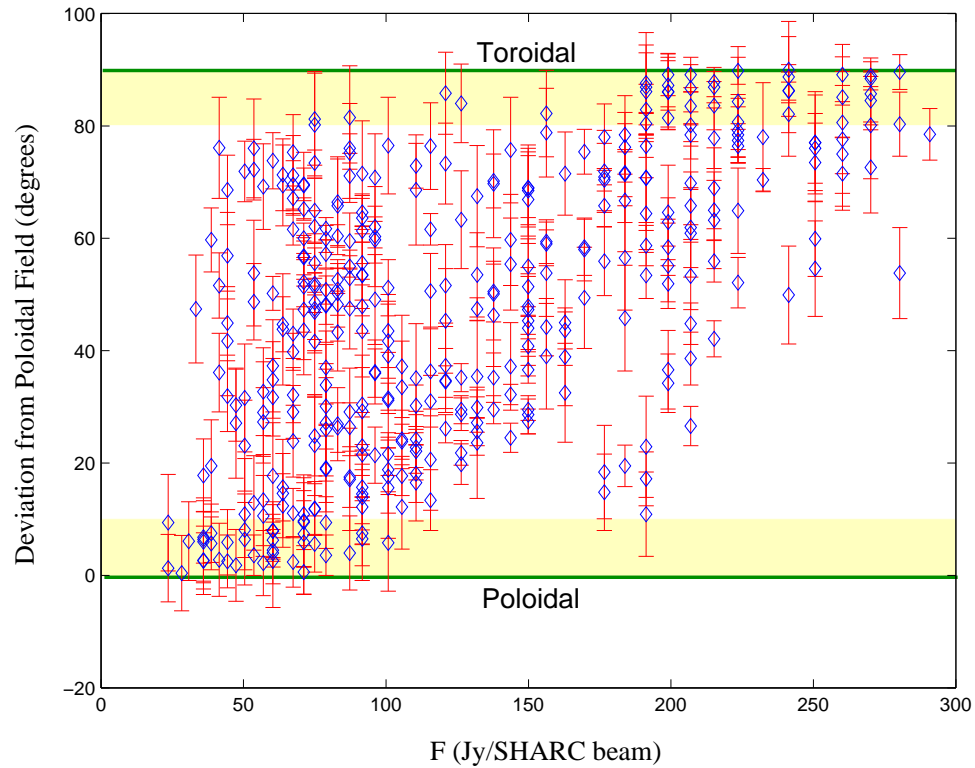


Figure 8.13. The absolute value of the deviation of each measurement from a poloidal field is plotted against $350 \mu\text{m}$ flux in a $15''$ SHARC beam. Here the angles are used from all of the GC polarization measurements. The assumption is that the polarization angle will not change from $60 \mu\text{m}$ to $350 \mu\text{m}$.

The key to this problem now becomes the estimate of ρ and v . v can be estimated from typical cloud velocities (Tsuboi, Handa and Ukita 1999) and is expected to be between $50 - 100 \text{ km s}^{-1}$. The density is a little more difficult.

With the aid of a few assumptions, it is possible to get an estimate for the total dust mass responsible for a submillimeter flux measurement (Hildebrand 1983). To begin with, we assume that the radiation is thermal, and therefore the radiative

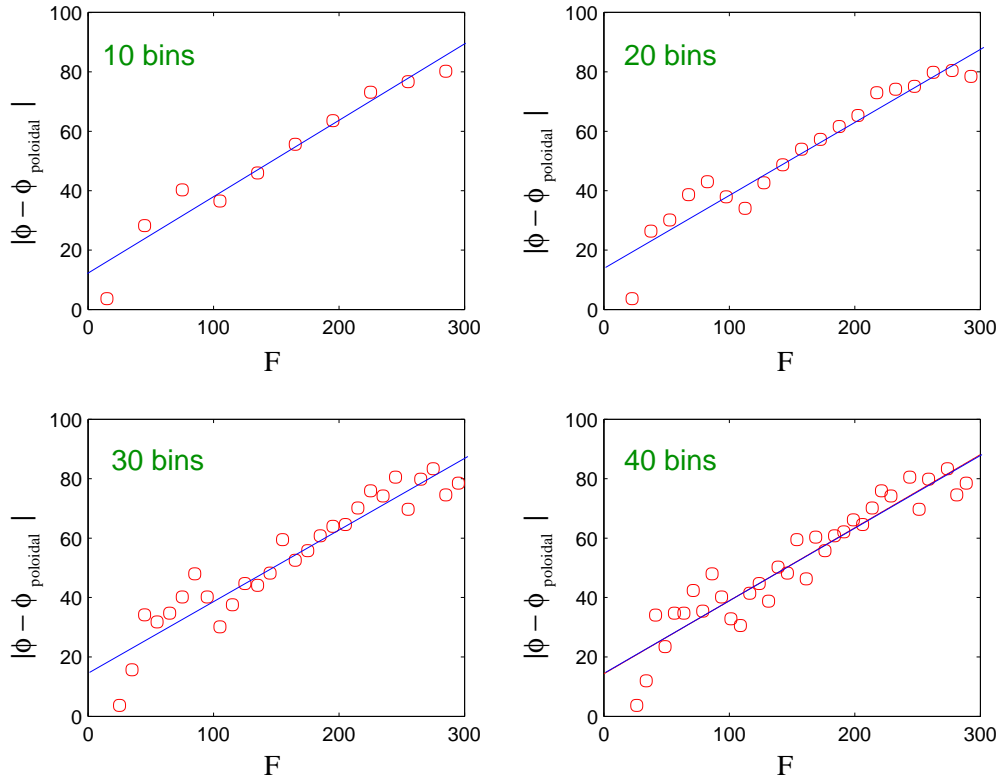


Figure 8.14. The fluxes are grouped into bins. The angles in each bin are averaged to produce the curves above. For each binning, the flux for equality of magnetic and gravitational forces has been calculated by fitting a line and then determining the flux value for a 45° deviation from a poloidal field. By taking the average of the flux values for each of the 4 plots, this flux is 125 Jy beam^{-1} . The error in the choice of bin size is around 1 Jy beam^{-1} .

transfer equation combined with Kirchoff's law yields

$$(8.3) \quad \frac{dI_\nu}{d\tau_\nu} = -I_\nu + B_\nu(T).$$

Here, $B_\nu(T)$ is the Planck function:

$$(8.4) \quad B_\nu(T) = \frac{2h\nu^3/c^2}{e^{h\nu/kT} - 1}.$$

Integrating the radiative transfer equation along the line of sight then gives

$$(8.5) \quad I_\nu = I_\nu(0)e^{-\tau_\nu} + \int_0^{\tau_\nu} e^{-(\tau_\nu - \tau'_\nu)} B_\nu(T) d\tau'_\nu.$$

Since for the molecular material in the Galactic center there is no background source, the first term in this equation vanishes and the second term gives

$$(8.6) \quad I_\nu = B_\nu(T)(1 - e^{-\tau_\nu}).$$

In the case of 350 μm observations, the optical depth is generally small. If $\tau_\nu \ll 1$,

$$(8.7) \quad I_\nu = \tau_\nu B_\nu(T).$$

SHARC measures $F_\nu = I_\nu \Delta\Omega$, the flux of the incoming radiation where $\Delta\Omega$ is the solid angle subtended by a SHARC array element. From these equations, it is possible to express the optical depth of the dust as a function of temperature and measured flux.

$$(8.8) \quad \tau_\nu = \frac{F_\nu}{B_\nu(T) \Delta\Omega}$$

Alternatively, we can express the optical depth as a function of grain properties along the line of sight. Once again we are working in the limit $\tau_\nu \ll 1$. To begin this derivation, we can imagine a column of dust along the line of sight that extends through the entire depth of the Galactic center. The optical depth is proportional to the number density of dust grains along the line of sight (N_d). It is also proportional to the typical geometrical cross-section of each of the grains (σ_d); however, since the grain sizes are generally much smaller than the wavelength of the radiation, the efficiencies of the grains for emitting, scattering or absorbing light are much lower than this blackbody approximation indicates. Thus we write the optical depth as

$$(8.9) \quad \tau_\nu = N_d Q_e \sigma_d,$$

where Q_e is the emissivity of the dust grains and is generally much less than unity for submillimeter radiation.

Once the N_d is found, the total dust mass observed by a SHARC beam is

$$(8.10) \quad M_d = N_d \rho_d v_d \Delta\Omega D^2.$$

Here, D is the distance to the source and $\Delta\Omega D^2$ is simply the physical size of SHARC's beam at a distance D . ρ_d and $v_d \sim \frac{4}{3}\pi a^3$ are the density and volume of a dust grain, respectively. If we then make the appropriate substitutions and assume a gas-to-dust ratio, $X \gg 1$, we get the following expression for the total

mass.

$$(8.11) \quad M = \frac{4 F_\nu \rho_d a D^2 X}{3 Q_e B_\nu(T)}$$

Putting in the appropriate numbers for 350 μm radiation yields

$$(8.12) \quad \frac{M}{M_\odot} = \left(\frac{F}{\text{Jy}}\right) \left(\frac{\rho_d}{\text{g cm}^{-3}}\right) \left(\frac{a}{\mu\text{m}}\right) \left(\frac{D}{\text{kpc}}\right) \left(\frac{X}{Q_e}\right) 6.89 \times 10^{-7} (e^{41.1/T} - 1).$$

The density can be calculated by assuming a value for the depth of the dust layer (L).

$$(8.13) \quad \rho = \frac{M}{\Delta\Omega^2 D^2 L}$$

We use the following grain properties (Dowell et al. 1999) for our grain model. These are $a = 0.1 \mu\text{m}$, $Q_e = 1.9 \times 10^{-4}$, $X = 100$, and $\rho_d = 3 \text{ g cm}^{-3}$. In addition, Pierce-Price, et al. (2000) have used SCUBA to map the CMZ at 450 and 850 μm . They have found the dust temperature to be relatively uniform over the CMZ and adopt a value of 20 K. With these numbers, one can get an estimate of the magnetic field strength as a function of velocity of the material and the thickness of the dust.

$$(8.14) \quad B = 3.0 \text{ mG} \left(\frac{L}{200 \text{ pc}}\right)^{-\frac{1}{2}} \left(\frac{v}{100 \text{ km s}^{-1}}\right)$$

Based on CS measurements of the CMZ (Tsuboi, Handa and Ukita 1999), most molecular material has $v < 150 \text{ km s}^{-1}$. The CMZ has a projected diameter of 200 pc. Assuming cylindrical symmetry, this is approximately the scale of the material along the line of sight.

CHAPTER 9

Conclusions

9.1. The Galactic Center Magnetosphere

9.1.1. Toroidal and Poloidal Fields

The complementary observations of SPARO and Hertz provide evidence for the application of the model of Uchida et al. (1985) (see chapter 2 and chapter 8) to the Galactic center magnetosphere. At low Galactic latitudes, SPARO finds that the field is toroidal over most of the CMZ. Hertz, with its finer resolution, has probed the central 30 pc and found that the field is toroidal in dense molecular clouds in which the gravitational energy density is great enough to shear an initially poloidal field. In less dense regions, the field is found to maintain its initial poloidal configuration. We interpret this observation to be a result of a clumpy Galactic center matter distribution.

Other scenarios for the explanation of the variety of fields in the central 30 pc cannot yet be ruled out. As suggested in chapter 8, winds produced by large explosions could be responsible for the vertical fields seen in this region. However, there are several reasons to favor the association with the vertical fields to a global poloidal field. First of all, the spatial proximity of the vertical fields to the NTFs lends evidence to this association. Second, the ~ 3 mG field strength we derive

is consistent with lower limits of the field found in NTFs. Third, to date we have not been able to locate any sources of a wind on large enough scales that couple to the magnetic field geometries observed. Finally, we see transitions from vertical to toroidal fields that correspond to dynamics of Galactic center molecular clouds, indicating that these two fields have the same origin and that the initial configuration was poloidal.

9.1.2. Generation of Non-Thermal Filaments

It has been discovered that many of the NTFs in the Galactic center are associated with molecular clouds (Serabyn and Güsten 1991; Staguhn et al. 1998). This has led to the suggestion that the source of the relativistic electrons in the NTFs is due to magnetic reconnection (Davidson 1996). The magnetic reconnection is believed to be precipitated by the collision of the cloud with a magnetic flux tube either by distorting the fields in the flux tube or by forcing these fields into contact with those in the cloud.

The notion that the poloidal and toroidal fields have the same origin suggests a third option for the magnetic reconnection scenario. Figure 9.1 illustrates this idea.

In the Galactic center, relative diffuse molecular gas is supported by magnetic pressure (fig. 9.1A); however, this material is free to collapse along the field lines. As the gas collapses, gravitational energy becomes increasingly important. If the material has a velocity with respect to the poloidal field, it can then begin to shear the magnetic field (fig. 9.1B) via the differential motion between the material in

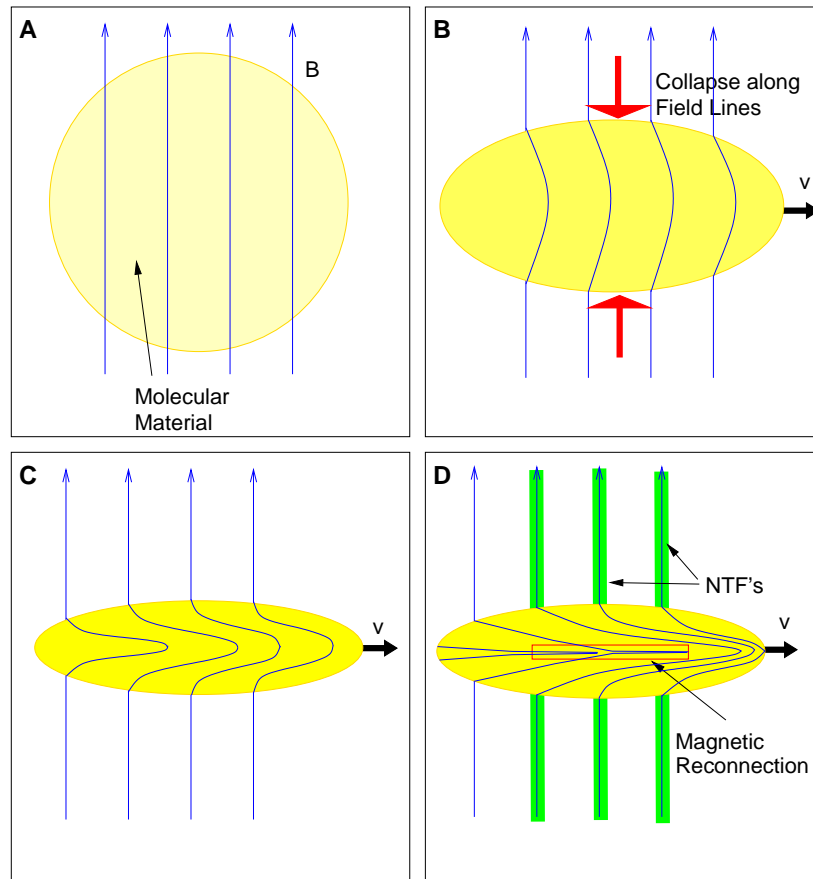


Figure 9.1. Molecular clouds can produce relativistic electrons necessary for the illumination of NTFs by the following process. In regions of low density, the molecular material is dominated by the magnetic field, and we observe a poloidal field (A). MHD allows for movement of material along the lines of flux. In this way, the material can form clouds and gravity can begin to compete with the magnetic field energy density (B). At this stage, velocities of the molecular material with respect to the poloidal field can distort the field. This process continues (C) as the poloidal fields become sheared into toroidal ones in the vicinity of the cloud. Finally, oppositely-oriented magnetic fields near the cloud centers will be forced into contact by gravity and will reconnect, thereby releasing energy that energizes relativistic electrons. These electrons spiral along the external field and produce synchrotron radiation that we observe as an NTF.

the cloud and that in the ambient medium. This shear continues until the field is more parallel than vertical (fig. 9.1C). Note that the field external to the clouds is still quite poloidal because magnetic energy dominates the dynamics of this region, and flux-freezing prevents the matter here from following the cloud. Finally, if the gravitational energy is large enough, and the system is given the time to evolve, the oppositely-oriented fields in the center of the cloud may be squeezed together to enable reconnection. This process releases energy that can produce the relativistic electrons required to “light up” the filaments.

When viewed from this perspective, the submillimeter and far-infrared polarimetry in concert with radio and submillimeter photometric observations present a picture of molecular material of various sizes at various evolutionary stages according to the model in figure 9.1. From the polarimetry data in figure 8.3, we can see examples of each of the four panels in figure 9.1. The area to the north and east of M-0.02-0.07 is an example of the situation depicted in figure 9.1A. Here, the molecular material is not very dense and the magnetic field is perpendicular to the Galactic plane. An example of figure 9.1B is the molecular cloud complex containing M0.07-0.08 and M0.11-0.08. Here the field is seen to be shearing around the front edge of M0.07-0.08, making a transition from poloidal to toroidal at the southern edge of the cloud. The 20 km s^{-1} cloud (M-0.13-0.08) is thought to be shearing out its magnetic field as it falls toward Sgr A* (Novak et al. 2000). The flare seen at the southern end indicates that it has not yet reached the point where magnetic reconnection is occurring and hence best matches figure 9.1C.

The interaction of the Sickle with the GCRA gives the best example of figure 9.1D. Here, the magnetic field in the molecular cloud is observed to be nearly perfectly aligned with the direction of both the cloud and the Galactic plane. Filaments, namely those of the GCRA, are observed, but appear to diffuse into G0.18-0.04, the H II region associated with this interaction. The clumpiness of the H II region and the structure of the filaments themselves may stem from the irregularities of the interior of the cloud where reconnection takes place. This model for NTF production is contrasted to that of Serabyn & Güsten (1991) in figure 9.2.

It is possible that there are similar occurrences in places such as the arched filaments where there is also an observed transition from toroidal to poloidal fields adjacent to an NTF (in this case, the Northern Thread). In order to verify this model with respect to other filaments and clouds in the Galactic center, more data are required.

9.1.3. Strength of the Magnetic Field

Perhaps the most interesting result of this work is the ability to estimate a magnetic field strength via submillimeter and far-infrared polarimetry. This result is dependent upon the model of Uchida et al. (1985). If some other process were responsible for the variety of field geometry (e.g. winds), our estimate for the strength of the field would not be valid because of its reliance on magnetic field dominance in regions of vertical fields. However, the fact that our measurement for typical field strengths within the molecular material agrees with the lower limits measured in regions containing NTFs gives us confidence in this measurements in

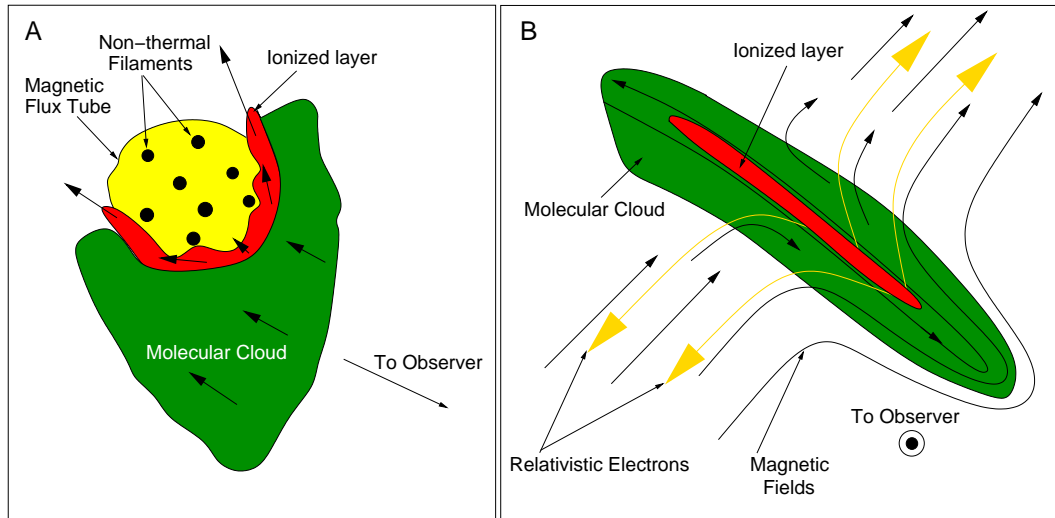


Figure 9.2. The model of Serabyn & Güsten (1991) for the interaction of the molecular cloud associated with the Sickle and the Radio Arc is shown (A). Here, the molecular cloud impacts magnetic flux tube. At the interface, an H II region (ionized layer) is formed. Magnetic reconnection is believed to occur in this region. This happens by either the production of localized distortions in the flux tube produced by the momentum of the collision, or between fields in the flux tube and those in the molecular cloud (Davidson 1996). This magnetic reconnection is believed to be responsible for the production of relativistic electrons required to light up the filaments. Alternatively, B depicts a scenario in which an ambient poloidal field is sheared into toroidal one. In doing so, oppositely-oriented fields near the center of the cloud will be forced into contact leading to magnetic reconnection and the generation of relativistic electrons.

addition to supporting the notion that the fields traced by the NTFs and those traced by far-infrared and submillimeter polarimetry are related. This raises some interesting questions and provides insight into the general nature of the Galactic center magnetosphere. In particular, the question of whether these NTFs are

isolated magnetic enhancements of a globally weaker poloidal field or tracers of a more ubiquitous mG field is not resolved.

The method employed to find the characteristic strength of the magnetic field in the central 30 pc may be extended to larger regions in the following way. If future SPARO observations at higher Galactic latitudes see the transition between a toroidal and a poloidal field that the model predicts, this method may be used to find the characteristic field strength of the entire CMZ.

9.2. Future Work

Future improvements in both detectors and observing techniques will allow for a more thorough investigation of the magnetosphere of the central 30 pc. Better detector efficiencies will lead to more efficient coverage of this region, thereby revealing the complete projected structure of the magnetic field. Improved resolution will provide the opportunity to explore field structure in the cores of the molecular clouds and may provide insight into depolarization. Scan-mapping methods are currently under development. These sophisticated observing procedures, similar to those employed in ground-based submillimeter photometry, have the potential for elimination of reference beam contamination. Continued SPARO observations of fainter regions at higher Galactic latitudes can test the model of Uchida et al. (1985) by determining the field structure in less dense regions where an initially poloidal field is expected to maintain its integrity. Finally, proposed far-infrared polarimetric capability for NASA's new airborne observatory, SOFIA, will provide

magnetic field maps of $\sim 5''$ resolution, a significant improvement over the $20''$ resolution currently achieved for these kinds of observations, as well as permitting us to distinguish between warm and cool regions along the line of sight.

References

- Baganoff, F. K., M. W. Bautz, W. N. Brandt, G. Chartas, E. D. Feigelson, G. P. Garmire, Y. Maeda, M. Morris, G. R. Ricker, L. K. Townsley, and F. Walter. 2001. Rapid X-ray flaring from the direction of the supermassive black hole at the Galactic centre. *Nature* 413:45–48.
- Bania, T. M. 1977. Carbon monoxide in the inner Galaxy. *The Astrophysical Journal* 216:381–403.
- Barvainis, R., D. P. Clemens, and R. Leach. 1988. Polarimetry at 1.3 mm using MILLIPOL - methods and preliminary results for Orion. *The Astronomical Journal* 95:510–515.
- Binney, J., O. E. Gerhard, A. A. Stark, J. Bally, and K. I. Uchida. 1991. Understanding the kinematics of Galactic centre gas. *Monthly Notices of the Royal Astronomical Society* 252:210–218.
- Davidson, J. A. 1996. The magnetic field structure in the Galactic center. In *Polarimetry of the Interstellar Medium held in Troy, New York*, edited by W. G. Roberge and D. C. B. Whittet, Volume 97 of *ASP Conference Series*, 504–521. San Francisco.
- Davis, L., and J. L. Greenstein. 1951. The polarization of starlight by aligned dust grains. *The Astrophysical Journal* 114:206–240.
- Delong, L. E., O. G. Symko, and J. C. Wheatley. 1971. Continuously operating ^4He evaporation refrigerator. *Review of Scientific Instrumentation* 42:147–149.

- Dotson, J. D., J. Davidson, C. D. Dowell, D. A. Schleuning, and R. H. Hildebrand. 2000. Far-infrared polarimetry of Galactic clouds from the Kuiper Airborne Observatory. *The Astrophysical Journal Supplement Series* 128:335–370.
- Dotson, J. L., G. Novak, T. Renbarger, D. Pernic, and J. L. Sundwall. 1998. SPARO: the submillimeter polarimeter for Antarctic remote observing. *Proc. SPIE* 3357:543–547.
- Dowell, C. D., R. H. Hildebrand, D. A. Schleuning, J. E. Vaillancourt, J. L. Dotson, G. Novak, T. Renbarger, and M. Houde. 1998. Submillimeter array polarimetry with Hertz. *The Astrophysical Journal* 504:588–598.
- Dowell, C. D., D. C. Lis, E. Serabyn, M. Gardner, A. Kovacs, and S. Yamashita. 1999. Sharc 350 μm mapping of the galactic center from the caltech submillimeter observatory. In *ASP Conference Series 186: The Central Parsecs of the Galaxy held in Tucson, Arizona, June, 1999*, edited by H. Falcke, A. Cotera, W. Duschl, F. Melia, and M. Rieke, 453–465.
- Ghez, A. M., B. L. Klein, M. Morris, and E. E. Becklin. 1998. High proper-motion stars in the vicinity of Sagittarius A*: Evidence for a supermassive black hole at the center of our Galaxy. *The Astrophysical Journal* 509:678–686.
- Goldsmith, P. F., D. C. Lis, D. F. Lester, and P. M. Harvey. 1992. High angular resolution far-infrared observations of Sagittarius B2. *The Astrophysical Journal* 389:338–346.
- Harwit, M. 1998. *Astrophysical Concepts* (3rd ed.). New York: Springer.
- Hildebrand, R. H. 1983. The determination of cloud masses and dust characteristics from submillimetre thermal emission. *Quarterly Journal of the Royal Astronomical Society* 24:267–282.
- Hildebrand, R. H., J. A. Davidson, J. L. Dotson, C. D. Dowell, G. Novak, and J. E. Vaillancourt. 2000. A primer on far-infrared polarimetry. *Publications of the Astronomical Society of the Pacific* 112:1215–1235.

- Ho, P. T. P., L. C. Ho, J. C. Szczepanski, J. M. Jackson, and J. T. Armstrong. 1991. A molecular gas streamer feeding the Galactic Centre. *Nature* 350(March):309–312.
- Jackson, J. D. 1975. *Classical Electrodynamics* (2nd ed.). New York: John Wiley & Sons, Inc.
- Lang, C., M. Morris, and L. Echevarria. 1999. A radio polarimetric study of the Galactic center threads. *The Astrophysical Journal* 526:727–743.
- LaRosa, T. N., N. E. Kassim, T. J. W. Lazio, and S. D. Hyman. 2000. A wide-field 90 centimeter VLA image of the Galactic center region. *The Astrophysical Journal* 119:207–240.
- Lazarian, A. 2000. Physics of grain alignment. In *Cosmic Evolution and Galaxy Formation: Structure, Interactions, and Feedback held in San Francisco, May, 2000*, by ASP, 215, 69–78.
- Lis, D. C., and J. C. Carlstrom. 1994. Submillimeter continuum survey of the galactic center. *The Astrophysical Journal* 424:189–199.
- Mather, J. C. 1982. Bolometer noise: Nonequilibrium theory. *Applied Optics* 21:1125–1129.
- Matthews, B. C., J. D. Fiege, and G. Moriarty-Schieven. 2002. Magnetic fields in star-forming molecular clouds. III. the submillimeter polarimetry of intermediate-mass cores and filaments in Orion B. *The Astrophysical Journal* 569:304–321.
- Matthews, B. C., C. D. Wilson, and J. D. Fiege. 2001. Magnetic fields in star-forming molecular clouds. II. the depolarization effect in the OMC-3 filament of Orion A. *The Astrophysical Journal* 562:400–423.
- Mezger, P. G., W. J. Duschl, and R. Zylka. 1996. The Galactic center: A laboratory for AGN? *Annual Review of Astronomy and Astrophysics* 7:289–388.
- Morris, M., and E. Serabyn. 1996. The Galactic center environment. *Annual Review of Astronomy and Astrophysics* 34:645–701.

- Novak, G., D. Chuss, T. Renbarger, G. S. Griffin, M. G. Newcomb, J. B. Peterson, R. F. Loewenstein, D. Pernic, and J. L. Dotson. 2002. First results from SPARO: Evidence for large-scale toroidal magnetic fields in the Galactic center. Submitted to the *Astrophysical Journal*.
- Novak, G., J. L. Dotson, C. D. Dowell, P. F. Goldsmith, R. H. Hildebrand, S. R. Platt, and D. A. Schleuning. 1997. Polarized far-infrared emission from the core and envelope of the Sagittarius B2 molecular cloud. *The Astrophysical Journal* 487:320–327.
- Novak, G., J. L. Dotson, C. D. Dowell, R. H. Hildebrand, T. Renbarger, and D. A. Schleuning. 2000. Submillimeter polarimetric observations of the Galactic center. *The Astrophysical Journal* 529:241–250.
- Novak, G., D. P. Gonatas, R. H. Hildebrand, and S. R. Platt. 1989. A 100- μm polarimeter for the Kuiper Airborne Observatory. *Publications of the Astronomical Society of the Pacific* 101:215–224.
- Okumura, S. K., M. Ishiguro, T. Kasuga, K. Morita, R. Kawabe, E. B. Fomalont, T. Hasegawa, and H. Kobayashi. 1991. A finger-like extension of the 20 kilometer per second cloud toward the Galactic center. *The Astrophysical Journal* 378(September):127–130.
- Pierce-Price, D., J. S. Richer, J. S. Greaves, W. S. Holland, T. Jenness, A. N. Lasenby, G. J. White, H. E. Matthews, D. Ward-Thompson, W. R. F. Dent, R. Zykla, P. Mezger, T. Hasegawa, T. Oka, A. Omont, and G. Gilmore. 2000. A deep submillimeter survey of the Galactic center. *The Astrophysical Journal* 545:L121–L125.
- Platt, S. R., R. H. Hildebrand, R. J. Pernic, J. A. Davidson, and G. Novak. 1991. 100- μm array polarimetry from the Kuiper Airborne Observatory: Instrumentation, techniques, and first results. *Publications of the Astronomical Society of the Pacific* 103:1193–1210.
- Press, W. H., S. A. Teukolsky, W. T. Vetterling, and B. P. Flannery. 1992. *Numerical recipes in C*. New York: Cambridge University Press.

- Price, S. D., M. P. Egan, S. J. Carey, D. R. Mizuno, and T. A. Kuchar. 2001. *Midcourse Space Experiment* survey of the galactic plane. *The Astrophysical Journal* 121:2819–2842.
- Purcell, E. M. 1979. Suprathermal rotation of interstellar grains. *The Astrophysical Journal* 231:404–416.
- Renbarger, T. 2002. *SPARO instrument characterization and first results*. Ph. D. thesis, Northwestern University.
- Schleuning, D. A., C. D. Dowell, R. H. Hildebrand, and S. R. Platt. 1997. Hertz, a submillimeter polarimeter. *Publications of the Astronomical Society of the Pacific* 109:307–318.
- Serabyn, E., and R. Güsten. 1991. The H II region G0.18-0.04: Ionization of a molecular cloud by impact with a strong magnetic field. *Astronomy and Astrophysics* 242:376–387.
- Serkowski, K. 1974. Polarization techniques. In N. Carleton (Ed.), *Methods of Experimental Physics Volume 12 - Part A: Astrophysics - Optical and Infrared*, 361–416. New York: Academic Press.
- Simpson, J. P., F. C. Witteborn, M. Cohen, and S. D. Price. 1999. The mid-infrared spectrum of the Galactic center- a starburst nucleus. In *ASP Conference Series 186: The Central Parsecs of the Galaxy held in Tucson, Arizona, June, 1999*, edited by H. Falcke, A. Cotera, W. Duschl, F. Melia, and M. Rieke, 527–535.
- Spitzer, L. 1998. *Physical processes in the interstellar medium*. New York: John Wiley & Sons, Inc.
- Staguhn, J., J. Stutski, K. I. Uchida, and F. Yusef-Zadeh. 1998. The interaction of the Galactic center filament system G359.54+0.18 with its ambient medium. *The Astrophysical Journal* 336:290–300.

- Tsuboi, M., T. Handa, H. Tabara, T. Kato, Y. Sofue, and N. Kaifu. 1986. Prominent polarized plumes in the Galactic center region and their magnetic field. *The Astronomical Journal* 92:818–824.
- Tsuboi, M., T. Handa, and N. Ukita. 1999. Dense molecular clouds in the Galactic center region I: Observations and data. *The Astrophysical Journal* 120:1–39.
- Tsuboi, M., N. Ukita, and T. Handa. 1997. An expanding shell-like molecular cloud near the Galactic Center Arc. *The Astrophysical Journal* 481:263–266.
- Uchida, Y., K. Shibata, and Y. Sofue. 1985. Origin of the Galactic Center Lobes. *Nature* 317:699–701.
- Wang, Q. D., E. V. Gotthelf, and C. C. Lang. 2001. UMass/Columbia Galactic Center Chandra Survey: The nature of the X-ray emission from the Galactic central region. *American Astronomical Society Meeting* 199(December):1474.
- Yusef-Zadeh, F., M. Morris, and D. Chance. 1984. Large, highly organized radio structures near the Galactic center. *Nature* 310:557–561.
- Zylka, R., P. G. Mezger, and J. E. Wink. 1990. Anatomy of the Sagittarius A complex. I - geometry, morphology and dynamics of the central 50 to 100 parsecs. *Astronomy and Astrophysics* 234(August):133–146.